The Production of Zero Hypercharge Baryons in 6 Gev./c K^-p Interactions.

by Kenneth Paler.

A Thesis presented for the degree of
Doctor of Philosophy of the
University of London.

Department of Physics,
Imperial College,
London S.W.7.

March 1967.

ABSTRACT

This thesis contains a complete analysis of the interactions $K^-p \rightarrow \Lambda^\circ\pi^+\pi^-$ and $K^-p \rightarrow \Lambda^\circ\pi^+\pi^-\pi^\circ$. The emphasis is placed on determining the production mechanism of the two, three and four-body channels. The results of this analysis are that there is a dominance of a vector meson exchange mechanism for the two-body channels and a double peripheral mechanism for the three-body channels. The mechanism for the four-body channel is less clear and no firm conclusions can be reached. A comparison with other experiments is also made.

TABLE OF CONTENTS

		Page
Title.		1
Abstract.		2
Table of Contents.		3
Preface.		5
Introduction		6
Chapter 1	Instrumentation.	
1.1	The Beam.	9
1.2	The Bubble Chamber.	13
1.3	The Scanning and Measuring Machines.	18
Chapter 2	Data Processing.	
2.1	Scanning and Measuring.	22
2.2	Computing.	27
Chapter 3	Biases, Errors and Cross Sections.	
3.1	Biases due to the Apparatus.	40
3.2	Biases due to Data Processing.	45
3.3	Contamination.	50
3.4	Cross Sections.	54
3.5	Resolution.	56
Chapter 4	General Definitions and the $\Lambda^0\pi^+\pi^-$ Final State.	
4.1	Kinematic Definitions.	59
4.2	Definitions of Angles.	61
4.3	$K^-p \rightarrow \Lambda^0\pi^+\pi^-$ General Features.	64

4.4	The Two-Body Channels.	71
4.5	The Three-Body Channel.	75
Chapter 5	The $\Lambda^\circ\pi^+\pi^-\pi^\circ$ final state.	
5.1	General Features.	79
5.2	The Two-Body Channels.	88
5.3	The Three-Body Channels.	99
5.4	The Four-Body Channel.	113
Chapter 6	Comparisons with Theory and other Experiments.	
6.1	The Two-Body Channels.	123
6.2	The Three-Body Channels.	132
6.3	The Four-Body Channel.	138
Conclusion.		141
References.		144
Aknowledgements.		147

PREFACE.

The author joined the High Energy Nuclear Physics Group of Imperial College in October 1963 and after satisfactorily completing the Postgraduate Lecture Course began working on the 3.5 Gev./c K^-p experiment. In the summer of 1964 the film of 6 Gev./c K^-p interactions in the 1.5 m. chamber was taken and the author has worked on this experiment from then onwards. The author was responsible for the initial data processing program which put the measurements of the events into a format suitable for the Rutherford Laboratory geometry program and was solely responsible for the analysis and presentation of the $\Lambda^\circ\pi^+\pi^-$ and $\Lambda^\circ\pi^+\pi^-\pi^\circ$ data.

INTRODUCTION

This experiment was begun at C.E.R.N. in the summer of 1964 and was a collaboration between the Universities of Birmingham, Glasgow, and Oxford, Imperial College, The Rutherford High Energy Laboratory (R.H.E.L.) and The Max Planck Institute Munich. At that time it used the highest momentum negative kaon beam (6 Gev./c) in existence and was the first experiment to use the 1.5 metre British National Hydrogen Bubble Chamber (B.N.H.B.C.). The main aim of the experiment was to search for evidence of the existence of the Ω^- particle which was predicted by the SU_3 classification scheme for elementary particles.[0.1,0.2,0.3] Details of this search are given elsewhere.[0.4]

This thesis is an investigation of the processes which produce a zero hypercharged baryon and result in the final states $\Lambda^o\pi^+\pi^-$ and $\Lambda^o\pi^-\pi^+\pi^o$. The theme of the thesis is to perform a complete analysis of the processes $K^-p \rightarrow \Lambda^o\pi^+\pi^-$ and $K^-p \rightarrow \Lambda^o\pi^+\pi^-\pi^o$ with an emphasis upon the production mechanism of each channel. The method used was to isolate each channel with as small a background as possible and investigate the decay angular distributions of any resonance produced in a particular channel and also the correlations between the momenta, scattering angles and production angles of the particles in the channel. The decay angular distributions give information about the quantum numbers of the exchanged system in the case of a peripheral production mechanism. The interpretation

of these distributions is less precise on the basis of the Absorption and Regge Models than on a simple Peripheral Model. The various correlations provide information on the kinematic configuration of a particular channel. This has principally been used for the study of the three and four body final states.

These channels were difficult to analyse because their cross sections were small relative to the channels $K^{*-}p$, $K^{*-}\pi^{+}n$ and $K^{*-}\pi^{\circ}p$ for example and the statistics were in general small. This was so because most of the events at this energy are produced by peripheral collisions and on the basis of a simple exchange mechanism the channels considered in this thesis must be produced by hypercharge or baryon exchange. Both these mechanisms have a much lower probability of occurring than the vacuum or zero hypercharge meson exchange mechanisms which produce the channels given above. A further difficulty was that there were many resonance channels produced in the $\Lambda^{\circ}\pi^{+}\pi^{-}$ and $\Lambda^{\circ}\pi^{+}\pi^{-}\pi^{\circ}$ final states, and each resonance had a small signal to noise ratio which made it difficult to separate from background.

The zero hypercharge baryons are defined by the relation

$$Q = I_3$$

where Q = electric charge

and I_3 = the third component of the isotopic spin.

This is derived from the empirical Gell-Mann and Nishijima relation;

$$Q = I_3 + \frac{B+S}{2} = I_3 + Y/2$$

where B = baryon number

S = strangeness

and Y = hypercharge.

The zero hypercharge baryons considered in this thesis are the Λ° and $Y_1^{*+}(1385)$. The Λ° belongs to the SU_3 octet of $(1/2)^+$ baryons and the $Y_1^{*+}(1385)$ to the SU_3 decuplet of $(3/2)^+$ baryons. The quantity in the parentheses is the spin and the superscript denotes the parity.

The system of units used throughout this thesis will be that in which the velocity of light is unity. Thus both momentum and energy will be expressed in terms of Gev.

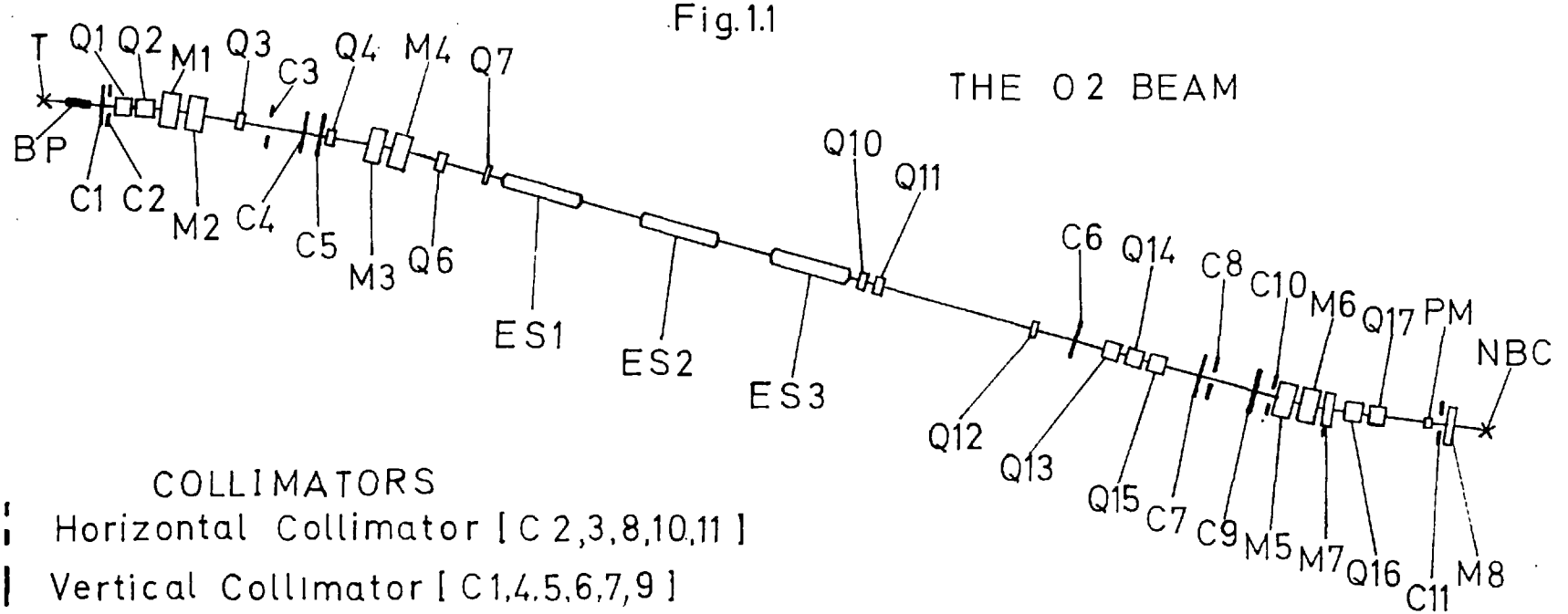
CHAPTER 1

1.1 The Beam.

The beam[1.1,1.2] for this experiment (called 02) was built in the East Experimental area of the C.E.R.N. Proton Synchrotron. It was designed as an all purpose beam producing kaons, pions, protons and antiprotons up to a momentum of 15 Gev. To achieve this the beam could be run in two modes of mass separation. One mode was electrostatic for momenta up to 8 Gev. and the other was radiofrequency, for momenta up to 15 Gev. For this experiment the beam was used in the electrostatic mode to produce negative kaons of 6 Gev. momentum. This form of the beam will be described briefly.

The layout of the beam is shown in Fig.1.1. The length of the beam line was 180 metres and incorporated many new features. The first of these was that the target was placed in the curved magnet section 60 of the Proton Synchrotron. This enabled an essentially zero angle secondary beam to be extracted with an intensity higher than would otherwise have been obtained. This beam was shielded from the magnetic fringing field of the next magnet section by a soft iron tube. The remaining part of the beam contained 14 standard

Fig. 1.1



COLLIMATORS

Horizontal Collimator [C 2,3,8,10,11]

Vertical Collimator [C 1,4,5,6,7,9]

MAGNETS

2m. Quadrupole [Q 1,2,13,14,15,16,17]

1m. Quadrupole [Q 3,4,6,10,11]

0.5m. Quadrupole [Q 7]

2 m. Horizontal Bending Magnet [M 1,2,3,4,5,6]

1m. Vertical Bending Magnet [M 7,8]

1m. Pulsed Bending Magnet (Vertical) [PM]

T Target

NBC Bubble Chamber

Electrostatic Separator [E S 1,2,3]

C.E.R.N. quadrupole magnets, 8 bending magnets, 11 collimators, and 3 electrostatic separator tanks which gave a total plate length of 27 metres.

The second new feature of the beam was that the collimator jaws were independently adjustable which provided easy and more accurate tuning of the beam. The muon and scattered particle background was reduced [1.3] by separating the horizontal and vertical foci and using independent horizontal and vertical collimators.

The beam could be considered generally as made up of three sections. The first was the beam acceptance section where the phase space acceptance (target area x solid angle acceptance) and momentum bite were defined. The second was the single stage electrostatic mass separation, and the third was the section where the phase space acceptance and momentum bite were redefined. The beam was designed in this way, with single stage mass separation, because with the redefining third section it gave a beam of reasonable purity and, more important, a higher beam flux at this momentum than multi-stage mass separation.

The beam purity will now be discussed. This is a very important beam parameter because large amounts of pion contamination make the analysis of the interactions difficult and the results unreliable. To this end another new feature

was used in the beam. This was the estimation of beam purity by counting kaons and non-kaons and attempting to label the beam tracks as kaons and non-kaons. The counting was arranged so that the number of coincidences between two scintillation counters were recorded. This gave the total number of particles entering the chamber and was defined as the B count. At the same time counts were recorded of the coincidences of the scintillation counters and a čerenkov counter which discriminated against kaons.

This gave the number of background particles and was defined as the A count. The difference (B - A) is the number of kaons. This difference method removed any systematic effects due to spurious coincidences. The track labelling was done using a C.R.T. display which was photographed along with the bubble chamber. The C.R.T. monitored the position of a beam track along the x -axis, and the nature of the particle,as detected by the čerenkov counter, by a y -axis deflection. This system was only partially sucessful due to poor photographic recording and the lack of a clear correlation between the actual positionsof the beam tracks on the film and the positionsof the y -deflections. The contamination of the beam by pions and muons was evaluated[1.4] by studying the absorption of the beam by various thicknesses of lead,the mirror image of the low mass side of the pion

peak,and the ratio of the interactions with one seen neutral decay to all interactions for various B and A values. The average value,given by these methods,of the pion to kaon ratio was ;

a) 15 ± 5% for the first third of the film.

b) 2 ± 2% for the remaining two thirds of the film.

On the basis of these figures and the fact that the interactions considered in this thesis contain only one strange particle the pion contamination was ignored. Table 1.1 shows typical beam parameters.

1.2 The Bubble Chamber. (1.5)

The chamber used in this experiment was the B.N.H.B.C. This was the first large United Kingdom bubble chamber. It was built at the Rutherford High Energy Laboratory (R.H.E.L.), and was a joint project,begun in 1957, by the Universities of Birmingham, Liverpool and Oxford, Imperial College and R.H.E.L. The hydrogen tank was 150 cms. long, 50 cms. high and 47 cms. deep,giving a liquid volume of 300 litres. This volume was enclosed by vertical glass walls (windows) and an aluminium casting to allow good temperature control.

The chamber was run at a temperature of 27° K which was maintained by hydrogen refrigeration loops around the aluminium walls. The chamber windows (1.6)

were made of borosilicate crown glass, chosen with regard to price, transparency to the blue end of the spectrum, homogeneity, freedom from bubbles and chemical stability. The window seals were soft indium gaskets which on one side of the glass were mounted on an inflatable stainless steel tube. The fiducial crosses were ruled on the inner side of the windows to an accuracy of 10 microns. The chamber was surrounded firstly by a hydrogen shield, then a nitrogen shield, both being used to reduce radiation losses, and finally a vacuum tank. Apertures in these shields were kept small for safety and to reduce heat radiation into the chamber. The basic constructional features are shown in Fig. 1.2.

A gas expansion system was used due to its great reliability. It was designed to reduce the uneven expansion and turbulence inherent in such a large chamber. The eveness of expansion was obtained by effectively expanding the complete top surface of the liquid hydrogen. This was done with 48 separate expansion tubes in which the liquid surfaces were equidistant from the expansion valve. This arrangement allowed the pressure to be applied simultaneously over the top surface of the liquid. The stability was increased because there were no large gas liquid interfacial areas and also because a controlled

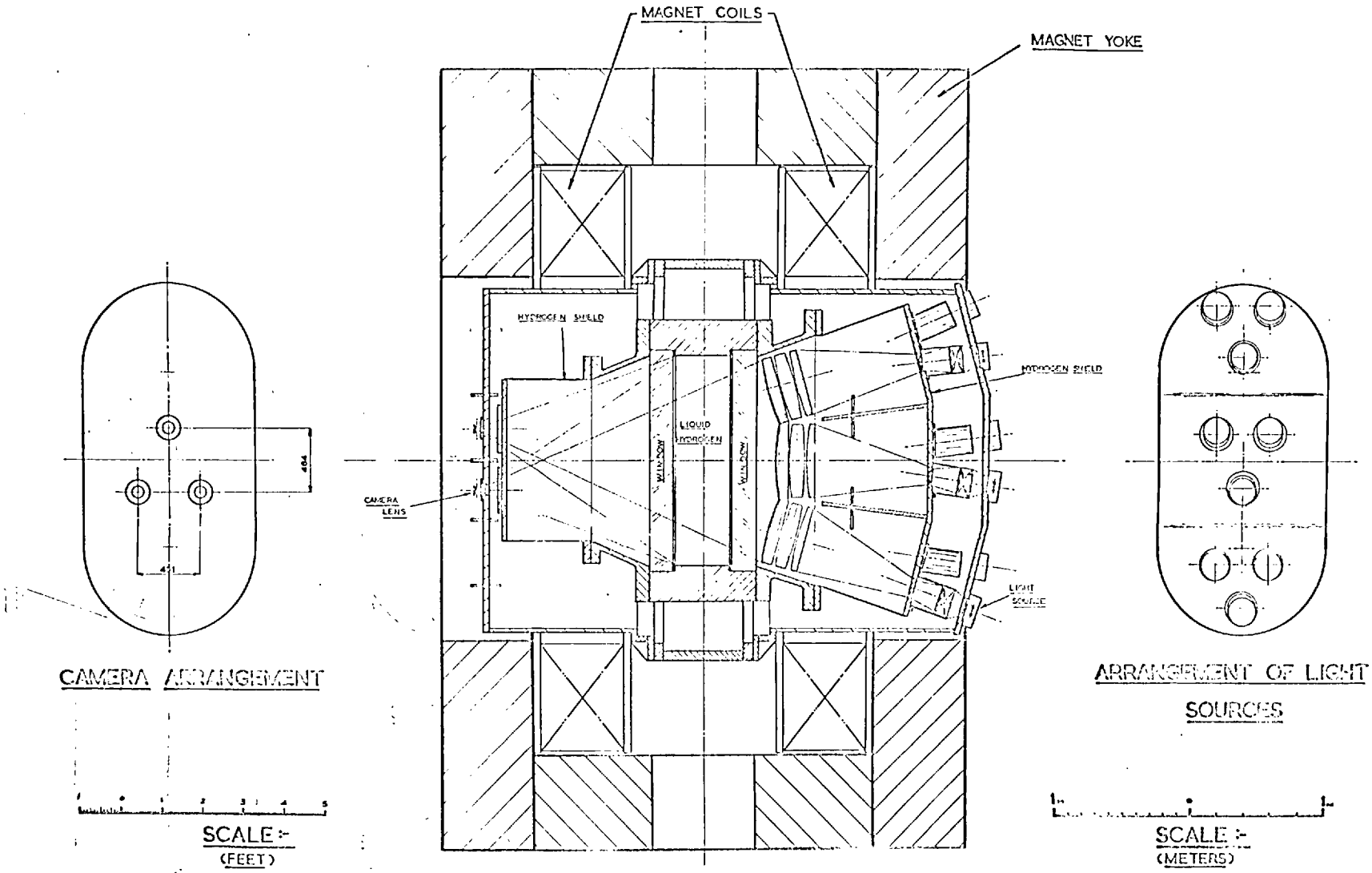

MAGNET COILS
MAGNET YOKE
HYDROGEN SHIELD
HYDROGEN SHIELD
LIQUID HYDROGEN
WINDOW
WINDOW
CAMERA LENS
LIGHT SOURCE
CAMERA ARRANGEMENT
SCALE :-
(FEET)
ARRANGEMENT OF LIGHT SOURCES
SCALE :-
(METERS)

Fig. 1.2

height of liquid was maintained in the expansion tubes. This produced an inertial volume which tended to damp any subsequent oscillations after expansion. The sequence of the bubble chamber cycle was that a signal from the Proton Synchrotron control room initiated the expansion of the chamber so that the beam pulse arrived at the chamber when it was sensitive . About 1.5 ms. after the beam pulse the flash tubes were fired and the photograph taken. The cycling time was about 2 secs.

The magnet of total weight 300 tons. was run at about 4 MW. and 500 volts. giving a field of approximately 12 Kgauss. The magnetic field at the geometrical centre of the magnet was found by proton nuclear magnetic resonance. The mapping of the field[1.7] in the chamber volume was done using a calibrated Hall Plate. The maximum mapping error was 0.25 % and the variation of the magnetic field across the chamber was 3 %.

The illumination system was of the straight through type. This was preferred over the retrodirective system because there was a better possibility of obtaining photographs of high quality and accuracy. This was at the expense of magnetic field strength. The consideration of the following points led to the adoption of a dark field illumination system and essentially three separate identical optical systems, each of

which illuminated one third of the chamber volume.

(a) Contrast of the tracks with background.

(b) The lower limit to the scattering angle.

(c) The observed volume. (This decreases as the scattering angle decreases, especially if each camera has its own light source.)

(d) Uniformity of illumination. (This is particularly important for visual ionization estimates.)

Each optical system had three ring shaped xenon flash tubes of 7 cms. diameter imaged around each camera on a circle of 14 cms. diameter, thus enabling small angle(2°)scattering to be used. The general features of the optical system are shown in Fig.1.2.

Three cameras rigidly mounted in the form of a triangle (see Fig.1.2) were used to photograph the bubble chamber. The film transport was automatic and the 35 mm. unperforated film was held firm by vacuum suck down. The camera lenses were wide angle (field coverage $\pm 30^{\circ}$) Ross Aerial Survey type, with a focal length of 8.2 cms. The residual coma, astigmatism and transverse colour were removed by a 15 mm. plate of borosilicate crown glass placed between film plane and lens. The cameras were focussed in a plane in the middle of the chamber. The depth of focus was 45 cms. and the demagnification was 16 at an aperture of f/25. A bubble had the diameter of the

first dark ring of the Airy Disc (19 microns) by slightly under-exposing. A data panel which contained the date, run, magnetic field value and the A and B counts was also photographed with the chamber. The results from the chamber were very variable. About 15% of the film received by Imperial College was classified as unusable. The film was taken in three runs with parameters;

Run	Amount of film (%)	Beam Momentum (Gev.)	Magnetic Field (Kgauss.)
D	15	6.02 ± 0.06	13.54
E	30	6.04 ± 0.06	12.28
F	55	6.02 ± 0.06	13.54

1.3 Scanning and Measuring Machines(1.8).

The scanning machines used were designed at R.H.E.L. and Imperial College. They satisfied the general requirements of scanning machines. These are;

(a) High reliability.

(b) Reasonable picture size (A magnification of 10 was used).

(c) Good focus and illumination, so that photographs could be made.

(d) Fast efficient film transport. The average time to scan a frame was 2-3 secs.

Later the magnification was increased to 15 for ionization scanning. The general features of the machines were a three channel projection system with two 45° mirrors, which produced an image on a horizontal white table , and an electrically driven film transport system.

Three measuring machines were used at Imperial College. Two were known as the National Measuring Machines and were also designed by R.H.E.L. and Imperial College. The third was a home made machine upon which the author initially worked. A brief descriptionof one of the National machines will now be given. It had a three channel illumination system thus accomadating the three views of the chamber. It had a projection system which produced a complete stationary image of magnification 10. This enabled particular frames and events to be found easily . The main channels were illuminated by a single high pressure mercury lamp. Part of the illumination was used to produce an image, magnified 30 times , of a small part of the view to be measured. This facilitated accurate measurement. Measurements were made by setting a fiducial cross, which moved with the projection lens, upon the point to be measured and recording its position. The complete event was measured on three views by recording the relative perpendicular movements of the lens and film stage from one setting of the fiducial cross to another along the tracks of the event. These movements were

recorded by a moiré fringe system producing voltages which were fed into a two-way octal scalar with a least count of 2 microns. on the film. These numbers were punched out on five hole paper tape in binary coded octal. This machine was later modified to operate in a semi-automatic manner(1.9).

TABLE 1.1

Some properties of the Electrostatic Beam recorded on 29/9/64.

1. Target.

Height	1.0 mm.
Width	1.0 mm.
Length	80 mm.
Material	Aluminium.
Effioiency	10 %

2. Production Angle.

K^-	3°

3. Transmission

Solid Angle x Momentum Bite	1.1×10^{-6}.

4. Separation.

Electric Field	50 kV./cm.
Plate Gap	10 cm.
Plate Length	27 m.
$\pi^- - K^-$ separation	10 mm.
Magnification relative to target	4.8.

5. Ciculating proton beam in P.S.

Intensity	$6 - 8 \times 10^{11}$
Energy	21.54 Gev.

CHAPTER 2

The data processing system.

The setting up of an efficient and fast data processing system is an important part of an experiment analysing many frames of bubble chamber film. The processing system used in this experiment is shown diagrammatically in Fig.2.1. In this system very efficient book-keeping was used to keep the number of lost and unprocessed events to a minimum. This also applied to the computer programs used at the various stages of processing. The processing status of each event was therefore accurately known and the rejection rate due to program failure was small. The system can be more easily described by considering it in two parts;

(1) scanning and measuring,

(2) computing.

2.1 Scanning and measuring.

The film received by Imperial College was approximately 60,000 frames, each having three views. This film was divided into rolls of about 1,300 frames. Each roll was scanned, that is each frame was inspected visually for any interaction between the beam particles and the protons in the hydrogen. Each interaction was called an event if it satisfied certain scanning criteria. The scanning criteria were designed to classify events and to reject spurious events and unmeasurable events. The criteria were defined for view 2 and were concerned mainly with three things;

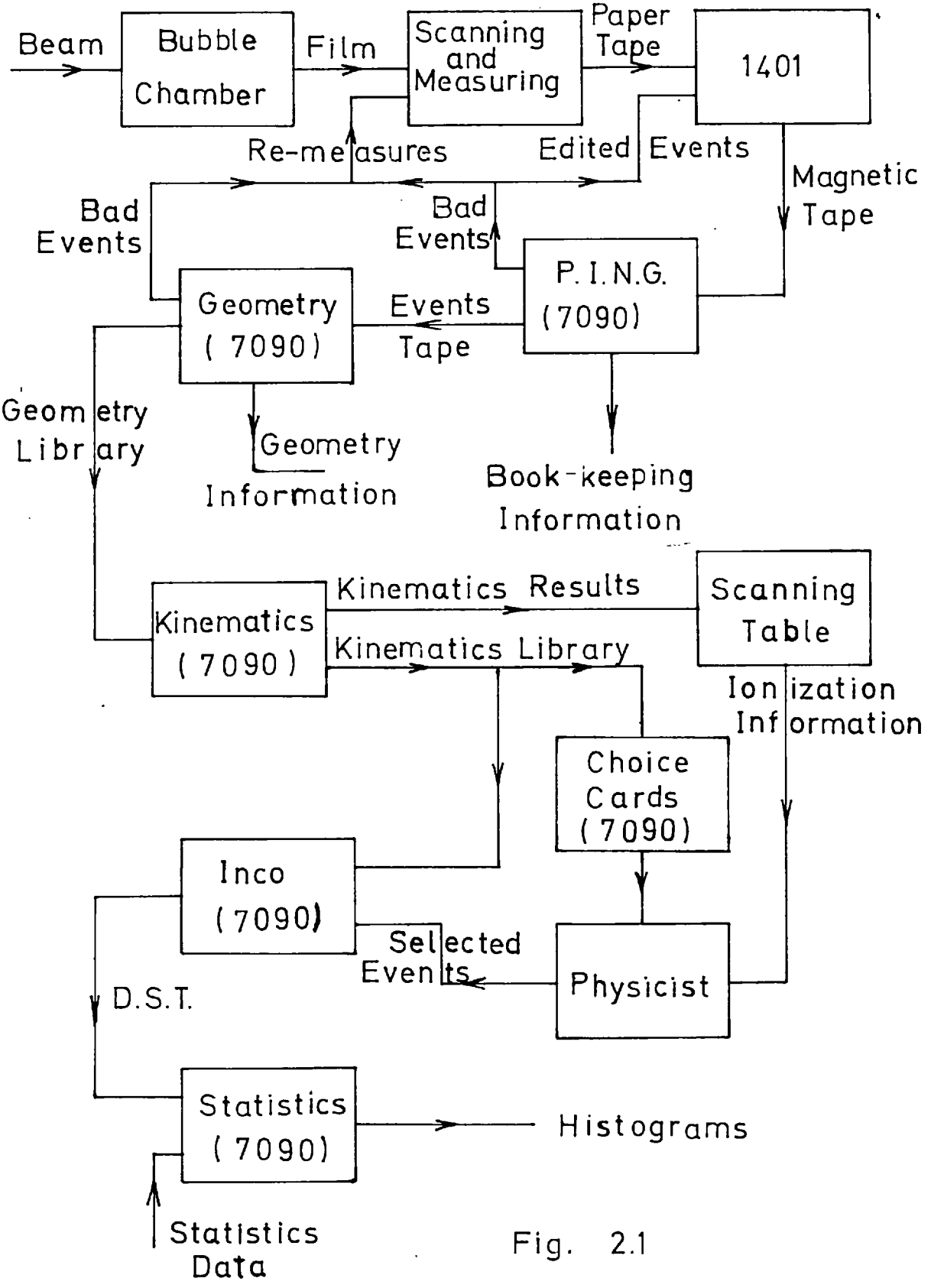

Beam
Bubble Chamber
Film
Scanning and Measuring
Paper Tape
1401
Re-measures
Edited Events
Magnetic Tape
Bad Events
Bad Events
P.I.N.G. (7090)
Geometry (7090)
Events Tape
Geometry Library
Geometry Information
Book-keeping Information
Kinematics Results
Scanning Table
Kinematics (7090)
Kinematics Library
Ionization Information
Choice Cards (7090)
Inco (7090)
Selected Events
Physicist
D.S.T.
Statistics (7090)
Histograms
Statistics Data

Fig. 2.1

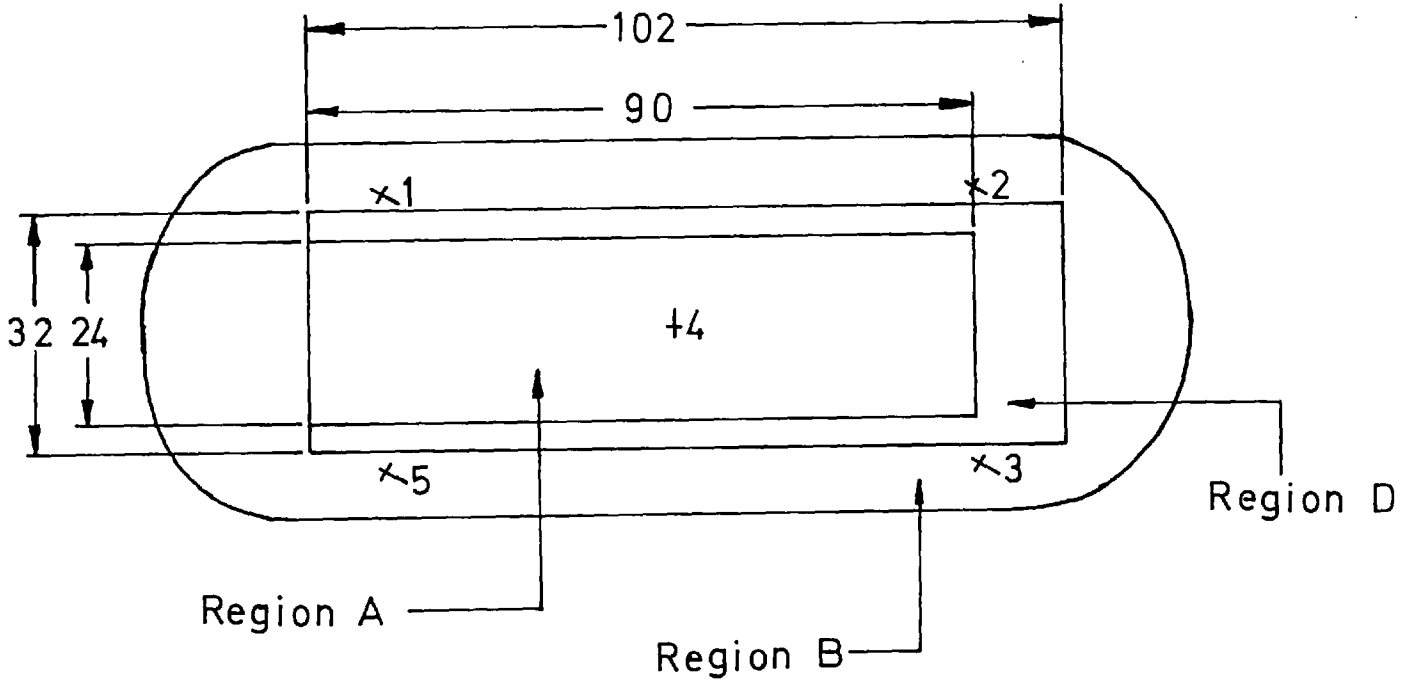
(i) the region in which the event occurred,

(ii) the neutral decay,

(iii) the charged decay.

With regard to (i), the chamber was divided into three regions which are shown in Fig.2.2. These regions were chosen so that sufficient length of track from the production vertex and decay vertex was available to allow a good momentum measurement to be made. These regions were defined on the back glass as seen by camera 2. The events were classified by three numbers which indicated the appearance(topology) of the event on the film. The first was the number of charged tracks associated with the production vertex, the second was the number of charged decays and the third was the number of neutral decays. The events classified as 201 form the material of this thesis. The events which contained up to one visible decay were classfied as common and those with two or more as rare. For all events the beam track was checked to be parallel to the other beam tracks to within 6°. Common events were accepted if the event was such that the production vertex was within region A and was produced by a beam track entering region A at the upstream end of the chamber and not through the sides and that the decay vertex was within region D. Rare events and τ decays were noted from anywhere in the chamber (region B).

Considering (ii), a neutral decay was considered associated



Dimensions in cms.

Fig. 2.2

with an event if a line between the two tracks of the neutral decay passed within 2 cm. of the production vertex. It was not regarded as a strange particle decay if one or both of the tracks from the decay was identified as an electron (i.e. the momentum was less than 140 Mev. and the track was minimum ionising) or the projected opening angle was less than 3° on two views and the ratio of the curvature of the positive track to that of the negative track was not 1:3.

Finally for (iii), the criterion was that the charged decay was measured if its projected decay length was greater than 3 mm. as seen under 10 times magnification.

The film was scanned three times. The first and second scans were independent and, in each, the frame number, topology of each event (except 000 events) and the region of rare events and τ decays were noted. For each event any electron pairs or neutron stars which could be associated with an event and all positive tracks which came from an event and stopped in the chamber (therefore being protons) were noted. The third scan was used to check the results of scan one and two and allow an estimate of the scanning efficiency to be made. During this scan, scan cards were made for events which were measurable and satisfied the above criteria. These cards contained the book-keeping information, a rough sketch of the event and approximate production and decay vertex positions to assist in the identification of the event

and any special measuring instructions.

The scanning stage of a conventional bubble chamber experiment is very important and if done efficiently ensures efficient measuring , statistically complete data, assistence in identifying the nature of events and an accurate estimation of the corrections to be applied to the cross sections due to the biases introduced by the scanning criteria.

Measuring forms the next part of this section. The events were measured on three views using the scan card information. The sequence of measurement on each view was to begin with a datum fiducial (fiducial 1) and then four other fiducials (2,3, 4, and5). See Fig.2.2. These fiducials were chosen because they gave the most accurate determination of the transformation parameters of the measurement system to a standard reference system. The rest of the event was then measured and each item (fiducial, track, vertex etc.) was labelled to allow a computer program to interpret the measurements of the items of the event.

2.2 Computing.

This part of the processing was done on the I.B.M. 7090 and 1401 computers at the Imperial College Computing Department and contains most of the complicated parts of the processing system. It can be divided in to four subsections each dealing with a particular program.

(a) The preparation of the measurement data for the

geometrical reconstruction program.

(b) Geometrical reconstruction (Geometry)[2.1].

(c) Kinematic reconstruction (Kinematics)[2.2].

(d) Statistics[2.3].

(a) The data preparation program.

This program was called P.I.N.G. and was modified and recoded by the author from the version used on the Mercury computer to a version for the I.B.M. 7090. It interpreted the magnetic tape image, produced by the I.B.M. 1401, of the paper tape output from the measuring machines, reassembled it into a format acceptable to geometry program and wrote this onto a magnetic tape which was called the Events Tape. It also carried out various checks on the data to ensure that the measurements were correctly sequenced and complete.

(b) The geometry program.

The geometry program read the events tape and with fixed data geometrically reconstructed the events and wrote the results onto a magnetic tape which was called the Geometry Library Tape. It also printed out the results in a condensed form which was known as the Geometry Output. This program forms part of the complete bubble chamber analysis system developed by the R.H.E.L. The fixed data required by the program consists of, for example, a range momentum table, magnetic field map and the optical constants of the chamber and cameras.[2.4]

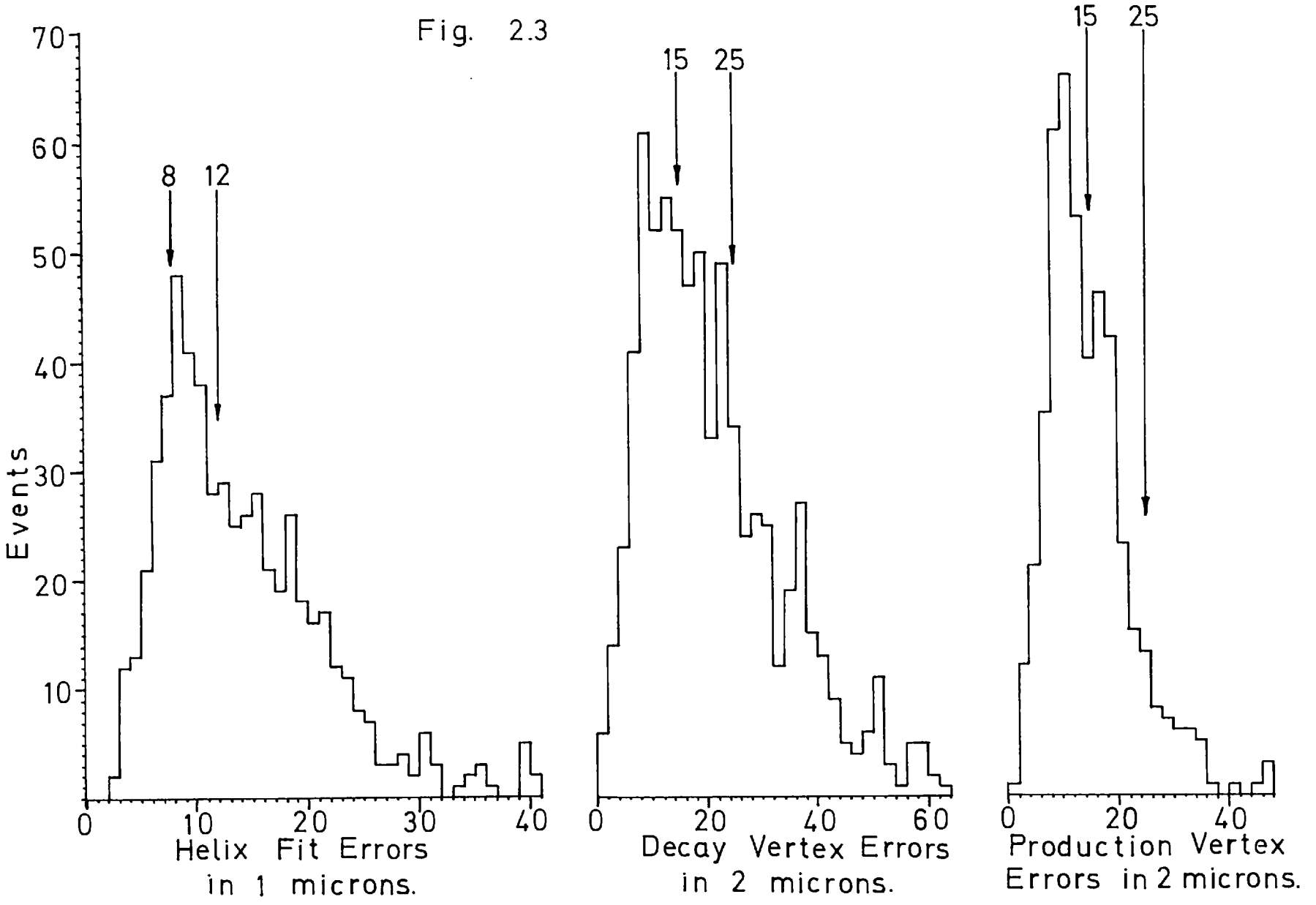
The spatial reconstruction of an event was done by firstly transforming the measurements of each view to a standard reference frame. This was necessary because of film shrinkage and measuring machine distortion. The transformation was done by a least squares fitting of the fiducial measurements to a set of expected fiducial positions. For each view the measured points were converted to rays using the optical constants then a circle was fitted by a least squares method to the points of intersection of the rays from the measured points along a track with the front glass of the chamber. Events were rejected at this stage if two points were more than a given distance from the fitted curve. The vertex coordinates were then spatially reconstructed by a least squares minimisation of the distances of a point in space from the rays of the three points measured on the three views of the film. This was later modified so that the rays from the point of intersection of the extrapolated tracks at a vertex on each view were used to define the vertex space point. The track points were then reconstructed in space using a corresponding points method. In this method the view on which the track had the maximum stereo angle with the track images on the other views was selected as a main view. The corresponding point was found by projecting a line parallel to the stereo axis from the main view to one of the other views and interpolating between the two points on the other view which were

either side of the projected line. The rays from these corresponding points defined a point in space. A corresponding point was then found for the other view and a weighted mean position of the space point was found. In general, because of optical distortions and track curvature, an iterative procedure and cicular interpolation were used. A series of space points were thus obtained and a fit was made to these in two parts. Firstly by fitting a parabola, cicle or straight line (according to the straightness of the track) to the x,y projections of the space points and secondly by fitting the z coordinate using a helix. The final fit was done iteratively using the parameters of the helix space fit as starting values and fitting a helix to the points of intersection of the space point rays with a nominal film plane. The first stage of the fitting procedure was used so that badly measured events were rejected quickly and starting values were obtained for the final stage. The method used in the final stage was because it avoided the awkward corresponding points method, the inability to calculate errors and the asymmetric treatment of the three views.(2.5)

The measurement errors were calculated from the error matrix and a standard r.m.s. error found from a histogram of the r.m.s. scatters of the measured points along each track about the fitted helix. The calculated value of the r.m.s. error was used if it was larger than a given check (12 microns.), otherwise a standard

error of 8 microns was used. The vertex errors were calculated from a weighted mean of the r.m.s. deviations of the space points from the rays from the measured points and from the rays from the points of intersection of the extrapolated tracks at the vertex. A standard value of 15 microns. was used for the vertex error if the calculated error was less than a given check of 25 microns, otherwise the caculated error after some iteration was used. The track and vertex r.m.s. scatter histograms are shown in Fig.2.3. The kinematic variables of each track were then calculated. These were the momentum (p),by using the magnetic field map, azimuthal angle (φ), and the dip angle λ. See Fig. 2.4. These are calculated at the centre of the track. The errors due to multiple coulomb scattering were added to the measurement errors. The formulae used were found by R. Böck from Monte Carlo calculations. The kinematic variables were used in the form $(1/p, \tan\lambda, \varphi)$. This was because 1/p was directly related to the measured curvature and facilitates easy error evaluation. Tanλ was used for convonience only. The final helix fit which was mass dependent was carried out with three different masses for the particle making the track (pion,kaon and proton). If the track was long or slow enough then the effect of the mass dependent energy loss showed itself in that the helix fit for the correct particle mass had a much smaller r.m.s. scatter of the measured points

Fig. 2.3


Events
70
60
50
40
30
20
10
0
10
20
30
40
8
12
Helix Fit Errors
in 1 microns.
0
20
40
60
15
25
Decay Vertex Errors
in 2 microns.
0
20
40
15
25
Production Vertex
Errors in 2 microns.

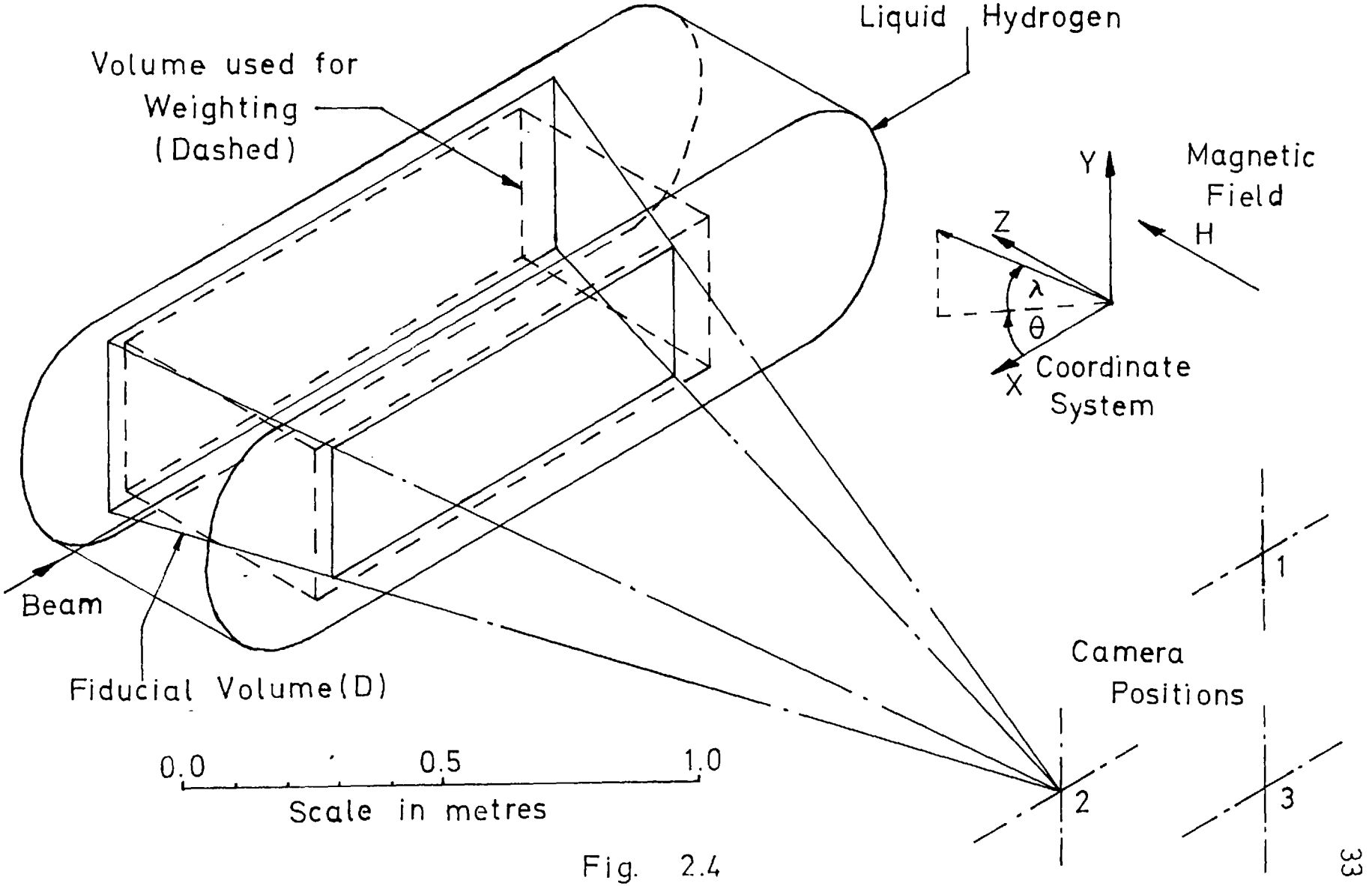

Liquid Hydrogen
Volume used for
Weighting
(Dashed)
Y
Magnetic
Field
H
Z
λ
θ
X
Coordinate
System
Beam
Fiducial Volume(D)
1
Camera
Positions
2
3
0.0
0.5
1.0
Scale in metres

Fig. 2.4

along the fitted curve than for the other particle masses. This allowed a particle to track identification to be made.

The geometry program calculated for each track of an event the variables $1/p$, $\tan\lambda$ and φ at the centre of each track and the associated errors, the three mass dependent helix fit r.m.s. scatters and the vertex positions with errors. This information then passed to the next program, the kinematics, by being written, in binary to keep the information compact, onto a geometry library tape. The geometry output was checked for quality of measurement and badly measured events were sent for re-measurement.

(c) The kinematics program.

Given the values of the kinematic variables of an event and the conservation of energy and momentum the kinematics program was presented with the problem of identifying the elementary particles which produced the tracks of an event. The solution made possible by the availability of fast computers was to perform a least squares fit to the many hypotheses of the interpretation of an event. The kinematic variables $(1/p, \tan\lambda, \varphi)$, specified at the centre of track, were used because they were then most likely to be normally distributed. This was because they were directly related to the measured points along each track. Normally distributed variables were required for the method of least sqares fitting with a χ^2 goodness of fit criteria. Centre of track variables were used

because this enabled easy multivertex fitting. Other information required by the kinematics program was some fixed data, for example, a range momentum table, particle masses and data defining the hypotheses fitting sequence.

The procedure of kinematic fitting was to minimise a modified χ^2 function which consisted of two parts. One was the true χ^2 function and the other part was a quantity which was a measure of the constraint unbalance (energy and momentum unbalance) of the fit. The complete function was:

$$M = \sum_{ij} (x_i - x_i^m)\, G^x_{ij}\, (x_j - x_j^m) + 2\sum_{\lambda} a_\lambda\, f_\lambda(x)$$

where $f_\lambda(x) = \sum_i e_i + \sum_i p_i$ and $G^x_{ij} = 1/\sigma^x_{ij}$

and a_λ = Lagrangian Multipliers

σ^x_{ij} = measurement error matrix.

For a minimum $\partial M/\partial x_i = 0$ and $\partial M/\partial a_\lambda$

i.e. $$\sum_j G^x_{ij}\, (x_j - x_j^m) + \sum_\lambda a_\lambda\, \partial f_\lambda/\partial x_i = 0$$

and $$f_\lambda(x) = 0$$

The constraint unbalance term was evaluated at each vertex, which meant that the kinematic variables had to be adjusted from their centre of track values to their values at the vertex. Each vertex has four constraint equations associated with it due to energy and momentum conservation . The number of constraints of a particular fit was reduced by one for each unmeasured variable. The equations were solved iteratively. A solution was regarded as acceptable if at a particular stage of iteration

$$\sum_{\lambda} f_{\lambda} < e_1$$

and $$\chi^2_{(n+1)} - \chi^2_{(m)} \; / \; \chi^2_{(m)} < e_2$$

where e_1 and e_2 were fixed tolerances.

Because there were in general a large number of hypotheses to be tested on a large number of events the rate of convergence to a suitable solution was very important. The method used was to allow the iterations to proceed until either the constraint unbalance increased twice, when the solution was rejected, or decreased to a minimum, when the solution was accepted as a reasonable fit. There was a maximum cut-off on the number of iterations allowed because it was possible for the values of the χ^2 to oscillate indefinitely. In these cases of oscillation a point can be made. It was noticed that in some cases of oscillation where a fit was not obtained the values of the χ^2 and constraint unbalance at some of the minima were acceptable. It would appear that in these cases a minima should be located and the fit at that stage be regarded as acceptable.

The procedure of fitting 201 events was divided into three parts. The first was the fitting of the decay vertex to a K° or Λ° decay. At the decay vertex only the K° or Λ° momentum was unknown and therefore the fit was a three constraint (3.C.) fit. The next part was the production vertex fit which used the value of the K° or Λ° momentum obtained from the decay vertex fit. In this part a fit to the production vertex of the various

hypotheses was attempted. This fit was a four constraint (4.C.) fit for hypotheses in which there were no missing particles at the production vertex. The hypotheses with a missing particle were 1.C. fits because there were then three components of momentum missing. The final part was to adjust all the kinematic variables simultaneously and obtain an overall multivertex fit. Events with two or more unseen particles could not be fitted and were classified as multineutral events.

This program calculated for each successful hypothesis tried on an event the fitted values of the variables with new errors, the ionisation, of each fitted track, as seen on view 2, the χ^2 and associated probability and the normalised stretch functions for each variable. The normalised stretch was defined as;

$$S = (x^f - x^m) / \sigma (x^f - x^m)_{rms}.$$

This should be normally distributed with a mean of zero for statistically unbiased fits. The 201 events were run through seven hypotheses only. These were chosen on the basis of an estimated cross section. The hypotheses used were;

$K^-p \longrightarrow K^\circ p \pi^-$, $K^\circ p \pi^+\pi^-$, $K^\circ n\pi^+\pi^-$, $\Sigma^\circ\pi^+\pi^-$, $\Lambda^\circ\pi^+\pi^-$, $\Lambda^\circ\pi^+\pi^-\pi^\circ$ and $\Lambda^\circ K^+K^-$.

The next stage of the analysis which could be regarded as part of the kinematics was the ionisation scanning. In this stage the ionisation given by the kinematics for each track was checked on the scanning table. The checking was done visually by

normalising to a nearby beam track. Also the hypothesis name and the χ^2 and probability for the decay vertex and multivertex fits for each hypothesis satisfying the ionisation were recorded. Common events not having a multivertex fit were regarded as multineutral versions of the common hypotheses consistent with the track ionisations observed. 201 events with fits were classified as unique if there were no other fits and ambiguous if there were other fits. Events with no fits were classified as Λ° type if there was only a Λ° fit, as K° type if there was only a K° fit and as ambiguous if there were both fits. K° type events were further divided into proton type if the positive track from production was identified as a proton, as pion type if it was identified as a pion and ambiguous if no identification was possible.

The kinematics libraries were then run through a program, written by L.K. Sisterson, which produced for each fit a card which contained information which uniquely defined the fit. This card was called a Choice Card. Using the ionisation information and the selection criteria discussed in Chapter 3 the fit or fits which were regarded as the correct interpretation of an event were selected by selecting the appropriate choice card running it, as data, with the kinematics library through a program called Inco. This program produced a Data Summary Tape (D.S.T.), which contained the kinematic quantities

associated with each selected fit.

(d) The statistics program.

This program deals with the final stage of the processing. The D.S.T. was run with fixed data, specifying the quantities to be histogrammed, through this program. The program was modified by the author to calculate logitudinal and transverse momenta and specialised scattering angles. The results obtained from processing the D.S.T. which contained the $\Lambda^{\circ}\pi^{+}\pi^{-}$ and $\Lambda^{\circ}\pi^{+}\pi^{-}\pi^{\circ}$ events through this program provide the material for the following chapters.

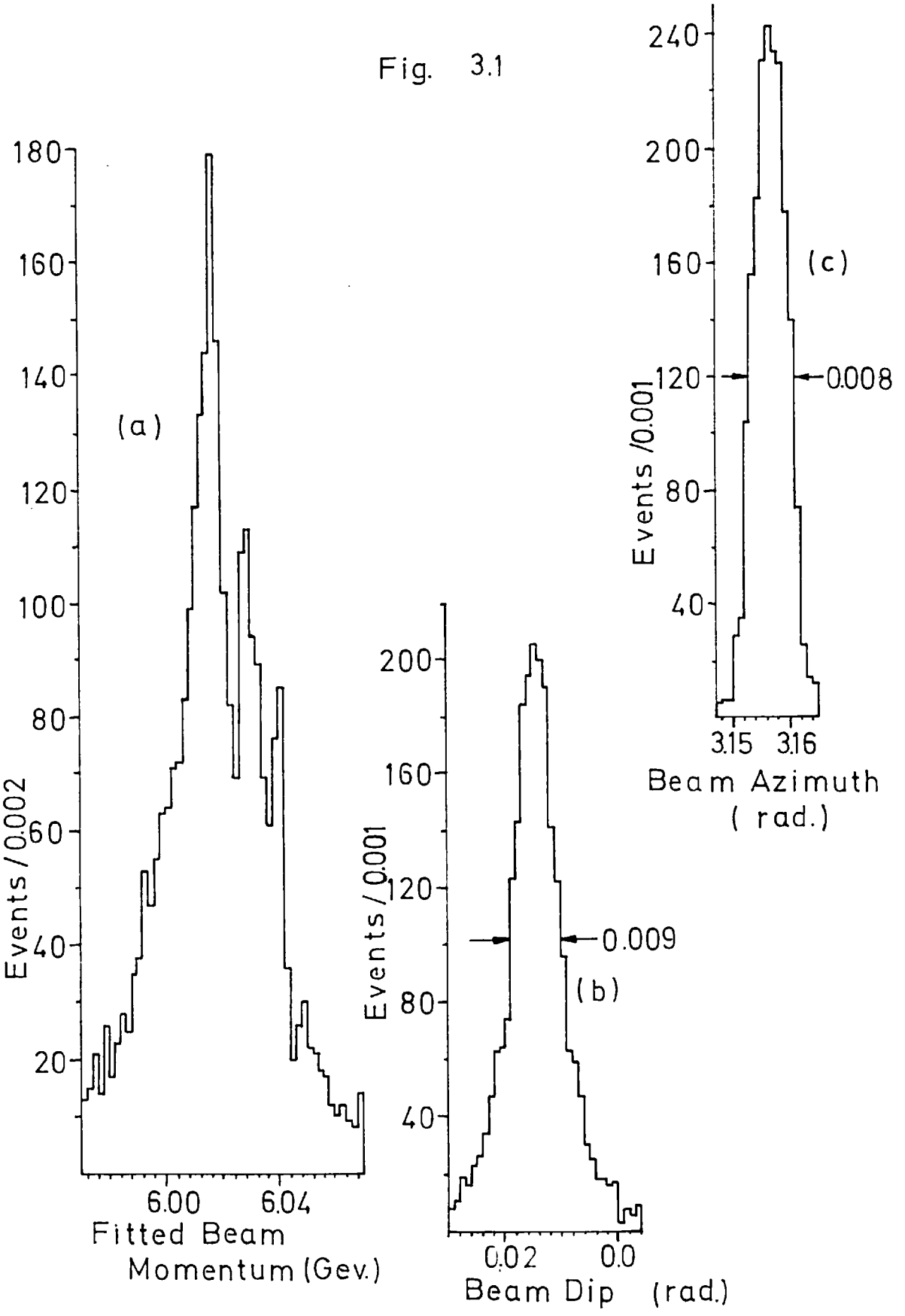
CHAPTER 3

In this chapter the experimental biases, errors, contamination, accuracy and cross sections will be discussed.

3.1 Biases due to the apparatus.

Firstly the beam is considered . The general angular definition of the beam can be seen from Fig. 3.1(b) and 3.1(c). The full width at half height for the dip angle (λ) was 9 ± 1 mrad. and for the azimuthal angle (φ) it was 8 ± 2 mrad. The azimuthal angular distribution has been approximately corrected for the effects of the sweeper magnet. The fitted beam momentum for the three runs is shown in Fig.3.1(a). Runs D and F used the same standard input value of the momentum. This distribution was modified by the effect of energy loss in the chamber. This spread the distribution by about 10 Mev. and reduced the central values by about 5 Mev. By applying these corrections the run D and F beam momentum was estimated to be 6.021 Gev. and the run E to be 6.037 Gev. Both values were in good agreement with the standard input values of 6.02 and 6.04 Gev. respectively. The error used for the beam momentum was 1 %. This allowed most of the events equal probability of fitting on the basis of beam momentum. For the main peak (runs D and F) the full width at half height was about 18 Mev. For the smaller run E peak the width was difficult to estimate but was about the same. The only bias which could be produced at this stage was to bias

Fig. 3.1


180
160
140
120
100
80
60
40
20
Events / 0.002
(a)
6.00
6.04
Fitted Beam
Momentum (Gev.)
200
160
120
80
40
Events / 0.001
0.009
(b)
0.02
0.0
Beam Dip (rad.)
240
200
160
120
80
40
Events / 0.001
(c)
0.008
3.15
3.16
Beam Azimuth
(rad.)

the distribution of the χ^2 probability of the kinematic fits to large values due to the large error on the beam momentum. Biases due to the bubble chamber will now be considered. The chamber, because of its finite size, has an immediate bias against observing the decays of particles with long lifetimes, intrinsically or because of their high momentum. The loss of the Λ° and K°'s was corrected for by a weighting factor of the form:

$$W = 1/ (1 - \exp.(-L_{max.}/pm\,\tau_o))$$

where L_{max} = the potential neutral path length in cms. (This was determined by the size of the fiducial volume. See Fig.2.4)

p = the momentum of the observed decaying particle in Gev.

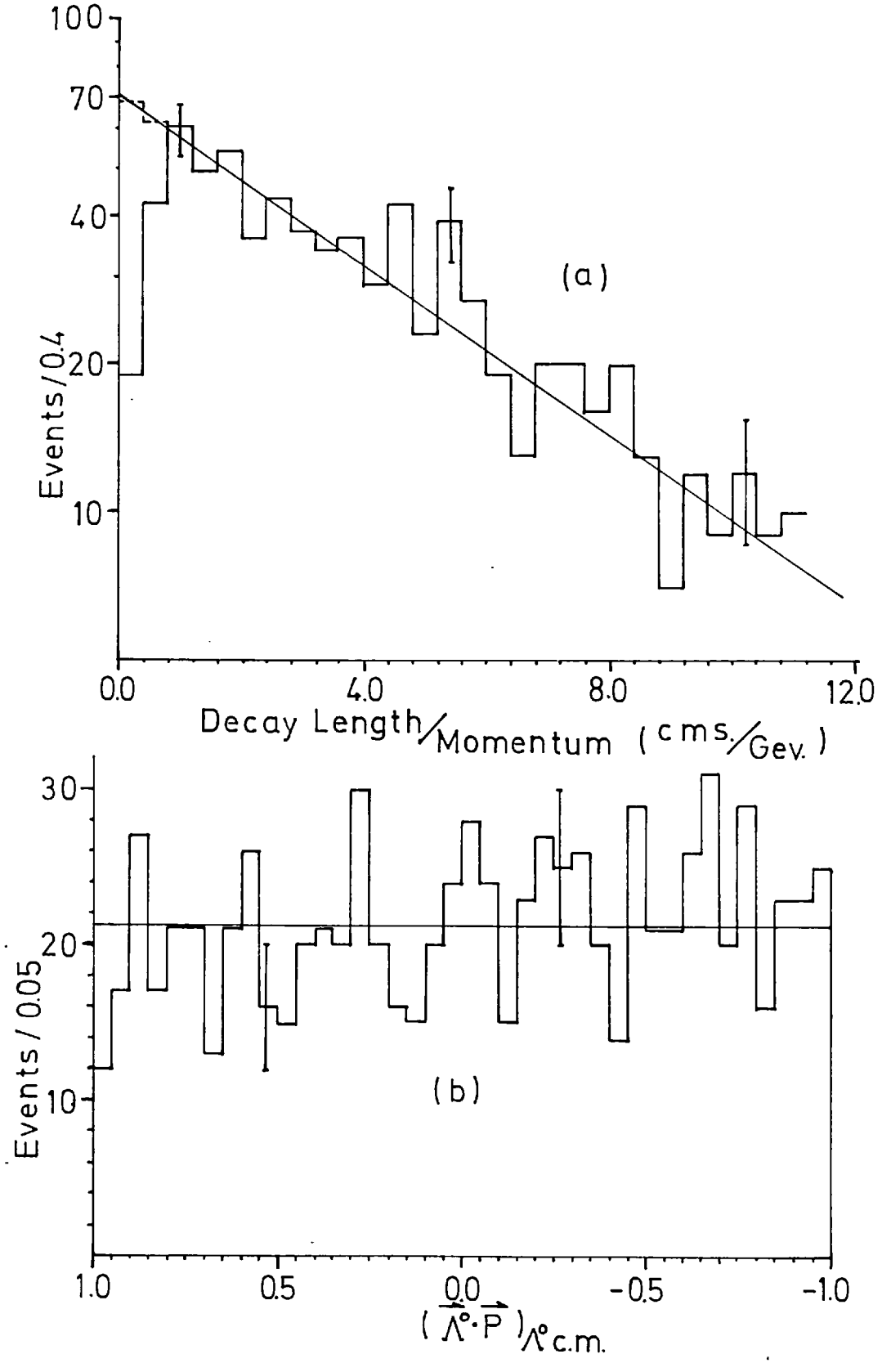
m = the rest mass of the decaying particle in Gev.

τ_o = the lifetime of the decaying particle in secs.

Each neutral decay observed was multiplied by this factor. There was ,however, a further bias which was introduced by the fact that decays close to the production vertex would appear as tracks coming from the production vertex. This loss in the case of neutral decays was corrected for by setting the 1 in the denominator of the weighting function equal to $\exp.(-L_{min.}/p\,m\,\tau_o)$. Where $L_{min.}$ = the minimum detectable decay length.

The value of $L_{min.}$ was set at 0.6 cms. in the chamber and was found from the lifetime plot. This is shown in Fig.3.2(a) for the Λ° particle. Because the Λ° particle decays exponentially a plot of the logarithm of the number (n) of events in which the

Fig. 3.2


100
70
40
20
10
Events/0.4
(a)
0.0
4.0
8.0
12.0
Decay Length/Momentum (cms./Gev.)
30
20
10
Events/0.05
(b)
1.0
0.5
0.0
-0.5
-1.0
$(\vec{\Lambda}^{\circ}\cdot\vec{P})_{\Lambda^{\circ}\,c.m.}$

Λ° decays within a given range of L/p against L/p is a straight line. The equation of the straight line is:

$$\log_e n = (L/p)\ /m\tau_o + \log_e n_o$$

where L = neutral path length in cms.

n_o = the number of decays with zero path length.

This line was extrapolated to L/p = 0 to obtain an estimate of the unobserved decays. The value obtained was $7 \pm 1\%$. The overall correction factor for the loss of Λ° particles was about 17%. The obvious loss of neutrally decaying neutral particles (i.e. $\Lambda^\circ \rightarrow n + \pi^\circ$) was corrected for by using the known branching ratios[3.1] of the Λ° decay. The values used were:

$\Lambda^\circ \rightarrow p + \pi^-$ = $66.4 \pm 1.1\%$ and $\Lambda^\circ \rightarrow n + \pi^\circ$ = $33.6 \pm 1.1\%$.

A more exact way to correct for the losses due to small and large decay lengths is to consider each final state as a separate sample, because the value of these losses will vary from process to process. This can be seen from the two body channels $Y_1^{*+}\pi^-$, $Y_1^{*+}\rho^-$ and $\Lambda^\circ\omega^\circ$ which were found to be very peripheral. The momentum of the Λ° in the laboratory for these channels can be very small (about 200 Mev.) and hence have small decay lengths. In this experiment this separate correction cannot be done because the number of events in these channels is too small (about 50 events). The method of correcting for decays outside the fiducial region was only approximate because the correcting factor calculated was the probability of the decay occurring

outside the fiducial region for an event in the same position in the chamber as the observed event. Hence the event should have an additional correction factor which is the probability that the event will occur in the same position in the chamber.

3.2 Biases due to scanning, measuring and programs.

The biases due to scanning were principally those from the scanning criteria and the loss of events due to the scanning efficiency. The calculation of the scanning efficiency was only approximate because the formula used assumed that each event was equally visible. This assumption can be expected to hold tolerably well in region A. The scanning efficiency for events considered in this thesis was about 1.0. The scanning criteria given in Chapter 2 were considered to give only a small bias against high momentum Λ° decays (more than 4 Gev.) in which the proton goes forward in the Λ° centre of mass, because this configuration will simulate an electron pair. Any bias in the Λ° decay configuration can be revealed by a study of the distribution of the polar angle of decay. This is defined in the Λ° centre of mass by ; $\text{Cos.}\,\theta_p = \vec{\Lambda^\circ} \cdot \vec{p}$

where $\vec{\Lambda^\circ}$ = a unit vector in the direction of the Λ°

$\vec{p}$ = a unit vector in the direction of the proton.

This distribution should be isotropic if there are no biases present. The distribution is shown in Fig. 3.2(b) and was found to be isotropic.

The procedure of measuring was not expected to produce any biases. The main biases produced at this stage will be due to the criteria used for the acceptance of the geometrical and kinematic reconstruction. The acceptance criteria used for the geometrical reconstruction were:

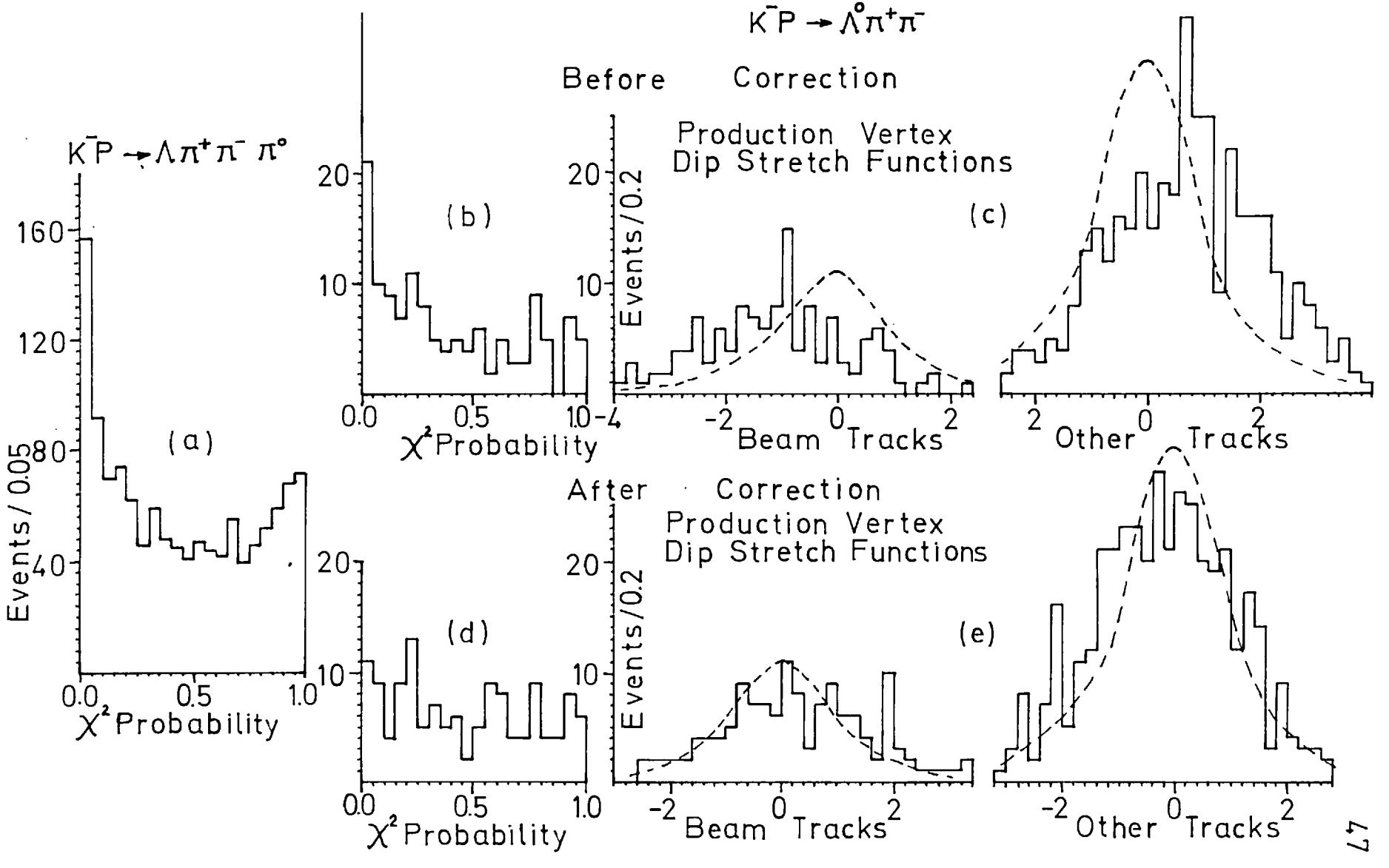
(a) The minimum helix fit errors were less than 25 microns.

(b) The errors on the track variables were less than 10%.

(c) The r.m.s. scatters of the vertices were less than 25 microns. These criteria necessarily reject events with tracks which are slow(about 100 Mev.) and those with a large dip angle (greater than 60°). Events with tracks of low momenta or large dip angles but which were otherwise well measured were accepted and were regarded as being impossible to be measured well. Any bias present was reduced to a negligible level by processing the events through at least two stages of remeasurement. The final result was that 98% of the measurable events had an acceptable geometry.

The errors used in the kinematical fitting of events were discussed in Chapter 2. The method used makes all events, except those with large errors, equally well measured which was a requirement of the fitting procedure used. It also gives a better estimate of the true error. The correctness of the errors can be seen from the χ^2 probability plots for the production vertex of the $\Lambda^{\circ}\pi^{+}\pi^{-}\pi^{\circ}$ fits to the 201 events shown in Fig.3.3(a).

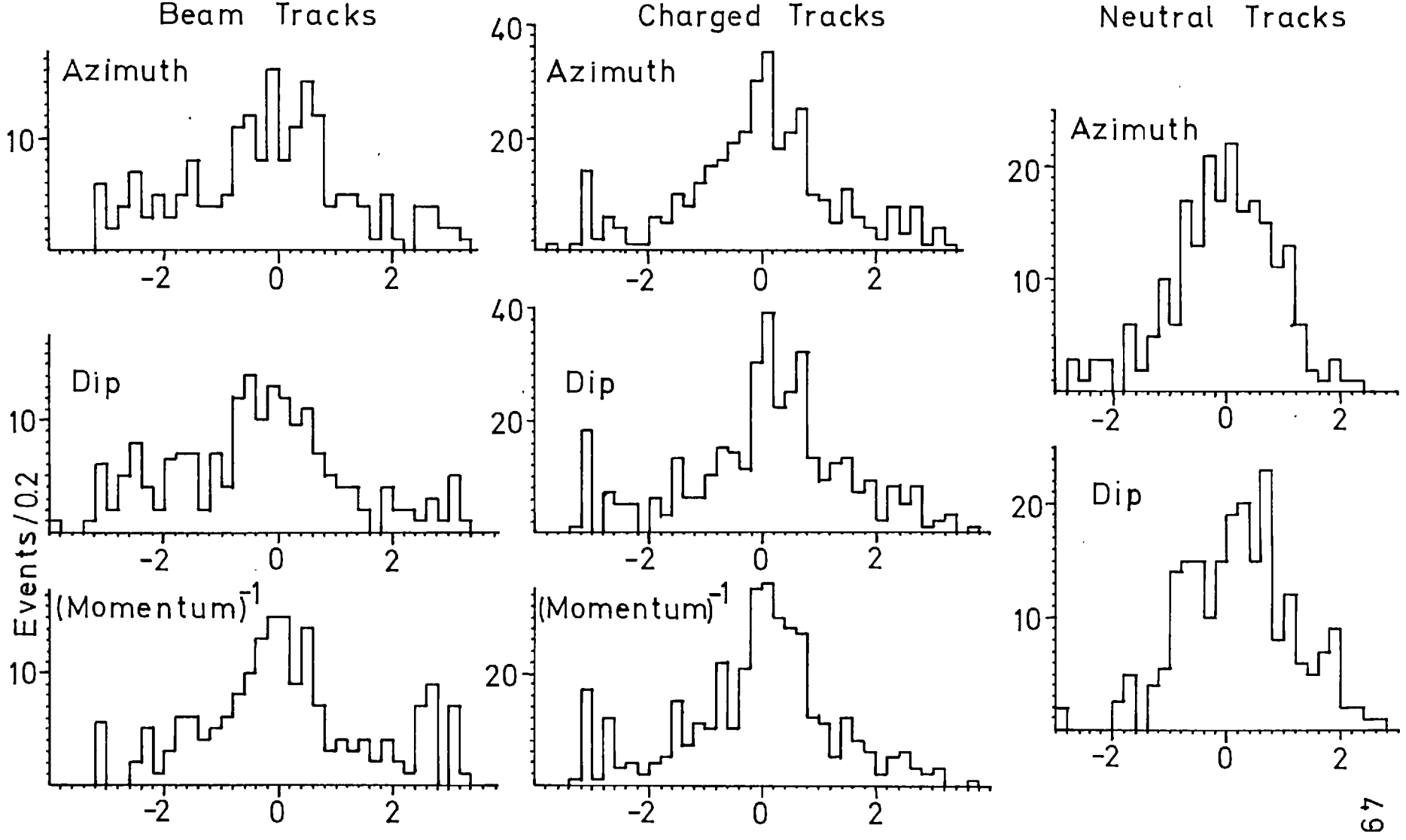
Fig. 3.3.


K⁻P → Λπ⁺π⁻ π°
Events / 0.05
(a)
χ² Probability
K⁻P → Λ°π⁺π⁻
Before Correction
Production Vertex
Dip Stretch Functions
(b)
(c)
Events/0.2
Beam Tracks
Other Tracks
After Correction
Production Vertex
Dip Stretch Functions
(d)
(e)

Any biases of the individual track variables can be revealed by plotting the normalised stretch functions of the production vertex fit for each variable. These distributions are shown in Fig. 3.4. The special highly constrained class of events fitting with no missing particle (i.e.4.C.) will be particularly sensitive to any biases. The probability distribution is shown in Fig.3.3(b) and the dip angle stretch functions in Fig.3.3(c). The probability distribution for the $\Lambda^{\circ}\pi^{+}\pi^{-}\pi^{\circ}$events shows a 15% peaking at low probability and an 8% peaking at the high probability extreme. Because of taking an average error some small equal peaking at each extreme is expected. Incorrect fits will produce a sharp peak at the low probability extreme. This was later found to be due to a large contamination (about 20%) of $\Lambda^{\circ}\pi^{+}\pi^{-}\pi^{\circ}\pi^{\circ}$events. The stretch functions for the 1.C. events ($\bar{K}^{\circ}\pi^{+}\pi^{-}n$, $\bar{K}^{\circ}p\,\pi^{-}\pi^{\circ}$, $\Lambda^{\circ}\pi^{+}\pi^{-}\pi^{\circ}$) show a normal distribution within statistics. An approximately normalised normal distribution is shown dotted. The 4.C. events, $\Lambda^{\circ}\pi^{+}\pi^{-}$, were strongly biased towards low probability. This was correlated with a strong bias of the beam dip stretch to negative values and the dip stretches of the other tracks to positive values. This effect was subsequently found to be due to a variation in the z-x plane of the coefficient of the second order correction term in the expression to correct for optical distortion which was used in the geometry program. This was most easily and quickly corrected

Fig. 3.4

Production Vertex Stretch Functions for 1.C. Fits.

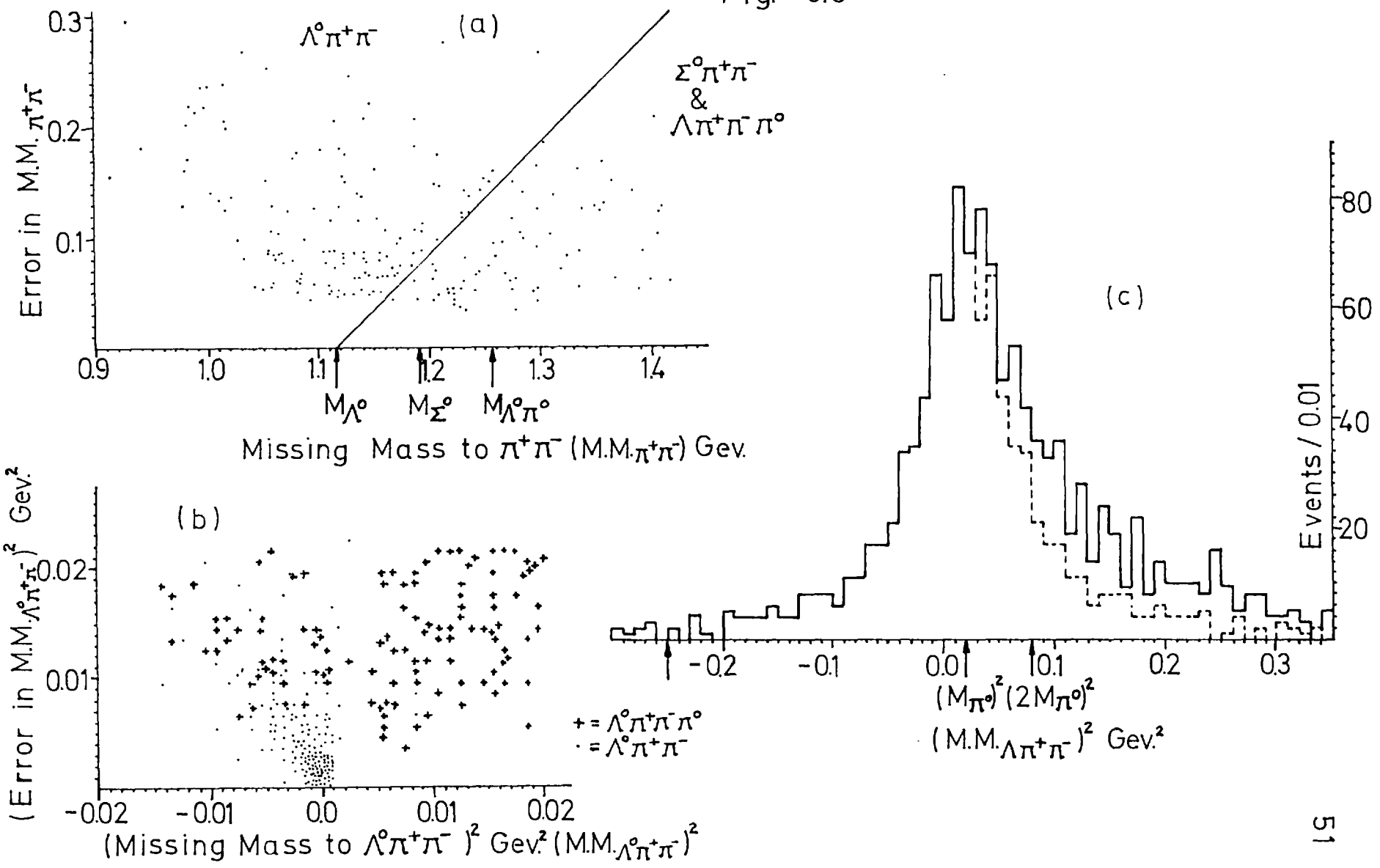


for by changing the beam dip by 0.3° (i.e. 2 standard deviations). The effect of this change can be seen from the distributions of probability and the dip stretches of the beam and other tracks shown in Figs. 3.3(d) and 3.3(e). This bias was equivalent to an extra transverse momentum of about 30 Mev. which reduced the resolution between Λ° and Σ° fits.

3.3 The separation and contamination of the $\Lambda^\circ\pi^+\pi^-$ and $\Lambda^\circ\pi^+\pi^-\pi^\circ$ final states.

The $\Lambda^\circ\pi^+\pi^-$ final state was separated in a special manner due to the bias of the beam dip and the large contamination (about 60%) by the $\Sigma^\circ\pi^+\pi^-$ events. Events which had a unique or ambiguous fit to $\Lambda^\circ\pi^+\pi^-$ or $\Sigma^\circ\pi^+\pi^-$ with a probability greater than 0.001 were run through a special set of programs which corrected the beam dip. The missing mass to the $\pi^+\pi^-$ was plotted against the error on this quantity. This plot is shown in Fig.3.5(a). A definite cone of events is seen about the Λ° mass. Events were classified as $\Lambda^\circ\pi^+\pi^-$ if they were on the low mass side of the high mass edge of this cone. The contamination of $\Sigma^\circ\pi^+\pi^-$ events in this sample was estimated to be about 13%. This was found from the asymmetry of events about the Λ° mass. The loss of $\Lambda^\circ\pi^+\pi^-$ events which did not fit because of the beam dip bias was very difficult to estimate, but was expected to be not greater than 20%. The general separation of $\Lambda^\circ\pi^+\pi^-$ events from $\Lambda^\circ\pi^+\pi^-\pi^\circ$ events can be seen

Fig. 3.5


(a)
Λ°π⁺π⁻
Σ°π⁺π⁻
&
Λπ⁺π⁻π°
Error in M.M.π⁺π⁻
0.3
0.2
0.1
0.9
1.0
1.1
1.2
1.3
1.4
MΛ°
MΣ°
MΛ°π°
Missing Mass to π⁺π⁻ (M.M.π⁺π⁻) Gev.
(b)
(Error in M.M.Λ°π⁺π⁻)² Gev.²
0.02
0.01
-0.02
-0.01
0.0
0.01
0.02
(Missing Mass to Λ°π⁺π⁻)² Gev.² (M.M.Λ°π⁺π⁻)²
+ = Λ°π⁺π⁻π°
· = Λ°π⁺π⁻
(c)
Events / 0.01
80
60
40
20
-0.2
-0.1
0.0
0.1
0.2
0.3
(Mπ°)² (2Mπ°)²
(M.M.Λπ⁺π⁻)² Gev.²

from the scatter plot of the missing mass to the $\Lambda^\circ\pi^+\pi^-$ against the error on this quantity for the $\Lambda^\circ\pi^+\pi^-$ and $\Lambda^\circ\pi^+\pi^-\pi^\circ$ fits. This is shown in Fig.3.5(b). The contamination of the $\Lambda^\circ\pi^+\pi^-$ events by the $\Lambda^\circ\pi^+\pi^-\pi^\circ$ events was thus considered to be negligible. No probability cut off was applied to the corrected $\Lambda^\circ\pi^+\pi^-$ events because the probability distribution was essentially flat.

The $\Lambda^\circ\pi^+\pi^-\pi^\circ$ events were selected with the following criteria:

(i) The production vertex fit probability was greater than 0.001.

(ii) There were no 4.C. common or rare fits.

(iii) 0.C. fits were rejected.

No probability ratio test was applied because a study, made by the author, of the probability distribution of events inconsistent with the observed ionisation showed that it was essentially the same as for the events consistent with the observed ionisation. The distribution of the $\Lambda^\circ\pi^+\pi^-$ and $\Lambda^\circ\pi^+\pi^-\pi^\circ$ fits among the other possible fits is shown in Table 3.1 for Imperial College only.

TABLE 3.1

UNIQUE FITS		AMBIGUOUS FITS				
$\Lambda^\circ\pi^+\pi^-$	$\Lambda^\circ\pi^+\pi^-\pi^\circ$	$\Lambda^\circ\pi^+\pi^-$ $\Sigma^\circ\pi^+\pi^-$	$\Lambda^\circ\pi^+\pi^-\pi^\circ$ $\Sigma^\circ\pi^+\pi^-$	$\bar{K}^\circ\pi^+\pi^-n$ $\Lambda^\circ\pi^+\pi^-\pi^\circ$	$\bar{K}^\circ p\pi^-\pi^\circ$ $\Lambda^\circ\pi^+\pi^-\pi^\circ$	$\bar{K}^\circ p\pi^-\pi^\circ$ $\bar{K}^\circ n\pi^+\pi^-$ $\Lambda^\circ\pi^+\pi^-\pi^\circ$
19	255	35	13	11	4	3

A study of the ambiguous events showed that the events ambiguous between the $\Lambda^\circ\pi^+\pi^-\pi^\circ$ and $\Sigma^\circ\pi^+\pi^-$ hypotheses were in most cases $\Sigma^\circ\pi^+\pi^-$ events. This fact also shows that there was a strong kinematic overlap between the $\Lambda^\circ\pi^+\pi^-\pi^\circ$ and $\Sigma^\circ\pi^+\pi^-$ events. It is seen from Table 3.1 that the problem of $\Lambda^\circ\pi^+\pi^-\pi^\circ$ ambiguities was small and so the ambiguous events were neglected except for cross section calculations when they were given a weight of 1/2. The correction factor for the $\Lambda^\circ\pi^+\pi^-\pi^\circ$ and $\bar{K}^\circ\pi^+\pi^-$ n ambiguities was 2.5% for the missing mass cuts used.

The contamination of the $\Lambda^\circ\pi^+\pi^-\pi^\circ$ events by $\Lambda^\circ\pi^+\pi^-\pi^\circ\pi^\circ$ events was estimated from a study of the distribution of the square of the missing mass for events fitted as $\Lambda^\circ\pi^+\pi^-\pi^\circ$. This distribution is shown in Fig.3.5(c). The events plotted have a three standard deviation cut off applied to the missing mass squared (i.e. $M^2_{\pi^\circ} - 3\varepsilon(M.M.)^2 < M.M.^2 < M^2_{\pi^\circ} + 3\varepsilon(M.M.)^2$). The distribution was seen to be strongly biased to the high mass side which indicated $\Lambda^\circ\pi^+\pi^-\pi^\circ\pi^\circ$ contamination. A quantitative estimate of the contamination was made by evaluating the asymmetry of the distribution about the position of the neutral pion mass squared. It was found to be 25 ± 5 %. A mass cut was applied to these events such that only events with $0.25 < M.M.^2 < 0.08$ Gev.^{2} were accepted. This produced a sample of events in which there was a loss of about 20% of true $\Lambda^\circ\pi^+\pi^-\pi^\circ$ events and a contamination of about 5%. This cut off

will produce a small bias against events with high momentum neutral pions because of the bad pion mass determination. There will be an unknown contamination from the $\Sigma^\circ\pi^+\pi^-\pi^\circ$ events. These events will tend to produce a bias to large neutral pion masses and will therefore be reduced to some extent by the missing mass cuts given above.

3.4 Cross sections.

The effective micro-barn equivalent for the final states $\Lambda^\circ\pi^+\pi^-$ and $\Lambda^\circ\pi^+\pi^-\pi^\circ$ was evaluated for the sample of events processed at Imperial College. Two methods were used. One was to use the number of τ decays found in region A and the other was to use the value of the total cross section for K^-p interactions at 6 Gev.

(i) The τ count method.

The number of τ decays found in region A after correcting for a scanning efficiency of 91% was N_τ where:

$$N_\tau = 469 \pm 20$$

The total number of τ's passing through region A (N_{o_τ}) is given by: $N_{o_\tau} = N_\tau / (1 - \exp.(-t/t_o)) \cong N_\tau\, t_o / t$

where t = the time of flight of the K^- through region A

and t_o = the lifetime of 6 Gev. K^- mesons.

Using the accepted value of K^- mass (0.494 Gev.):

$$t = 3 \text{ nsecs. and } N_{o_\tau} = 93{,}800.$$

Only 5.6 % [3.1] of the K^- mesons decay via the τ mode and decay

involving one or more neutral pions will produce 0.3% of Dalitz pairs which will simulate decays. These considerations change the τ decay branching ratio to 5.9%. This now allows the total number of K^- mesons passing through region A to be found. The cross section for one event (micro-barn equivalent) is defined as: $\sigma = 10^{34} / \rho A L$ in μbns.

where ρ = the density of hydrogen at 27°K.(0.0625 grm/cc.)

A = Avagadros number.(6.023×10^{23} mols./grm.mol.)

L = the mean free path.(total K^- path length in cms.)

Hence $\sigma = 0.742 \pm 0.04$ μbns.

The main error was due to the uncertainty in the number of τ decays.

(ii) The total cross section method.

The total number of interactions observed in region A was N_t, where: $N_t = 33{,}900$. This number includes an approximate estimate of the number of unscanned 000 events and unseen small angle elastic scatters. From counter experiments[3.2] the total cross section at 6 Gev. is 24 mbns. Assuming an average pion contamination of 5% the micro-barn equivalent is given by: $\sigma = 24 / N_{t\,cor.} = 0.738 \pm 0.003$ μbns.

This is in good agreement with the value obtained by the other method. The micro-barn equivalent for the complete data of the collaboration was found by using the numbers of events processed by the other groups and extrapolating the above value of σ.

The micro-barn for the collaboration was found to be

$$0.18 \pm 0.03 \ \mu\text{bns}.$$

For each of the final states $\Lambda^\circ\pi\ \pi$ and $\Lambda^\circ\pi\ \pi\ \pi^\circ$ by considering the losses and contaminations discussed earlier in this chapter an effective micro-barn equivalent can be found so that given the number of events in any channel a simple multiplication by this factor yields the corresponding cross section. For the $\Lambda^\circ\pi^+\pi^-$ events the value was 0.43 ± 0.1 bns. and for the $\Lambda^\circ\pi^+\pi^-\pi^\circ$ events it was 0.41 ± 0.05 μbns.

3.5 Resolution.

The basic factors which determine the resolution of any mass distribution are the accuracy of the measurement of the momentum of the charged tracks and the ratio of the rest mass to the momentum for the particles in the mass combination. The accuracy of measurement of the momentum of two pions was estimated from the width of the K° measured mass distribution. An ideogram (smooth curve) and histogram of the K° mass squared are shown in Fig3.6(a). The width was 16 ± 2 Mev. This will be the approximate resolution of the $\pi^+\pi^-$ effective mass distributions. The resolution of the $\pi^+\pi^-\pi^\circ$ distribution was found from the width of the ω° peak to be about 30 Mev. The resolution of the $\pi^\pm\pi^\circ$ distributions will be worse because there is only one charged track. This was estimated to be about 35 Mev. The accuracy of measuring the proton and pion

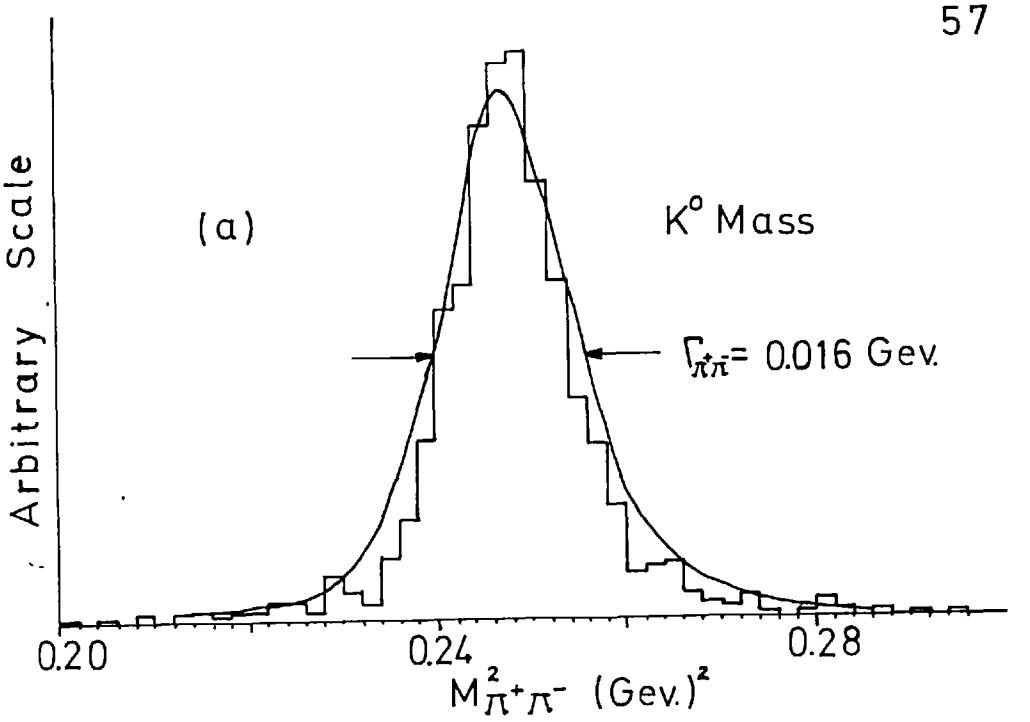
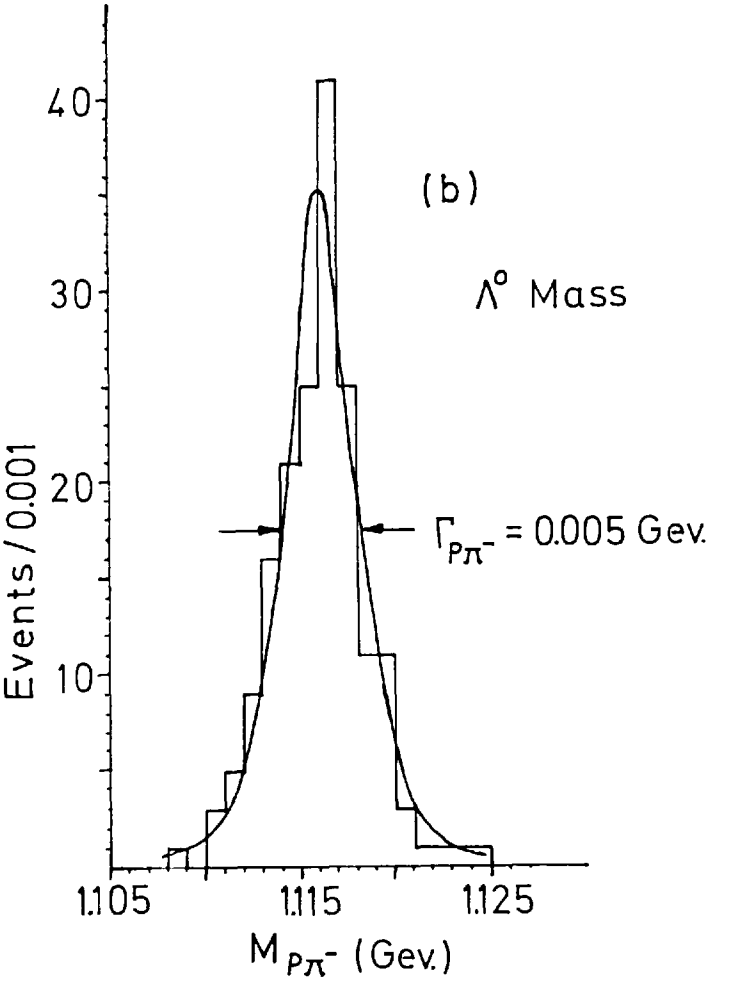

Arbitrary Scale
(a)
K° Mass
$\Gamma_{\pi^+\pi^-}$= 0.016 Gev.
0.20
0.24
0.28
$M^2_{\pi^+\pi^-}$ (Gev.)²

Fig. 3.6


Events / 0.001
40
30
20
10
(b)
Λ° Mass
$\Gamma_{P\pi^-}$ = 0.005 Gev.
1.105
1.115
1.125
$M_{P\pi^-}$ (Gev.)

momenta was found from the width of the measured Λ° mass distribution. This is shown in Fig. 3.6(b). The width was estimated to be about 5 Mev. It was small because the tracks from the Λ° decay were slow and the ratio of the proton mass to its momentum was large. The resolution of the $\Lambda^\circ\pi^\pm$ and $\Lambda^\circ\pi^+\pi^-$ distributions will be somewhat worse than this because of the adjustment of the Λ° momentum when a fit is made and was estimated to be 10 - 15 Mev. The resolution of the $\Lambda^\circ\pi^\pm\pi^\circ$ distribution was estimated to be about 20 - 25 Mev. and the $\Lambda^\circ\pi^\circ$ to be 30 - 35 Mev. These were larger because of the uncertainty in the determination of the neutral pion mass.

CHAPTER 4

In this chapter the final state $\Lambda^{\circ}\pi^{+}\pi^{-}$ will be described and the definitions of the kinematic variables and reference systems used in this and the following chapters will be given.

4.1 Kinematic variables.

The variable used for the investigation of mass correlations (resonances) between particles and combinations of particles in a given final state is the "effective mass". This variable is Lorentz invariant and is usually plotted as a histogram or ideogram. It is defined by the expression:

$$M^{2}_{eff.} = \left(\sum e_n \right)^2 - \left(\sum p_n \right)^2$$

where n = the number of particles in the combination

$M_{eff.}$ = the effective mass.

e_n = the energy of the n^{th} particle

and p_n = the momentum of the n^{th} particle.

The internal configuration of a three body final state is completely defined by a point on a "Dalitz Plot". A form of the Dalitz plot is a scattergram of the square of the effective masses of any two of the different two body combinations. That is :

$$\left(M_{eff.} \right)^2_{1,2} \quad \text{vs.} \quad \left(M_{eff.} \right)^2_{1,3}$$

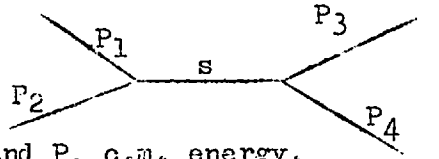
or $$\left(M_{eff.} \right)^2_{1,2} \quad \text{vs.} \quad \left(M_{eff.} \right)^2_{2,3}$$

or $$\left(M_{eff.} \right)^2_{1,3} \quad \text{vs.} \quad \left(M_{eff.} \right)^2_{2,3}$$

A statistical theory for the production process predicts that the density of points on the Dalitz plot is constant. Hence any resonance production is immediately apparent as a variation in the density of points. This plot will also show any interference effects between resonances.

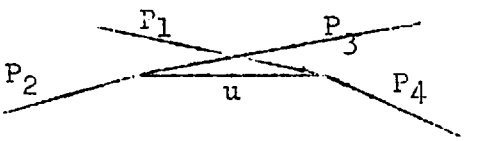
The field theoretic description of strong interaction production processes is based on "Feynman Graphs" and the formalism developed by Mandlestam and others.[4.1] The variables defined by Mandlestam are :

(1) The 's' variable



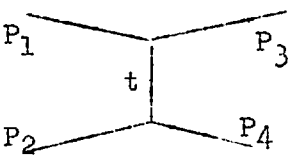
$$s = (P_1 + P_2)^2 = (P_3 + P_4)^2$$
$$= (e_1 + e_2)^2 - (p_1 + p_2)^2 = P_1 \text{ and } P_2 \text{ c.m. energy.}$$

(2) The 'u' variable



$$u = (P_1 - P_4)^2 = (P_2 - P_3)^2$$
$$= (e_1 - e_4)^2 - (p_1 - p_4)^2 = \text{four momentum transfer } P_1 \text{ to } P_4$$

(3) The 't' variable



$$t = (P_1 - P_3)^2 = (P_2 - P_4)^2$$
$$= (e_1 - e_3)^2 - (p_1 - p_3)^2 = \text{four momentum transfer } P_1 \text{ to } P_3$$

where P_i = the four momentum of the i^{th} particle

m_i = the i^{th} particle rest mass

e_i = the energy of the i^{th} particle

p_i = the three momentum of the i^{th} particle

and $i = 1 \quad 4$

These relations provide three independent four vectors and two

independent scalar variables. The first is due to four momentum conservation and the other from the relation :

$$s_1 + s_2 + s_3 = m_1^2 + m_2^2 + m_3^2 + m_4^2$$

where the s_i's are made up from the three independent four momenta. Because of the dominance of the peripheral production mechanisms at high energy the t variable is most widely used. More fully this is ;

$$t = e_1^2 + e_3^2 - 2e_1e_3 - p_1^2 - p_3^2 + 2\vec{p}_1 \cdot \vec{p}_3$$
$$= m_1^2 + m_3^2 - 2\, e_1e_3 + 2\, \vec{p}_1 \cdot \vec{p}_3$$

In the physical region t is negative, but can become positive if $m_1 > m_3$ or $m_2 > m_4$.

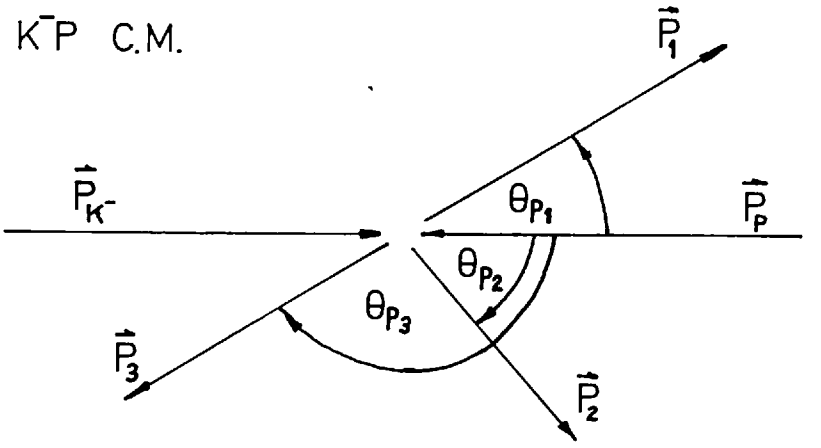
4.2 Angular distributions.

The angles which are used to describe the configuration of the final state are defined in two reference frames. One is the overall centre of mass (i.e. the K^-p centre of mass) and the other is the centre of mass of a particular combination of particles. The angles used in each reference frame are shown in Fig. 4.1.

In the K^-p centre of mass there is only one angle. This angle is the production angle of a particle or combination of particles (denoted by c) and is given by :

$$\text{Cos.}(\theta_p)_c = \vec{p}_c \cdot \vec{p}_{K^-}$$

where $\vec{p}_c$ and $\vec{p}_{K^-}$ are unit vectors in the direction of the particle or combination of particles and of the incident K^- respectively.


K⁻P C.M.
$\vec{P}_1$
$\vec{P}_{K^-}$
θ_{P_1}
$\vec{P}_P$
θ_{P_2}
θ_{P_3}
$\vec{P}_3$
$\vec{P}_2$

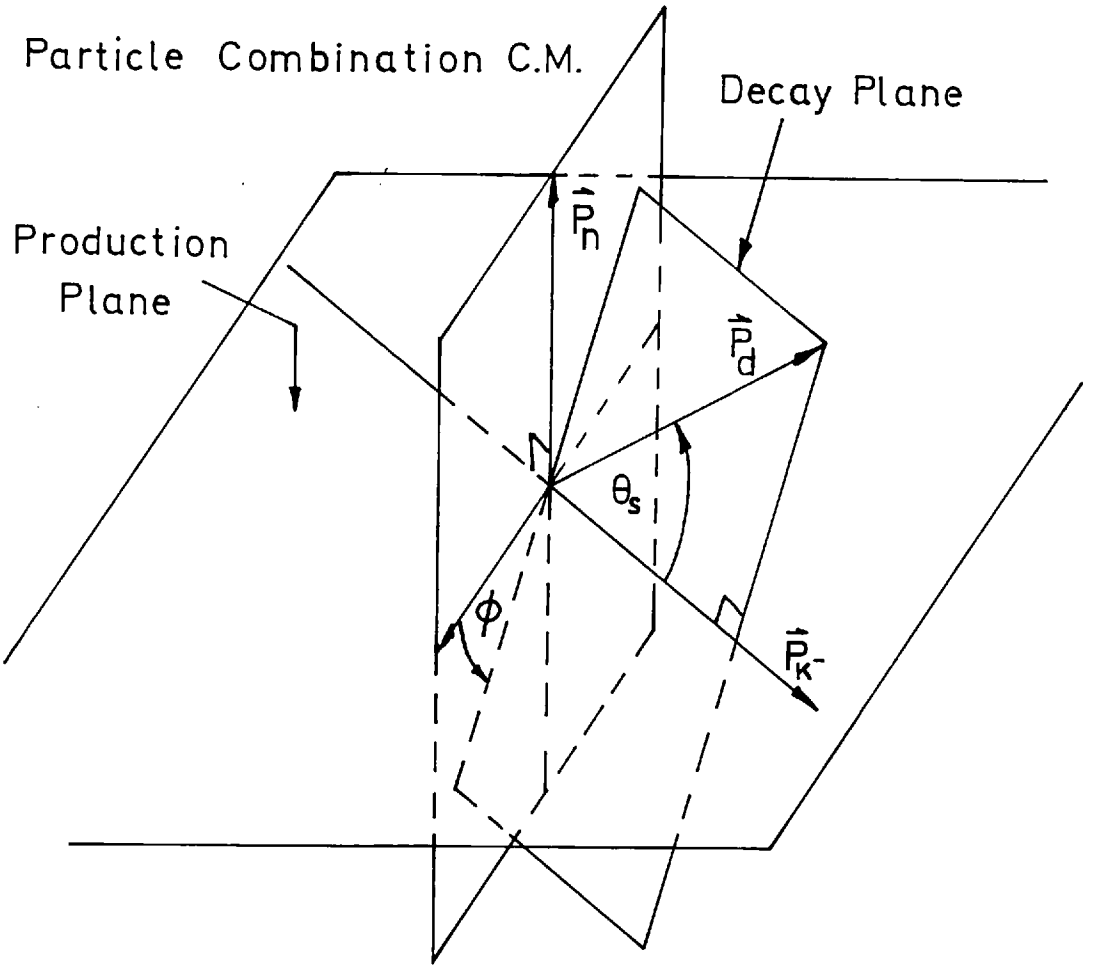

Particle Combination C.M.
Decay Plane
Production Plane
$\vec{P}_n$
$\vec{P}_d$
θ_s
ϕ
$\vec{P}_{K^-}$

Fig. 4.1

In the centre of mass of the combination of particles there are two angles. These are :

(1) The scattering angle. For a two particle combination the direction of one of the particles is used in the definition of these angles. For a three particle combination the normal to the plane containing the three particles is used.

$\text{Cos.}\ (\theta_s)_c = \vec{p}_d \cdot \vec{p}_{K^-}$ — for a combination not containing a baryon.

$\text{Cos.}\ (\theta_s)_c = \vec{p}_d \cdot \vec{p}_p$ — for a combination containing a baryon.

(2) The azimuthal angle.

$$\varphi_c = \tan^{-1}\left[\frac{\vec{p}_d \cdot \vec{p}_n}{(\vec{p}_n \times \vec{p}_{K^-}) \cdot \vec{p}_d}\right]$$ for a non-baryon combination.

$$\varphi_c = \tan^{-1}\left[\frac{\vec{p}_d \cdot \vec{p}_n}{(\vec{p}_n \times \vec{p}_p) \cdot \vec{p}_d}\right]$$ for a baryon combination.

This definition of φ_c means that when $\varphi_c = 0$ the decay plane coincides with the production plane. The additional symbols used are: $\vec{p}_d$ = a unit vetor in the direction of one of the particles from a two body combination or the normal to the three body decay plane.

$\vec{p}_p$ = a unit vector in the direction of the proton.

$\vec{p}_n$ = a unit vector in the direction of the normal to the production plane.

4.3 The final state $\Lambda^\circ\pi^+\pi^-$.

The cross section for this final state was 71 ± 20 μbns. which represented 177 events. The error on the cross section was large due to uncertainties in the estimation of contamination and program losses. The contamination from $\Sigma^\circ\pi^+\pi^-$ events was $13 \pm 5\%$ with a loss of about 5%. The Dalitz plots of $(M_{\Lambda^\circ\pi^+})^2$ vs. $(M_{\Lambda^\circ\pi^-})^2$ and $(M_{\Lambda^\circ\pi^+})^2$ vs. $(M_{\pi^+\pi^-})^2$ are shown in Fig. 4.2(a) and 4.2(b) respectively. These plots show a strong $Y_1^{*+}(1385)$ resonance band. This was approximately 25% of this final state. There was a small amount of ρ° production and a broad enhancement at about 3.0 Gev.^{2} in the $\Lambda^\circ\pi^+$ mass combination. From the Dalitz plots it can be seen that the effects of interference between resonance bands can be ignored. The $\Lambda^\circ\pi^+$ and $\pi^+\pi^-$ masses tend to be small. This effect is due to the strong peripherality of the Λ° and π^- which restricts the events to the region of the Dalitz plot where $M_{\Lambda^\circ\pi^-}$ is large and hence $M_{\Lambda^\circ\pi^+}$ and $M_{\pi^+\pi^-}$ are small. The $\Lambda^\circ\pi^+$, $\Lambda^\circ\pi^-$ and $\pi^+\pi^-$ effective mass distributions with various resonance subtractions are shown in Figs. 4.3(b), 4.3(c) and 4.3(d) respectively. The $\Lambda^\circ\pi^+$ distribution shows the $Y_1^{*+}(1385)$ clearly and a 2.5 standard deviation enhancement at approximately 1.720 Gev. A maximum likelihood fit was made to the $\Lambda^\circ\pi^+$ effective masses.(4.2) The results are shown in Table 4.1 and the fitted curve in Fig. 4.4(d).

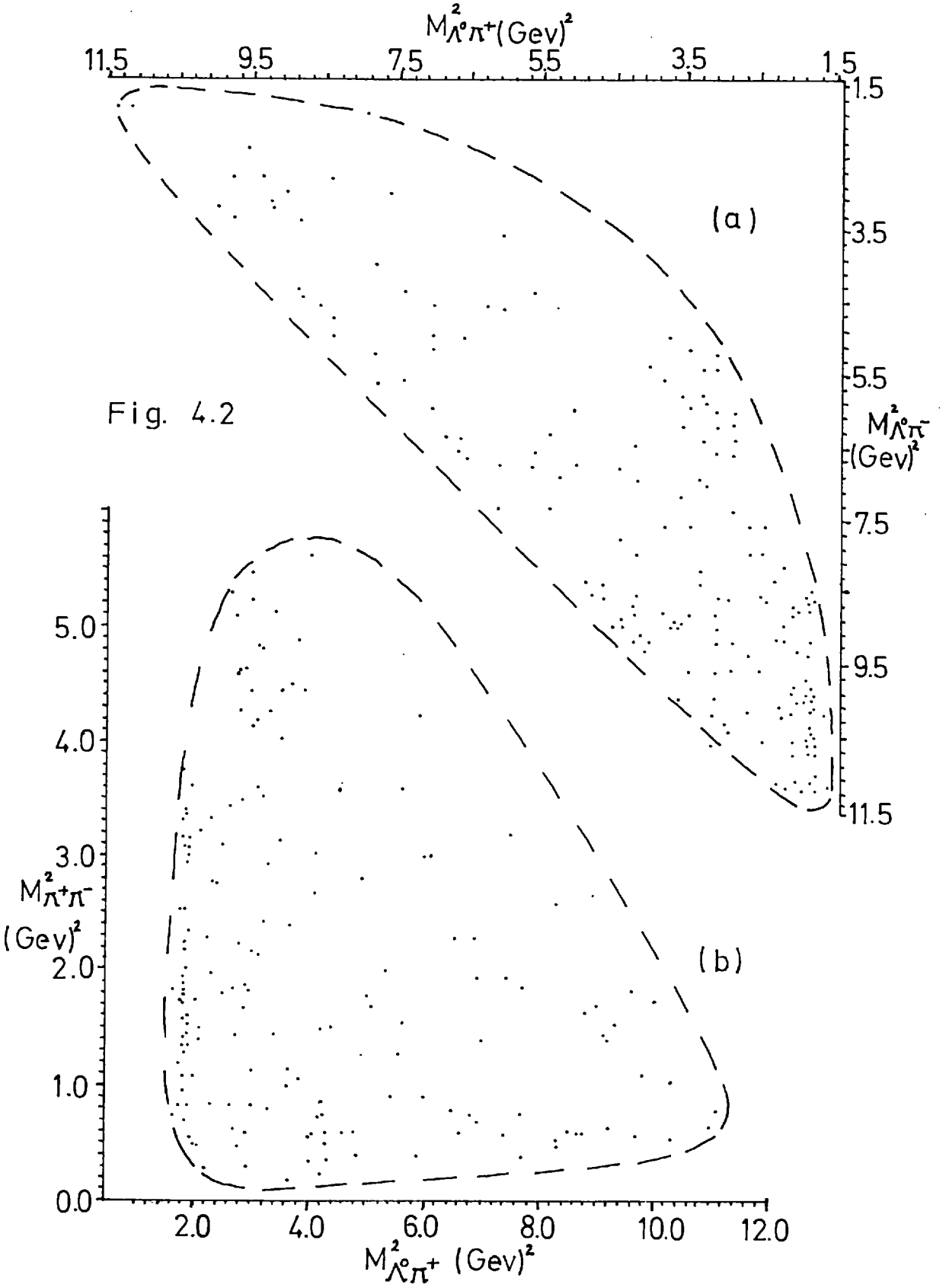

$M^2_{\Lambda^0\pi^+}$(Gev)^2
11.5
9.5
7.5
5.5
3.5
1.5
(a)
$M^2_{\Lambda^0\pi^-}$ (Gev)^2
(b)
$M^2_{\pi^+\pi^-}$ (Gev)^2
5.0
4.0
3.0
2.0
1.0
0.0
2.0
4.0
6.0
8.0
10.0
12.0
$M^2_{\Lambda^0\pi^+}$ (Gev)^2

Fig. 4.2

Fig. 4.3

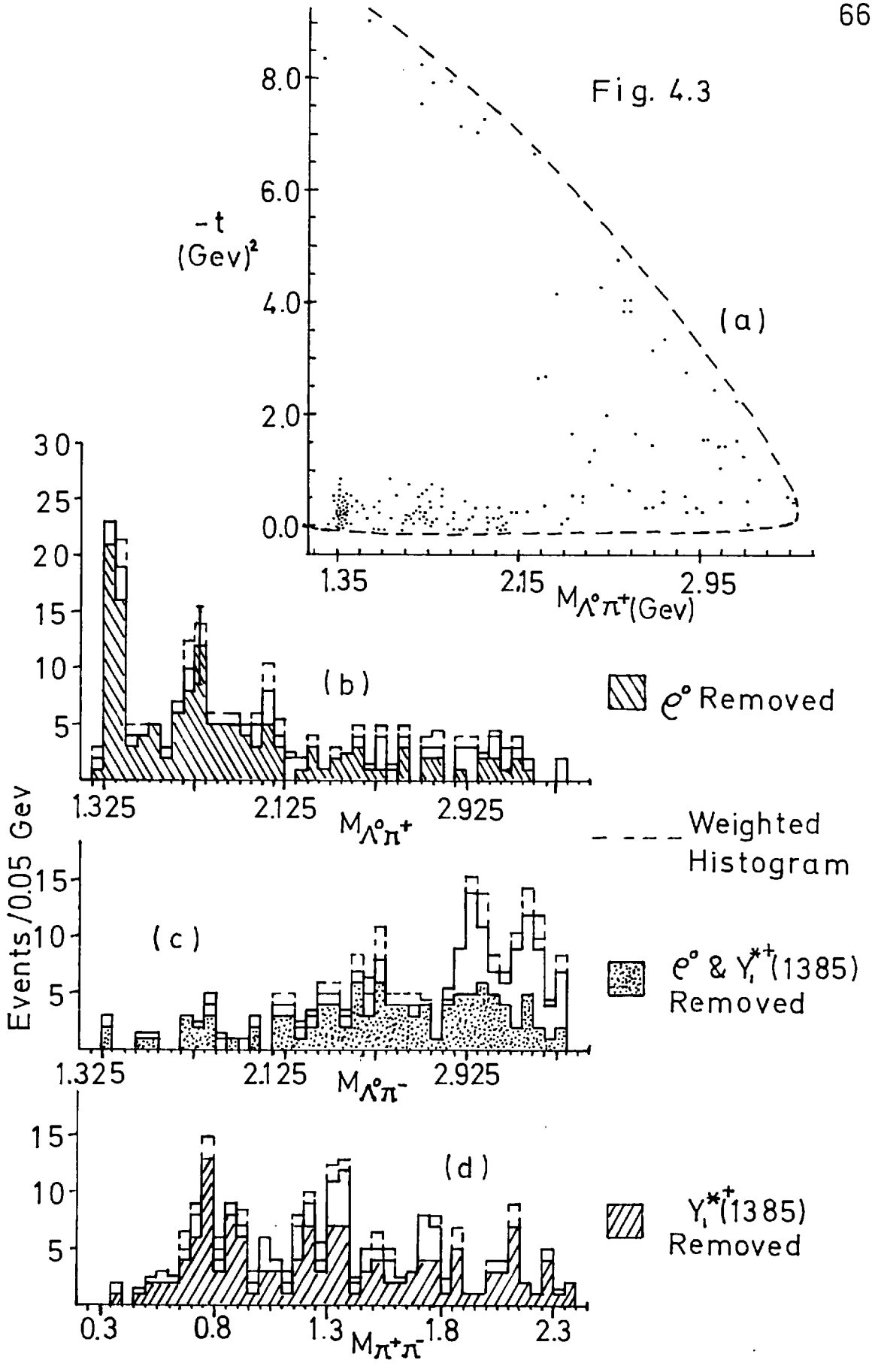

8.0
6.0
4.0
2.0
0.0
-t
(Gev)²
(a)
1.35
2.15
2.95
M Λ°π⁺(Gev)
30
25
20
15
10
5
(b)
1.325
2.125
2.925
M Λ°π⁺
ℓ° Removed
Weighted Histogram
Events/0.05 Gev
15
10
5
(c)
1.325
2.125
2.925
M Λ°π⁻
ℓ° & Y₁*⁺(1385) Removed
15
10
5
(d)
0.3
0.8
1.3
1.8
2.3
M π⁺π⁻
Y₁*⁺(1385) Removed

Fig. 4.4

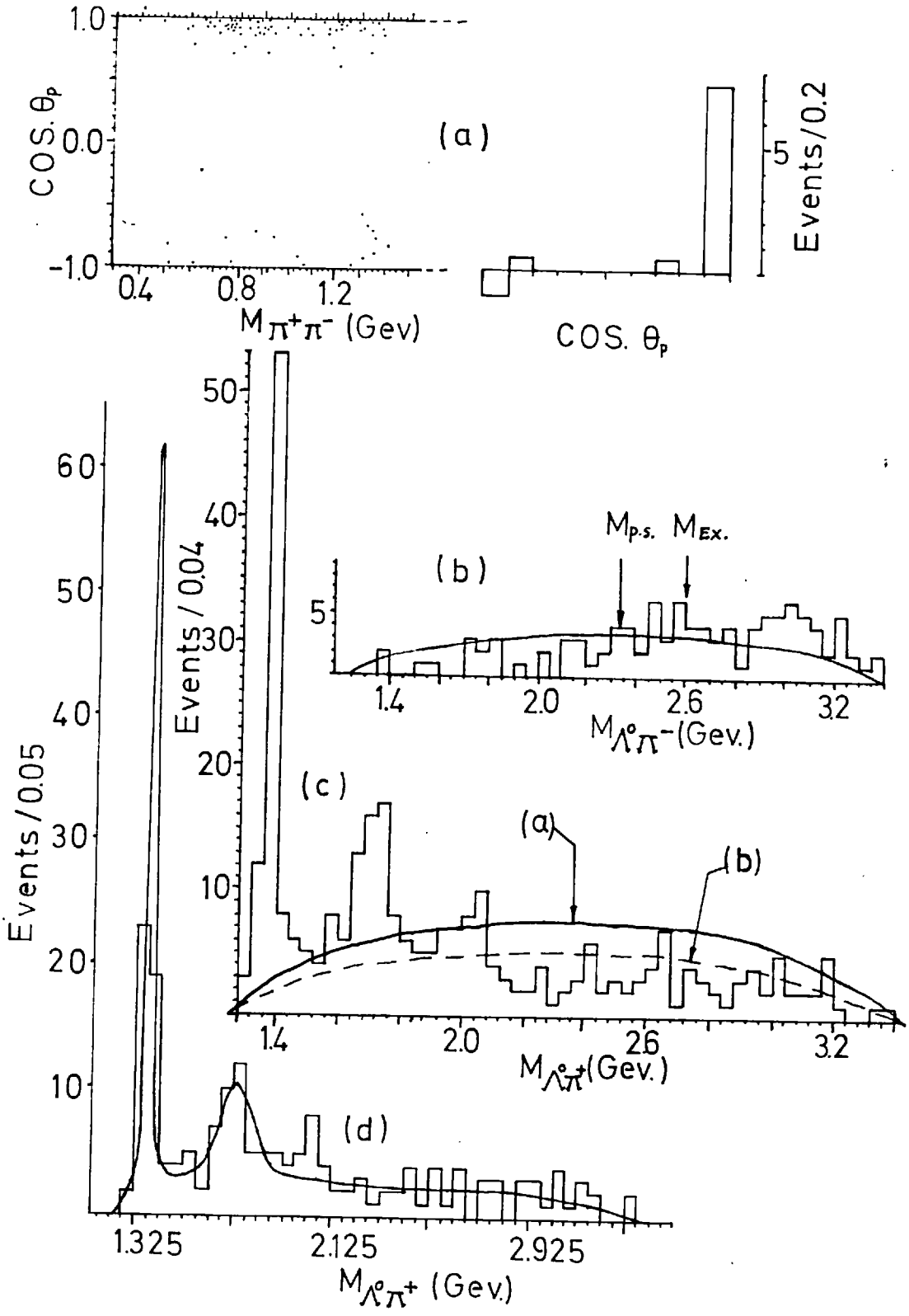

1.0
0.0
-1.0
COS. θp
0.4
0.8
1.2
Mπ+π- (Gev)
(a)
5
Events/0.2
COS. θp
50
40
30
20
10
Events / 0.04
60
50
40
30
20
10
Events/0.05
(b)
Mp.s. MEx.
5
1.4
2.0
2.6
3.2
MΛ°π- (Gev.)
(c)
(a)
(b)
1.4
2.0
2.6
3.2
MΛ°π+ (Gev.)
(d)
1.325
2.125
2.925
MΛ°π+ (Gev.)

TABLE 4.1

$Y_1^{*+}(1385)$			$Y^{*+}(1720)$		
Mass(Mev.)	Width(Mev.)	%	Mass(Mev.)	Width(Mev.)	%
1372 ± 5	22 ± 5	25 ± 5	1727 ± 15	181 ± 50	24 ± 10

The errors calculated were unreliable and those given above are approximate estimates. The fit was made with three assumptions :

(a) There were only two Breit Wigner resonances present,

(b) The non-resonant events followed a phase space distribution

and (c) There were no reflections from other resonances. These assumptions were not stictly valid because in (a) the $Y_1^{*+}(1385)$ is a $p_{3/2}$ resonance and hence a p-wave angular momentum barrier should be included for the decay width. In (b) there was strong evidence for a non-phase space distribution for the non-resonant events and in (c) there was a small reflection from the $\Lambda^\circ\rho^\circ$ channel. With the small statistics of this final state the effects of the invalidity of assumptions (b) and (c) are within statistical errors. A calculation of the effect on the mass value of the $Y_1^{*+}(1385)$ by the energy dependence of the width due to the p-wave barrier gave a shift of -3 Mev. The formula used was that given by Jackson.(4.3) Viz :

$$\frac{(e_o - e_{peak})}{\Gamma_o} = \frac{2L+1}{8}\left(\frac{\Gamma_o}{e_o}\right) \frac{e_o^4 - (m_1^2 - m_2^2)^2}{e_o^4 - 2(m_1^2 + m_2^2)e_o^2 + (m_1^2 - m_2^2)^2}$$

This expression assumes $\Gamma(e) = \Gamma_o (q/q_o)^{2L+1}$

where e_o and Γ_o are the central mass and width of the resonance. The values used were 1.38 Gev. and 0.04 Gev. L is the relative angular momentum of the two body decay and m_1 and m_2 are the masses of the decay products.

i.e. $m_1 = m_{\Lambda^o} = 1.115$ Gev.

and $m_2 = m_{\pi^+} = 0.140$ Gev.

q and q_o are the three momenta of the decay particles for a non-central mass and central mass respectively. Even with this correction the central mass value was low but due to the errors involved this was not significant.

The second enhancement can be seen from Fig. 4.2(a) to be as peripheral as the $Y_1^{*+}(1385)$ with $-t_{p,Y_1^{*+}} \leq 0.9$ Gev.^{2} It cannot be explained by assuming it to be the $Y_1^{*+}(1660)$ or $Y_1^{*+}(1765)$ because the branching ratios of these resonances into $K^o p$ would give, for an estimated number of 15 events observed in the $\Lambda^o\pi^+$ decay mode :

30 events in the $K^o p$ mode if it was $Y_1^{*+}(1660)$

and 120 events in the $K^o p$ mode if it was $Y_1^{*+}(1765)$. There was no excess of events above phase space in the $K^o p$ effective mass distribution. It was also not due to contamination by $\Sigma^o\pi^+\pi^-$ events because no enhancement was seen in the $\Sigma^o\pi^+$ distribution for unambiguous $\Sigma^o\pi^+\pi^-$ events. This enhancement will be referred to as $Y^{*+}(1720)$. Due to the small value of the

signal to noise ratio and the smallness of statistics no further work was done on this enhancement. A similar enhancement was seen by the Argonne National Laboratory in a 5.5 Gev. K^-p experiment.(4.4) The combined $\Lambda^\circ\pi^+$ effective mass distribution is shown in Fig. 4.4(c). The curves superimposed are the phase space normalised to the total number of events (curve a) and phase space nomalised to the number of events with the $Y_1^{*+}(1385)$ and $Y^{*+}(1720)$ removed (curve b). There was a third enhancement seen in the $\Lambda^\circ\pi^+$ distribution at 2.06 Gev. and could be identified with the recent $Y_1^{*+}(2065)$.(4.5) These events however appeared to be almost completely associated with the ρ° and would correspond to a strongly asymmetric decay angular distribution if it was a resonance. Hence it is more oonsistent with a kinematic effect which could be due to the $\sin^2(\theta_s)_{\rho^\circ}$ distribution of the decay pions from the ρ° . The $\Lambda^\circ\pi^+$ distribution shows a general depopulation of events in the region 2.08 to 3.0 Gev. when compared with phase space.

The $\pi^+\pi^-$ distribution shows a weak ρ° peak and a second enhancement which appeared to be strongly associated with the $Y_1^{*+}(1385)$. This effect was very small and statistically unreliable. The $\Lambda^\circ\pi^-$ distribution which shows only three events in the $Y_1^{*-}(1385)$, after subtraction of the Y_1^{*+} and ρ° events is seen to be very different from phase space. This distribution is shown in Fig. 4.4(b). A method of parametrising this

deviation was to calculate the mean effective mass for a phase space distribution ($M_{p.s.}$) and compare it with that for the experimental distribution ($M_{ex.}$). The positions of these means are shown in Fig. 4.4(b). There was a displacement to larger masses of about 300 Mev. This was mainly due to the peripheral nature of the Λ° and π^-. In the K^-p centre of mass the Λ° was produced in the direction of the proton (backwards) and the π^- in the direction of the incident K^- (forwards).

The channels contributing to this final state are shown in Table 4.2.

TABLE 4.2

$K^-p \rightarrow \Lambda^\circ\pi^+\pi^-$ (177 events (71 ± 20 μbns.)

Channel	%	Cross section bns.
$Y_1^{*+}(1385)\ \pi^-$	25 ± 5	17 ± 4
$Y_1^{*-}(1385)\ \pi^+$	2 ± 1	1.2 ± 0.4
$\Lambda^\circ\ \rho^\circ$	13 ± 4	10 ± 3
$Y^*(1720)\ \pi^+$	8 ± 4	6 ± 2
$\Lambda^\circ\pi^+\pi^-$	52 ± 14	37 ± 8

4.4 The two body channels.

$$K^-p \longrightarrow Y_1^{*+}\pi^-$$

The $Y_1^{*+}(1385)$ was defined as $1.35 \leqslant M_{\Lambda^\circ\pi^+} \leqslant 1.43$ Gev. This channel is produced strongly and cleanly. With this criteria on the $\Lambda^\circ\pi^+$ effective masses the estimated background was $\lesssim 10\%$ and for the following analysis was ignored. The decay angular

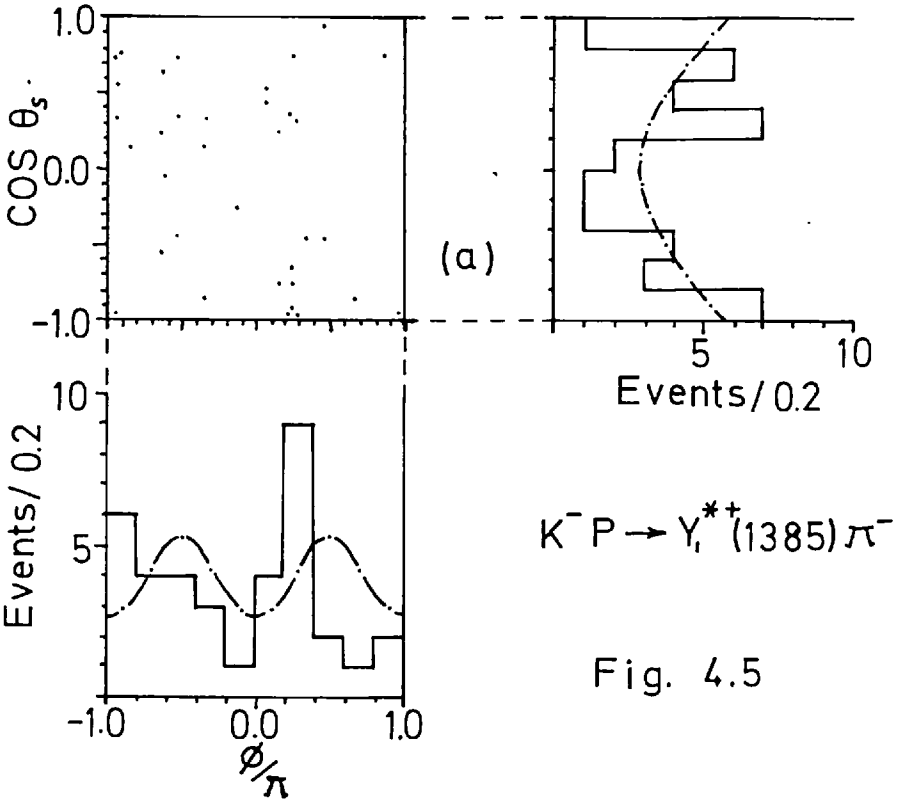
distributions ($\mathrm{Cos.}(\theta_s)_{Y_1^{*+}}$ and $\varphi_{Y_1^{*+}}$) for the Y_1^{*+} decay are shown in Fig. 4.5(a). The spin density matrix elements were calculated for these events using maximum likelihood and and moments methods. These matrix elements averaged over the momentum transfer range $0.0 \lesssim -t_{p,Y_1^{*+}} \lesssim 1.0$ Gev.^{2} are shown in Table 4.3. For a spin 3/2 particle decaying into spin 1/2 and spin 0 particles the decay distribution is given by:(4.6)

$$W(\cos.\theta_s, \varphi) = 3/4\pi\big(1/6(1 + 4\rho_{33}) + 1/2(1-4\rho_{33})\cos.^2\theta_s - 2/\sqrt{3}\,\mathrm{Re}\,\rho_{3,-1}\sin.^2\theta\cos.2\varphi - 2/\sqrt{3}\,\mathrm{Re}\,\rho_{3,1}\sin.2\theta\cos.\varphi\big)$$

and from the trace condition : $\rho_{11} = 1/2 - \rho_{33}$

The ρ- parameters are the expectation values of the quantum mechanical states defined by the overlap integral of two magnetic substates. The subscripts denote the value of the magnetic quantum number of each substate.

For this channel the Stodolsky -Sakurai model which fixes the values of the ρ -parameters can be applied. The basis of this model is to consider a peripheral production process and make the exchanged K^{*o} equivalent to a photon assuming that the strong Ml. coupling observed in the reaction $\gamma p \rightarrow N_{33}^{*++}$ also predominates at the baryon vertex, i.e. $K^{*o}p \rightarrow Y_1^{*+}$. A peripheral production mechanism is certainly valid for this channel which from Fig. 4.3(a) is seen to be very peripheral. The values of the ρ -parameters calculated for this model are shown in Table 4.3.



$K^- P \rightarrow Y_1^{*+}(1385)\pi^-$

Fig. 4.5

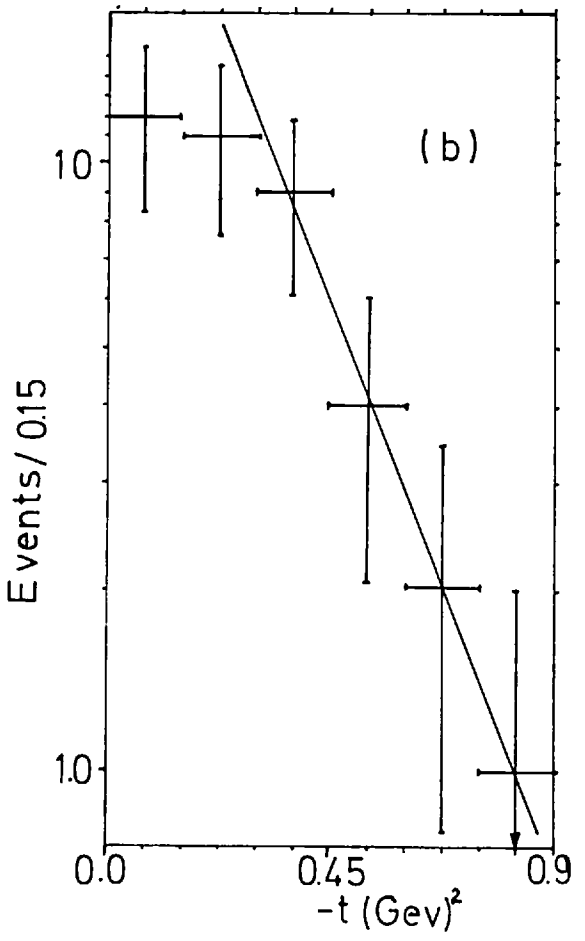


TABLE 4.3

$Y_1^{*+}(1385)$ decay matrix elements

Method	ρ_{33}	Re $\rho_{3,-1}$	Re $\rho_{3,1}$
Max. Lik.	0.23 ± 0.08	0.12 ± 0.08	0.12 ± 0.08
Moments.	0.24 ± 0.03	0.11 ± 0.08	0.09 ± 0.07
Stodolsky Sakurai	0.375	0.216	0.00

The experimental values of ρ_{33} and Re $\rho_{3,-1}$ are both less than the Stodolsky Sakurai values. This difference could be explained either by a decrease in the effective strength of the M1 coupling due to absorption[4.8] effects or the exchange of a higher spin system, e.g. $K^{*o}(1400)$.

The momentum transfer distribution for the Y_1^{*+} is shown in Fig, 4.5(b). It is plotted logarithmically and an approximate fit was made to the expression $d\sigma/dt = A\, e^{-at}$.

The values found were $a = 2.5 \,^{+9}_{-1.5}$ Gev.$^{-2}$

and $A = 20 \,^{+12}_{-6}$ μbns.

The cross section for this channel is given in Table 4.2.

$K^- p \longrightarrow \Lambda^\circ \rho^\circ$

This channel is very weak and for a mass selection of $0.625 \leq M_{\pi^+\pi^-} \leq 0.875$ has a background of about 50%. Due to the background and statistical uncertainties only the production angle against the $\pi^+\pi^-$ effective mass and a background subtracted histogram of the production angle are shown in Fig. 4.4(a).

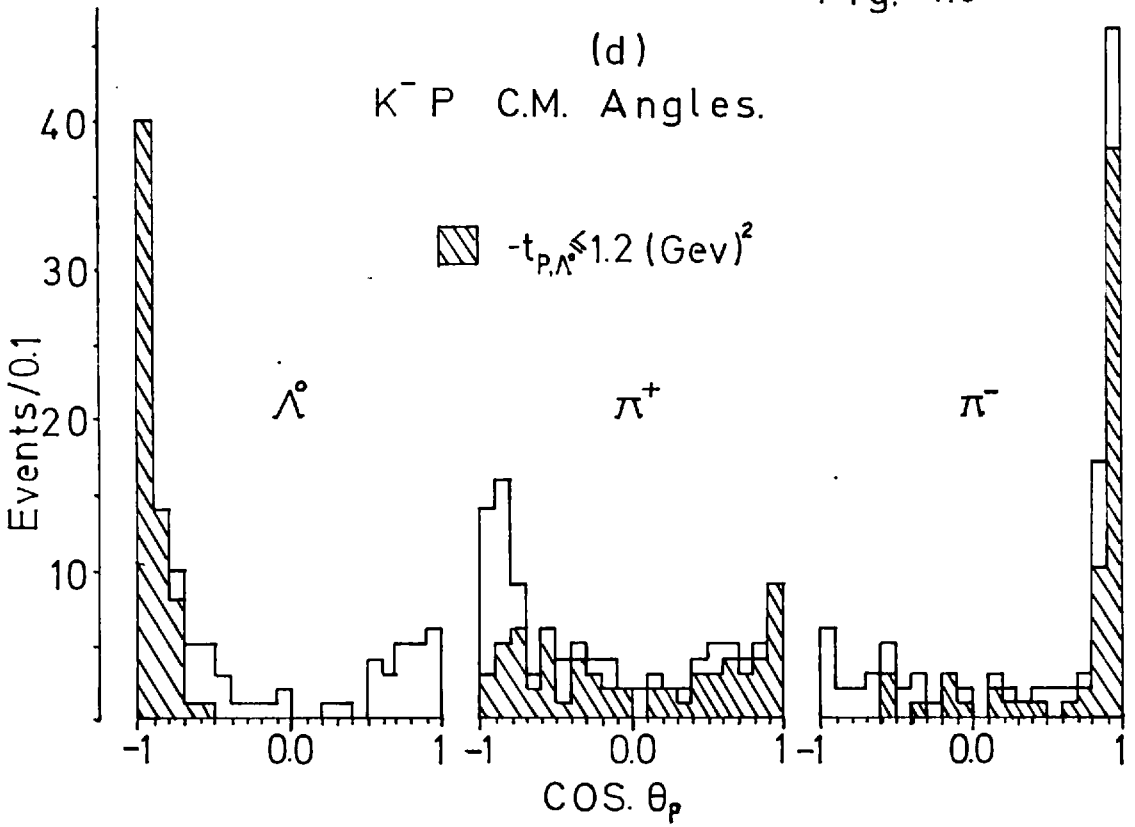
The background was the sum of two mass bands of half the width of the ρ^o band. One was above the ρ^o band and the other below. There was no evidence for a backward ρ^o peak in the differential cross section of $\Lambda^o\rho^o$. This is in contrast with experiments at lower energies.(4.9) However from the ratio of forward to backward ρ^o production at 5.5 Gev.(4.2) and assuming this to be the same at 6.0 Gev. then the number of backward ρ^o's at 6.0 Gev. would be about 3 events. The cross section for the $\Lambda^o\rho^o$ channel is shown in Table 4.2. The decay distributions (Cos.(θ_s) and Φ) for the ρ^o suggest that there is a strong vector exchange mechanism.

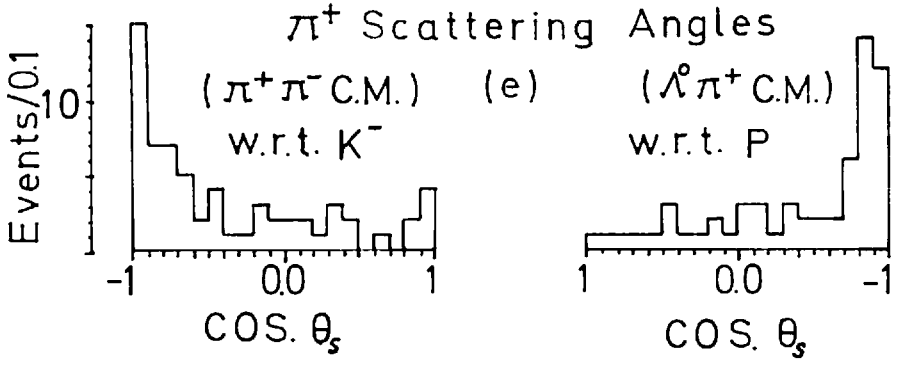
4.5 The three-body channel ($\Lambda^o\pi^+\pi^-$)

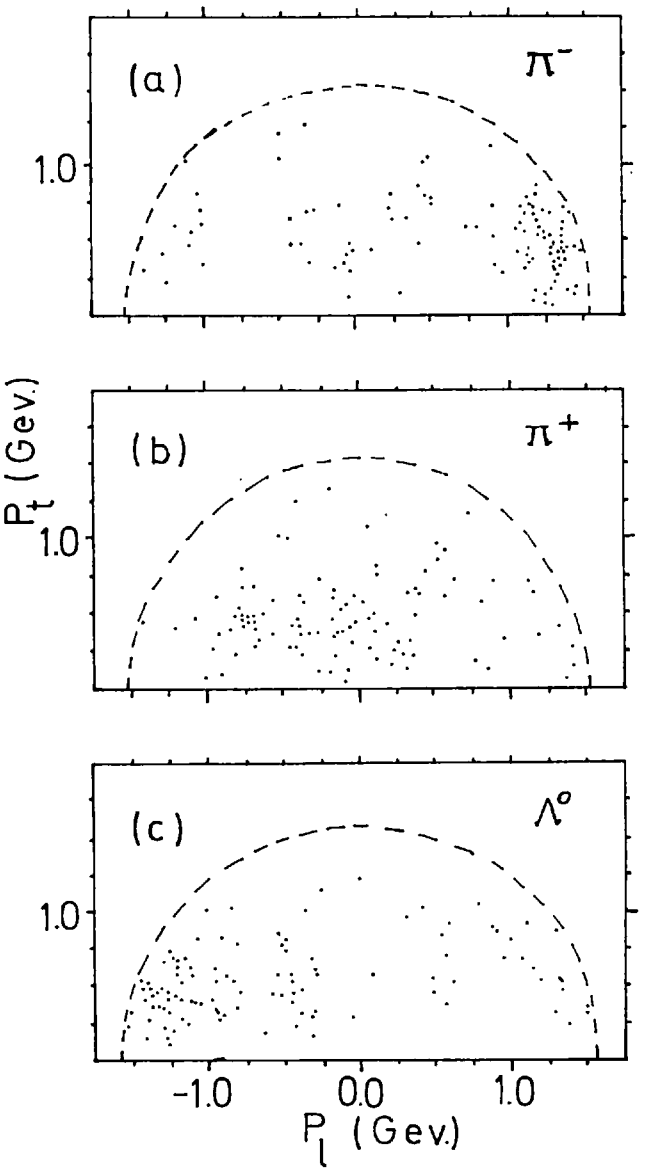
This channel was obtained by removing the $Y_1^{*+}(1385)$ and ρ^o events in the ranges defined previously . This leaves a small contamination from events in the $Y^{*+}(1720)$. The total contamination was estimated to be about 20%, with a loss of true $\Lambda^o\pi^+\pi^-$ events of about 10%. This channel is of importance due to the increasing interest in the three body channels. See references 4.9,10,11,12. The channel was characterised by the Λ^o being of high momentum (1.3 Gev.), and peaked backwards, the π^+ being of relatively low momentum (0.5 Gev.) and isotropic and the π^- being of high momentum (1.3 Gev.) and peaked forwards. These features are best displayed by a "Peyrou Plot". This is a scatter diagram of the transverse

momentum against the longitudinal momentum for a given particle in the overall centre of mass. This is shown in Fig. 4.6(a), 4.6(b) and 4.6(c) for the π^-, π^+ and Λ° respectively. There was a small cluster of events on the Peyrou plot of the π^+ at $P_l \sim 0.5$ Gev. and $P_t \sim 0.75$ Gev. and on ~~the~~ that of the Λ° at $P_l \sim 0,5$ Gev. and $P_t \sim 0.5$ Gev. These events correspond to the $Y_1^{*+}(1720)$. The production angular distribution in the K^-p centre of mass for each particle is shown in Fig.4.6(d). The enhancement in the π^+ distribution at $\text{Cos.}(\theta_p)_{\pi^+} \sim -1.0$ also corresponds to the $Y^{*+}(1720)$ events. The general features of these distributions suggest that a double peripheral production mechanism is occurring for most of the events. To investigate this further a selection of peripheral Λ°'s was made by requiring the criterion $-t_{p\Lambda^\circ} \leq 1.2$ Gev.^{2} to be satisfied. This condition removes only 35% of the $\Lambda^\circ\pi^+\pi^-$ events and in these about 50% belong to the $Y^{*+}(1720)$. The production angular distributions for these peripheral Λ° events for each particle are shown as shaded histograms in Fig. 4.6(d). For these events the π^- is seen to become more peaked in the opposite direction to the Λ° and the π^+ is isotropic. Further evidence for the double peripherality were the strongly peaked distributions of the scattering angle of the π^+ in the $\pi^+\pi^-$ centre of mass with respect to the incident K^- and the scattering angle of the π^+ in the $\Lambda^\circ\pi^+$ centre of mass with respect to

Fig. 4.6


(d)
K⁻ P C.M. Angles.
-t_{P,Λ°} ≤ 1.2 (Gev)²
Λ°
π⁺
π⁻
Events/0.1
40
30
20
10
-1
0.0
1
COS. θ_P


π⁺ Scattering Angles
(e)
(π⁺π⁻ C.M.)
w.r.t. K⁻
(Λ°π⁺ C.M.)
w.r.t. P
Events/0.1
10
-1
0.0
1
COS. θ_s


(a)
π⁻
(b)
π⁺
(c)
Λ°
P_t (Gev.)
1.0
-1.0
0.0
1.0
P_l (Gev.)

the direction of the proton. These distributions are shown in Fig.4.6(e). The similarity of these distributions is a reflection of the isotropy of the π^+ production angle.

The scatter plot of the momentum transfer to the $\Lambda^\circ\pi^+$ system against the $\Lambda^\circ\pi^+$ effective mass (Fig.4.3(a) shows a definite transition at $M_{\Lambda^\circ\pi^+} \sim 2.2$ Gev. from small momentum transfer to a uniform distribution of momentum transfer. This transition region corresponds to the depopulation in the $\Lambda^\circ\pi^+$ effective mass distribution mentioned earlier. The channel was further purified by removing the $Y^{*+}(1720)$ events using a mass range $1.65 \lesssim M_{\Lambda^\circ\pi^+} \lesssim 1.775$ Gev. and a momentum transfer range $-t_{p,Y^{*+}} \lesssim 0.5$ Gev.^{2} to define the $Y^{*+}(1720)$. The remaining $\Lambda^\circ\pi^+\pi^-$ events were used in the analysis discussed in chapter 6.

CHAPTER 5

5.1 In this chapter the final state $\Lambda^\circ\pi^+\pi^-\pi^\circ$ will be discussed. This final state, at this energy, was difficult to isolate with a small contamination because the error on the missing mass was of the same magnitude as the mass of the missing neutral pion. See Figure 3.5(c). This means that the fitting program was not efficient in rejecting those events with two neutral pions in which the effective mass of the two neutral pions was at the threshold of the two pion phase space. This contamination was reduced to about 5% by the missing mass cut offs given in Chapter 3.

The type of hypothesis used was based on the a priori knowledge that events with one strange particle (Λ° or K°) had a much larger cross section than those with three strange particles. The hypotheses tested were given in Chapter 2. Because only these were used spurious peaks in the effective mass distributions of the $\Lambda^\circ\pi^+\pi^-\pi^\circ$ final state may occur. These will be due to contamination from three strange particle events which are kinematically similar to the $\Lambda^\circ\pi^+\pi^-\pi^\circ$ events. The events most likely to cause these peaks are :

$$K^-p \longrightarrow \Sigma^\circ K^+K^- \ , \ \Sigma^\circ K^+K^- \ \pi^\circ \text{ and } \Lambda^\circ K^+K^- \pi^\circ .$$

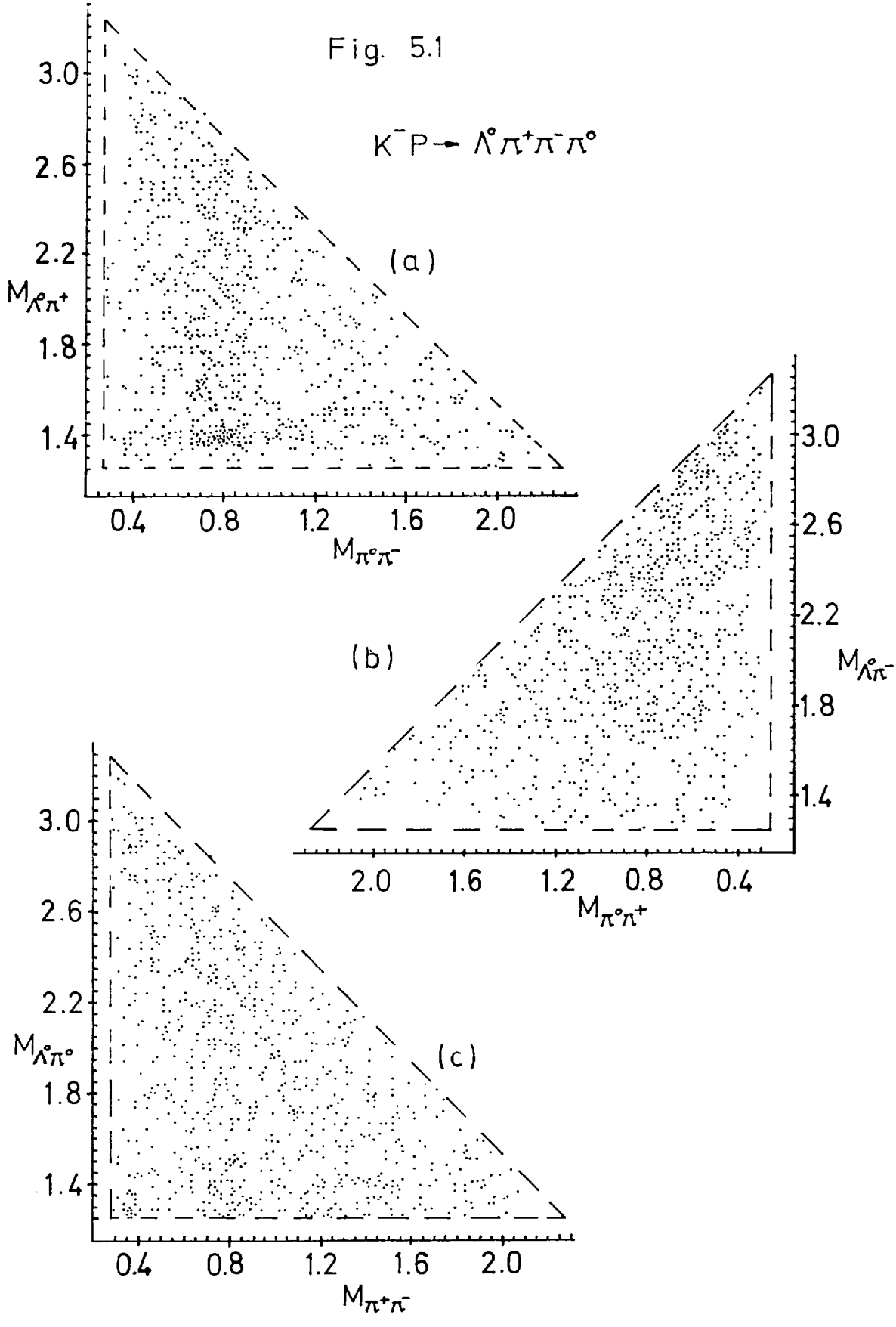
These events will contain the φ° meson decaying into K^+ and K^-. For the φ° decay, when the kaons are interpreted as pions, the $\pi^+\pi^-$ effective mass is about 0.35 Gev. and the width is

small (about 20 Mev.). The effective mass distributions most sensitive to these contaminations are the $\pi^+\pi^-$ from the φ° events and the $\Lambda^\circ\pi^\circ$ from the $\Sigma^\circ K^+K^-$ and also the unfitted $\Sigma^\circ\pi^+\pi^-$ and $\Lambda^\circ\pi^+\pi^-$ events, which will produce a $\Lambda^\circ\pi^\circ$ threshold enhancement.

A study of these two mass distributions showed that both effects were present. In the $\pi^+\pi^-$ distribution there was a 50 Mev. wide enhancement at 0.35 to 0.40 Gev. and in the $\Lambda^\circ\pi^\circ$ distribution there was a strong threshold enhancement. A strong overlap was found to exist between both these enhancements. This can be seen from the triangle plot of $M_{\pi^+\pi^-}$ vs. $M_{\Lambda^\circ\pi^\circ}$, shown in Fig. 5.1(c). This overlap indicates contamination from the $\Sigma^\circ K^+K^-$ events. To reduce the contamination from these three strange particle and unfitted 4.C. events the events with $1.255 \leq M_{\Lambda^\circ\pi^\circ} \leq 1.315$ Gev. and $-t_{p,\,\Lambda^\circ\pi^\circ} \leq 1.2$ Gev.^{2} were removed. The events in this region will be referred to as "Σ°" events. The sample obtained after the removal of these "Σ°" events and used for the analysis of this final state was 766 events, giving a cross section of 314 ± 40 μbns.

As a preliminary analysis an estimate of the parameters (mass, width and percentage) of the main resonances produced in this final state i.e. $Y_1^{*+}(1385)$, ρ^- and ρ° was obtained by fitting the appropriate effective masses to a Breit Wigner resonance plus phase space distribution. The fit was made with the assumption that there is only one resonance present and no reflections from

Fig. 5.1


$K^-P \to \Lambda^\circ\pi^+\pi^-\pi^\circ$
(a)
$M_{\Lambda^\circ\pi^+}$
3.0
2.6
2.2
1.8
1.4
0.4
0.8
1.2
1.6
2.0
$M_{\pi^\circ\pi^-}$
(b)
$M_{\Lambda^\circ\pi^-}$
$M_{\pi^\circ\pi^+}$
(c)
$M_{\Lambda^\circ\pi^\circ}$
$M_{\pi^+\pi^-}$

other resonances. The fitting was done with a maximum likelihood method. To ensure reasonable agreement with the assumptions, all the other resonances which could cause reflections in the distribution to be fitted were removed. The criteria defining these resonances are given later in the chapter. The fitted curves are shown in Fig.5.5. and the fitted values of the parameters are given in Table 5.1.

TABLE 5.1

Resonance	$Y_1^{*+}(1385)$	ρ^-	ρ°
Mass	1379 ± 3	766 ± 15	753 ± 20
Width	44 ± 10	185 ± 30	150 ± 30
Percentage	14 ± 2	28 ± 3	12 ± 2

The quality of the fit is quite good and hence the assumptions made are reasonably valid.

The method of analysis was to define each resonance by a mass range only, when the resonance was produced with little background (e.g. ω° and η°), and by a mass range and momentum transfer range when the background is large (e.g. ρ^- and ρ°). The second method of resonance definition made use of the general peripheral production of resonances at this energy. An important part of the analysis when studying a particular channel was to remove the events in the unwanted resonances using the method of resonance definition given above. This method of

resonance removal reduces the biasing and loss effects of removing events on the basis of a mass range only. The effective mass distributions of every possible particle combination are shown in Figs. 5.2,3,4 and 5.6(d). The broken outline corresponds to the distribution produced when the events are weighted with the maximum and minimum Λ° decay length cut offs discussed in Chapter 3. In the $\pi^+\pi^-\pi^\circ$ distribution these events are shown shaded. From these distributions there is obvious ρ^-, ρ°, ω°, and $Y_1^{*+}(1385)$ production. The amount of $Y_1^{*c}(1385)$ production was difficult to estimate because of the somewhat artificial removal of the $\Lambda^\circ\pi^\circ$ threshold enhancement and the possible effects of $\Sigma^\circ\pi^+\pi^-\pi^\circ$ contamination. This contamination could produce enhancements at $M_{\Lambda^\circ\pi^\circ} \sim 1.405$ Gev. and 1.520 Gev. due to $Y_o^{*\circ}(1405)$ and $Y_o^{*\circ}(1520)$ production. The masses of these resonances will be reduced because the π° and $\gamma\gamma$ are constrained to have the π° mass. The presence of the $Y_o^{*\circ}(1405)$ maybe the reason for the broadness of the $Y_1^{*\circ}(1385)$ peak. The amount of associated resonance production (e.g $Y_1^*\rho$) can be seen from the triangle plots shown in Fig.5.1(c). The $\Lambda^\circ\ \pi^\circ$ threshold enhancement due to the "Σ°" events has not been removed from these plots.

A subsequent analysis of the $\pi^+\pi^-\pi^\circ$ effective mass distribution revealed that the small enhancement of 22 ± 7 events at $M_{\pi^+\pi^-\pi^\circ}$ in the range 0.95 to 1.075 Gev. was almost completely associated (70%) with the peripheral ρ° events.[5.1] From the observed

Fig. 5.2

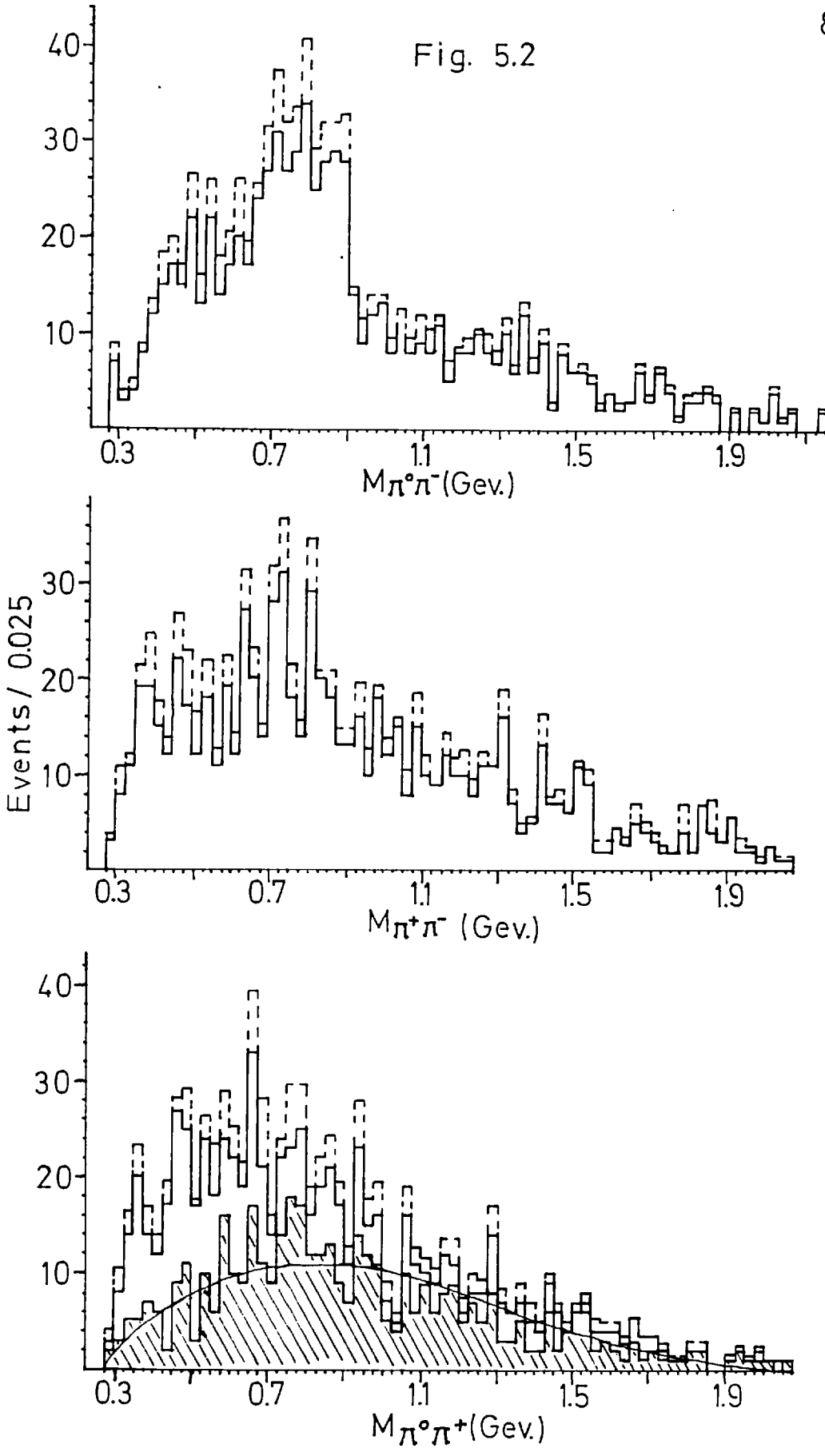

40
30
20
10
0.3
0.7
1.1
1.5
1.9
Mπ°π⁻(Gev.)
Events / 0.025
30
20
10
0.3
0.7
1.1
1.5
1.9
Mπ⁺π⁻ (Gev.)
40
30
20
10
0.3
0.7
1.1
1.5
1.9
Mπ°π⁺(Gev.)

Fig. 5.3

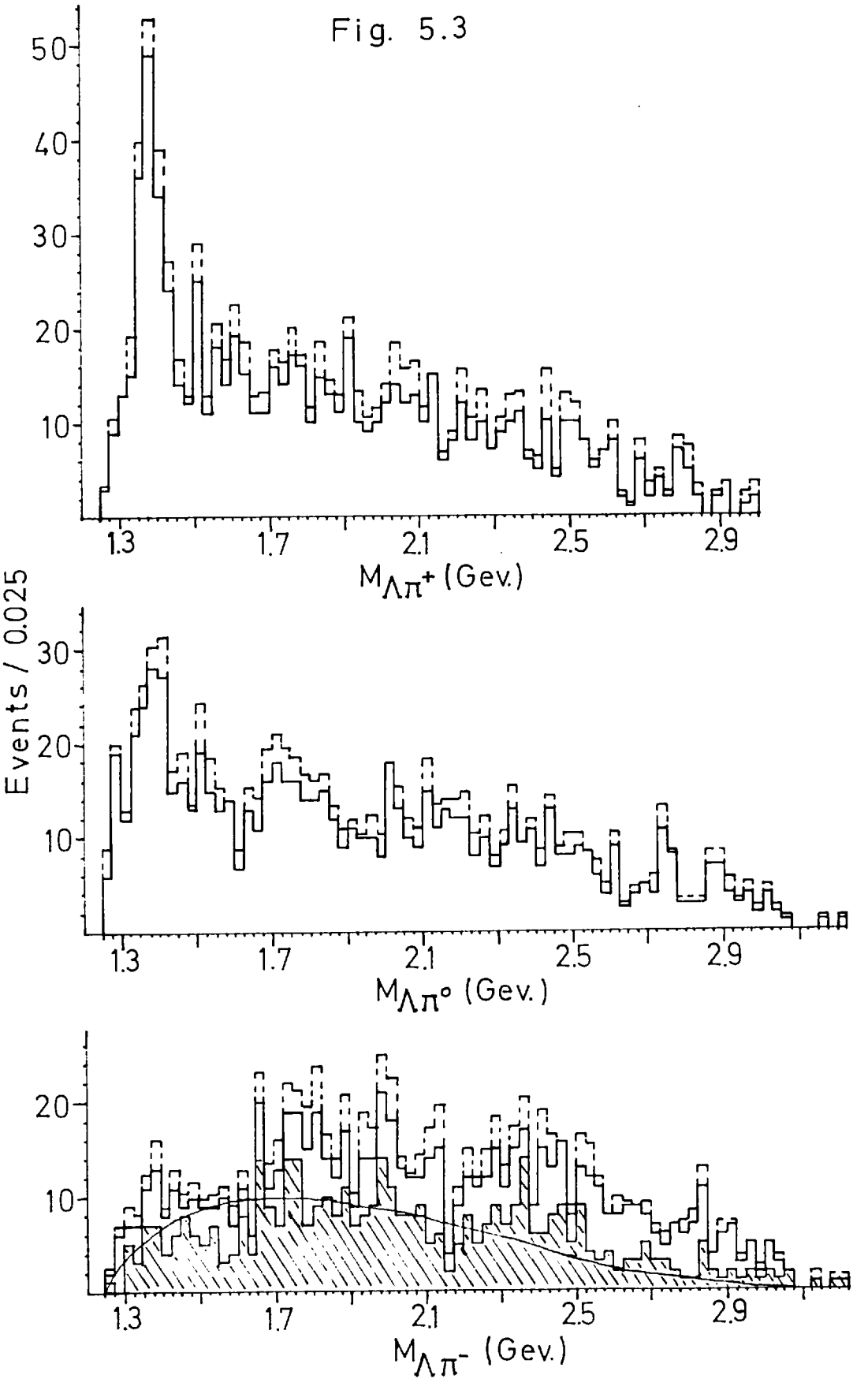
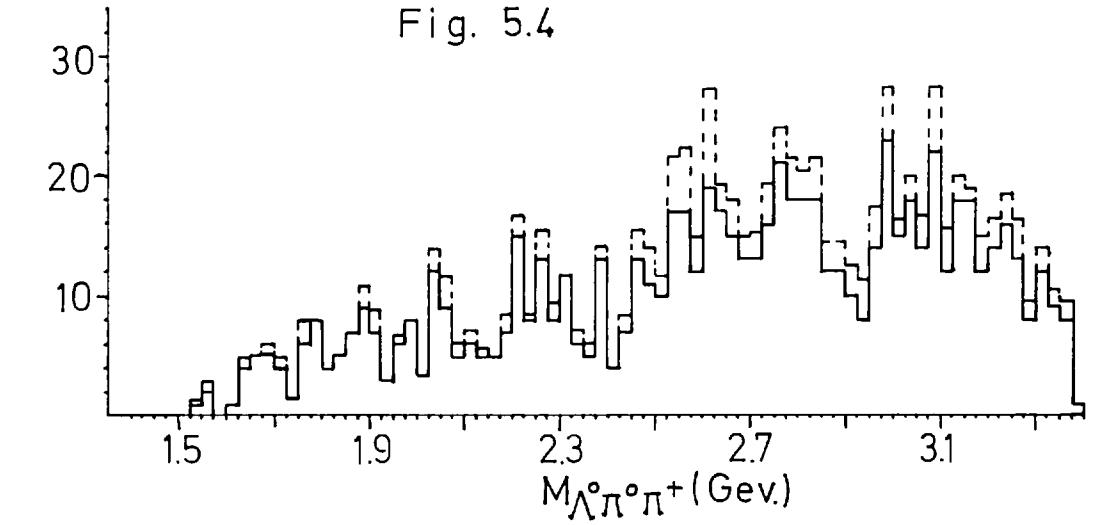
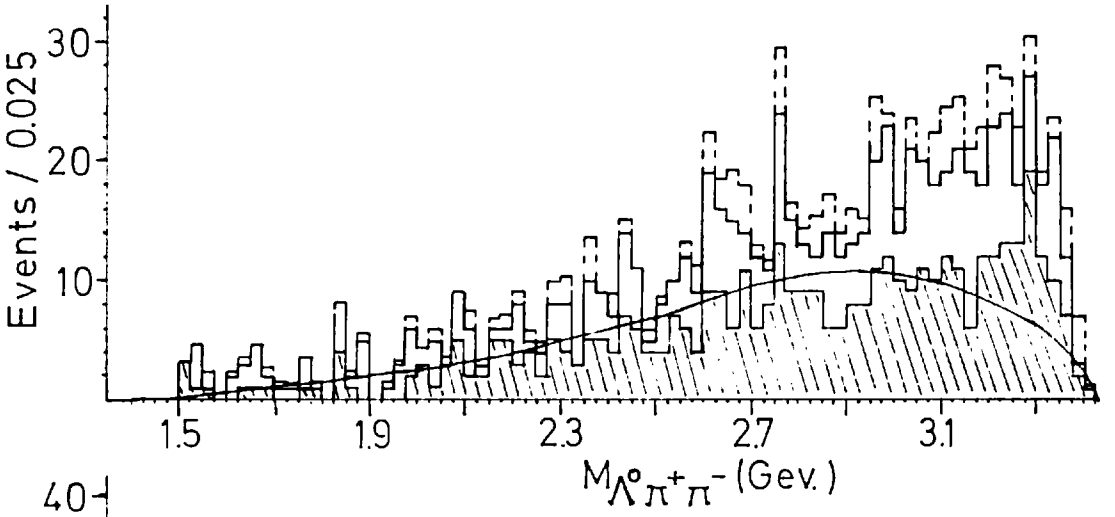

50
40
30
20
10
1.3
1.7
2.1
2.5
2.9
$M_{\Lambda\pi^+}$ (Gev.)
Events / 0.025
30
20
10
1.3
1.7
2.1
2.5
2.9
$M_{\Lambda\pi^o}$ (Gev.)
20
10
1.3
1.7
2.1
2.5
2.9
$M_{\Lambda\pi^-}$ (Gev.)

Fig. 5.4


30
20
10
1.5
1.9
2.3
2.7
3.1
$M_{\Lambda^\circ\pi^\circ\pi^+}$ (Gev.)


Events / 0.025
30
20
10
1.5
1.9
2.3
2.7
3.1
$M_{\Lambda^\circ\pi^+\pi^-}$ (Gev.)

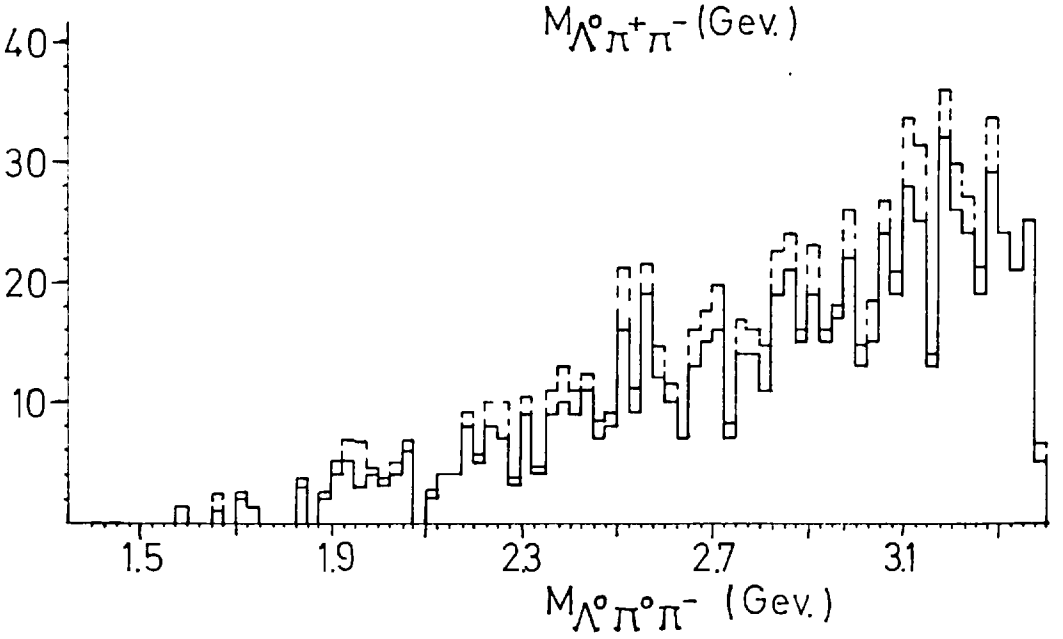
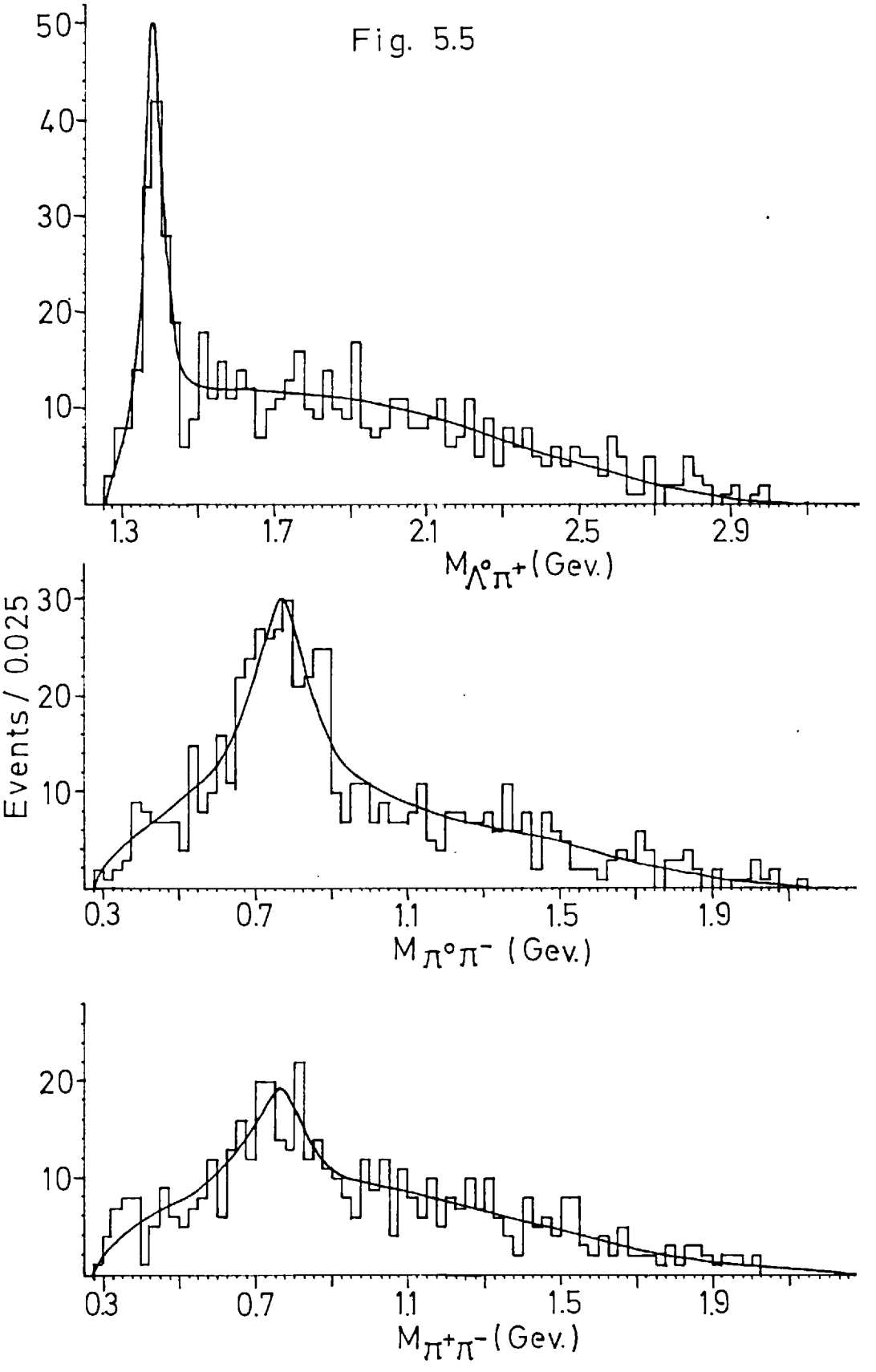

40
30
20
10
1.5
1.9
2.3
2.7
3.1
$M_{\Lambda^\circ\pi^\circ\pi^-}$ (Gev.)

Fig. 5.5


50
40
30
20
10
1.3
1.7
2.1
2.5
2.9
$M_{\Lambda^0\pi^+}$ (Gev.)
Events / 0.025
30
20
10
0.3
0.7
1.1
1.5
1.9
$M_{\pi^0\pi^-}$ (Gev.)
20
10
0.3
0.7
1.1
1.5
1.9
$M_{\pi^+\pi^-}$ (Gev.)

amount of φ^{o} meson production the number of events expected to go into $(\rho\pi)^{o}$ was 6 ± 3, assuming a branching ratio of 12%[5.2] for $\varphi \rightarrow \rho\pi$. Because this enhancement has only a $\rho^{o}\pi^{o}$ decay mode, then it must be due to a resonance of isotopic spin 0, or 2 assuming the decay is strong (isotopic spin conserving). The most likely candidate is the $\eta 2\pi$ resonance X^{o} at 960 Mev. The X^{o} according to the Rosenfeld Tables[3.1] decays into $\pi^{+}\pi^{-}\gamma$ and $\rho^{o}\gamma$. Hence this enhancement is consistent with a $\rho^{o}\gamma$ decay mode of the X^{o}. The experimental resolution is not sufficient to resolve the γ from the π^{o} . The slight increase in mass is due to constraining the γ to be a π^{o} and so obtain a $\Lambda^{o}\pi^{+}\pi^{-}\pi^{o}$ fit. There maybe some enhancement from the H meson [5.3] but the evidence for the existence of this meson is weak at present[5.4]. A similar enhancement was observed in the 2.24 $K^{-}p$ Brookhaven experiment [5.5] and in the 2.1 to 2.7 $K^{-}p$ Berkeley experiment[5.1]. This enhancement was removed by removing events for which

$$0.975 \leqslant M_{\pi^{+}\pi^{-}\pi^{o}} \leqslant 1.050 \text{ Gev. and } -t_{K^{-}, \pi^{+}\pi^{-}\pi^{o}} \leqslant 0.4 \text{ Gev.}^{2}$$

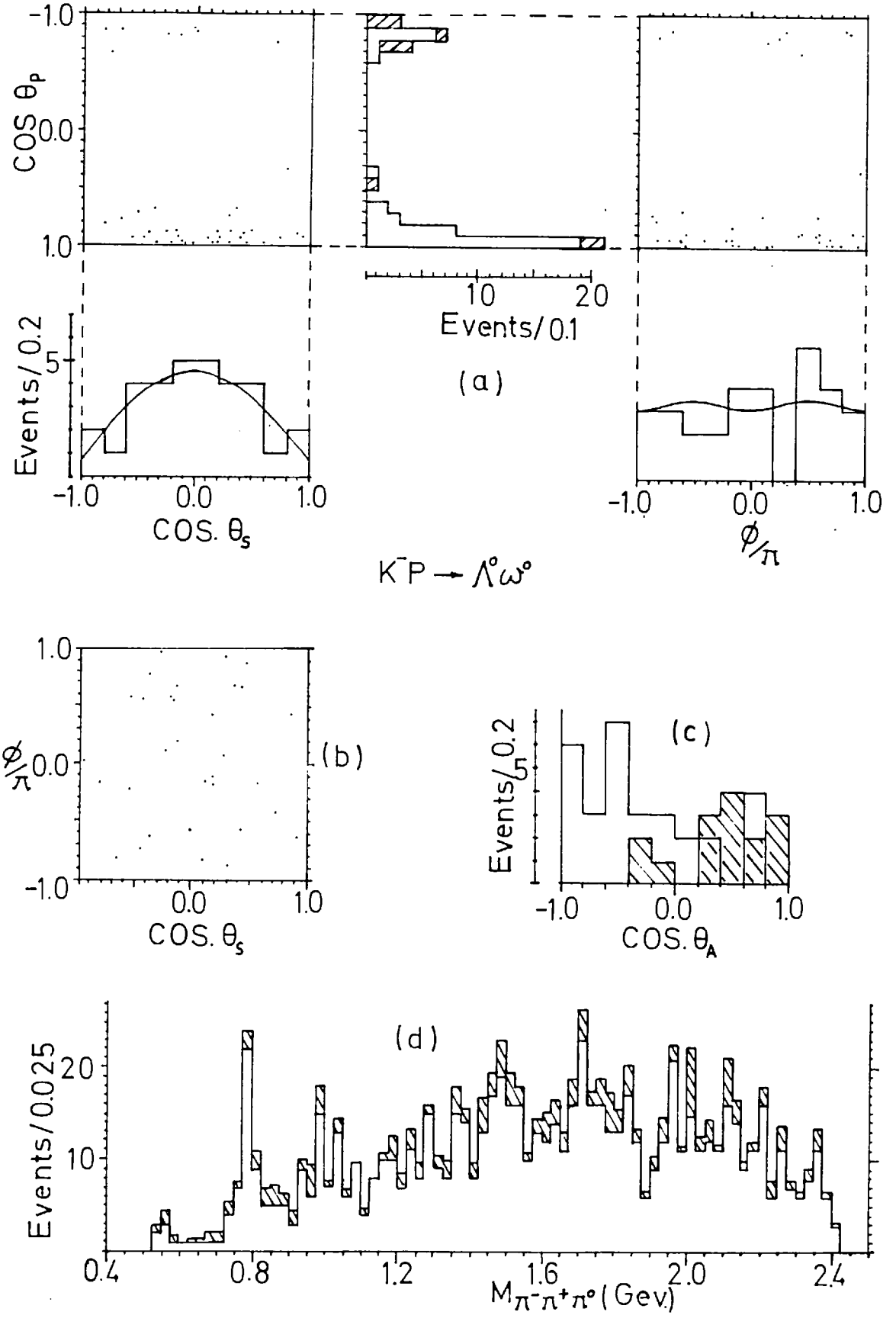
5.2 The two-body channels.

The two body channels were relatively easy to separate because of their extreme peripherality. The total cross sections for each of the two-body channels produced in the $\Lambda^{o}\pi^{+}\pi^{-}\pi^{o}$ final state are shown in Table 5.1. A detailed analysis was only possible for the $\Lambda^{o}\omega^{o}$ and $Y_{1}^{*+}(1385)\rho^{-}$ because the statistics of the other channels were very low (about 10 events).

$K^- p \longrightarrow \Lambda^\circ \omega^\circ$

This channel was separated by selecting events for which $0.750 \leq M_{\pi^+\pi^-\pi^\circ} \leq 0.835$ Gev. which gave a sample of 41 events with a contamination of $\leq 10\%$ and a loss of about 5%. The scatter plot of the production angle of the ω° against the scattering angle and azimuthal angle of the ω° decay are shown in Fig 5.6(a). The production angular distribution shows the extremely peripheral nature of the $K^- p \rightarrow \Lambda^\circ \omega^\circ$ interaction at 6 Gev. and also the presence of a well separated backward ω° peak. From a scatter plot of production angle against the $\pi^+\pi^-\pi^\circ$ effective mass (not shown) these backward events were seen not to be consistent with background. The forward to backward ratio was difficult to estimate with certainty because it was sensitive to the missing-mass cut off used. The events outside the missing-mass cuts given in Chapter 3 are shown shaded on the produotion angular distribution. With no missing-mass cut the forward backward ratio was 2.3 ± 1 and with the missing-mass cuts it was 3.6 ± 1.5. This dependence on the missing-mass is because the accuracy of the measurement of the π° mass depends on the magnitude of the π° momentum and also the accuracy of the determination of the Λ° momentum. It appears that the second effect is important for the backward ω°'s. The projections of the cosine of the scattering angle (θ_s) and the azimuthal angle (φ) for the forward ω°'s ($\cos.(\theta_p)_{\omega^\circ} > 0.6$) are shown in Fig. 5.6(a). The

Fig. 5.6


COS θp
-1.0
0.0
1.0
10
20
Events/0.1
(a)
Events/0.2
5
-1.0
0.0
1.0
COS. θs
Φ/π
K⁻P → Λ°ω°
(b)
Φ/π
(c)
Events/0.2
5
COS. θA
(d)
Events/0.025
20
10
0.4
0.8
1.2
1.6
2.0
2.4
Mπ⁻π⁺π°(Gev.)

distribution of $\cos.(\theta_s)$ indicates that if absorption effects are ignored then there is strong vector exchange(K^*) i.e. θ_s has a $\sin.^2(\theta_s)$ dependence. For the ω° decay distributions events outside the missing-mass cuts are not included. The decay distribution for a vector meson is :(4.6)

$$W(\cos.\theta_s,\varphi) = 3/4\pi\{1/2(1-\rho_{oo}) + 1/2(3\rho_{oo}-1)\cos^2\theta_s - \rho_{1,-1}\sin^2\theta_s\cos.2\varphi - \sqrt{2}\mathrm{Re}\,\rho_{1,0}\sin 2\theta_s\cos\varphi\}$$

where $\rho_{1,1} = 1/2(1-\rho_{oo})$

Integration over φ gives :

$$W(\cos.\theta_s) = 3/4\,((1-\rho_{oo}) + (3\rho_{oo}-1)\cos.\theta_s)$$

and over $\cos.\theta_s$ gives :

$$W(\varphi) = 1/2\,\pi((1+2\rho_{1,-1}) - 4\rho_{1,-1}\cos.^2\varphi)$$
$$= 1/2\,\pi(1-2\rho_{1,-1}\cos.2\varphi)$$

These are completely general expressions derived on the basis of the quantum mechanical theory of angular momentum and parity conservation. The values of the ρ-parameters were found experimentally from the values of $\cos.\theta_s$ and φ for each event by maximum likelihood and moments methods. The values obtained are shown in Table 5.2. These values are for the forward ω°'s only.

TABLE 5.2

	ρ_{oo}	$\rho_{1,-1}$	$\mathrm{Re}\,\rho_{1,0}$
Max. Lik.	0.08 ± 0.10	0.03 ± 0.13	-0.01 ± 0.08
Moments.	0.06 ± 0.10	-0.02 ± 0.13	-0.025 ± 0.06

The scatter plot of $\cos.\theta_s$ against φ is shown in Fig.5.6(b). The statistics however are too low to reveal any correlations due to absorptive effects. Assuming no absorptive effects the value of ρ_{oo} corresponds to $90 \pm 10\%$ vector exchange. The value of $\rho_{1,-1}$ which determines the strength of the $\cos.2\varphi$ variation of φ was small and may be related to the observed polarisation of the backward Λ°'s. The polarisation of the forward and backward Λ°'s was calculated from the asymmetry of the distribution of the decay angle of the Λ°. This angle is defined as the angle between the direction of the pion from the Λ° in the Λ° centre of mass and the direction of the normal to the production plane. The distributions of this angle for the backward Λ°'s and forward Λ°'s (shown shaded) are shown in Fig. 5.6(c). The results of the analysis of these distributions are shown in Table 5.3. The value of the Λ° decay asymmetry (α) was taken to be 0.66.

TABLE 5.3

	Backward Λ°'s	Forward Λ°'s
Prod. Angle Range	$\cos.(\theta_p)_{\omega^o} < -0.6$	$\cos.(\theta_p)_{\omega^o} > 0.0$
Asymmetry (αP)	-0.81 ± 0.28	0.48 ± 0.33
Polarisation(P) %	-110 ± 40	70 ± 40

It is of interest to note that there is a difference in the sign of the Λ° polarisation between the backward (meson exchange)

and the forward (baryon exchange) Λ°'s. The cross section of this channel is given in Table 5.5. This cross section is corrected for the unseen neutral decays of the ω° as well as the biases and losses discussed in Chapter 3.

$K^{-}p \longrightarrow \Lambda^{\circ}\eta^{\circ}$

This channel was seen as a small enhancement at the threshold of the $\pi^{+}\pi^{-}\pi^{\circ}$ effective mass distribution (see Fig. 5.6(d)). The number of events was 5 ± 2 and hence only the cross section for the $\pi^{+}\pi^{-}\pi^{\circ}$ decay mode was calculated. This is given in Table 5.5. The production of this channel was very peripheral with all events having $\cos.(\theta_{p})_{\eta^{\circ}} \lesssim 0.95$.

$K^{-}p \rightarrow Y_{1}^{*}(1385)\rho^{-}$

The production of the various charged modes of this channel can be seen from the appropriate triangle plots. The amount of $Y_{1}^{*-}\rho^{+}$ is consistent with zero and an upper limit to this cross section is given in Table 5.5. Assuming the dominance of $\bar{K}^{\circ}$ and $\bar{K}^{*\circ}$ (isospinor) exchange for these channels the ratio

$$\sigma_{Y_{1}^{*+}\rho^{-}} / \sigma_{Y_{1}^{*\circ}\rho^{\circ}} = 4$$

The experimental value for this ratio was 4 ± 2. This value however is uncertain due to the unknown contamination from $Y_{o}^{*\circ}(1405)$ discussed earlier. Only the channel $Y_{1}^{*+}\rho^{-}$ was sufficiently strong to warrant further detailed analysis. The $Y_{1}^{*+}\rho^{-}$ sample was selected by the following criteria :

$1.350 < M_{\Lambda^{\circ}\pi^{+}} < 1.435$ Gev. and $0.65 < M_{\pi^{-}\pi^{\circ}} < 0.90$ Gev.

These criteria gave a sample of 49 events with a background contamination of $\leq 20\%$ and a loss of true $Y_1^{*+}\rho^-$ events of about 10%. In the case of overlapping resonance bands there are four kinds of events contributing to the overlap region, which due to the width of the ρ^- is rather large.

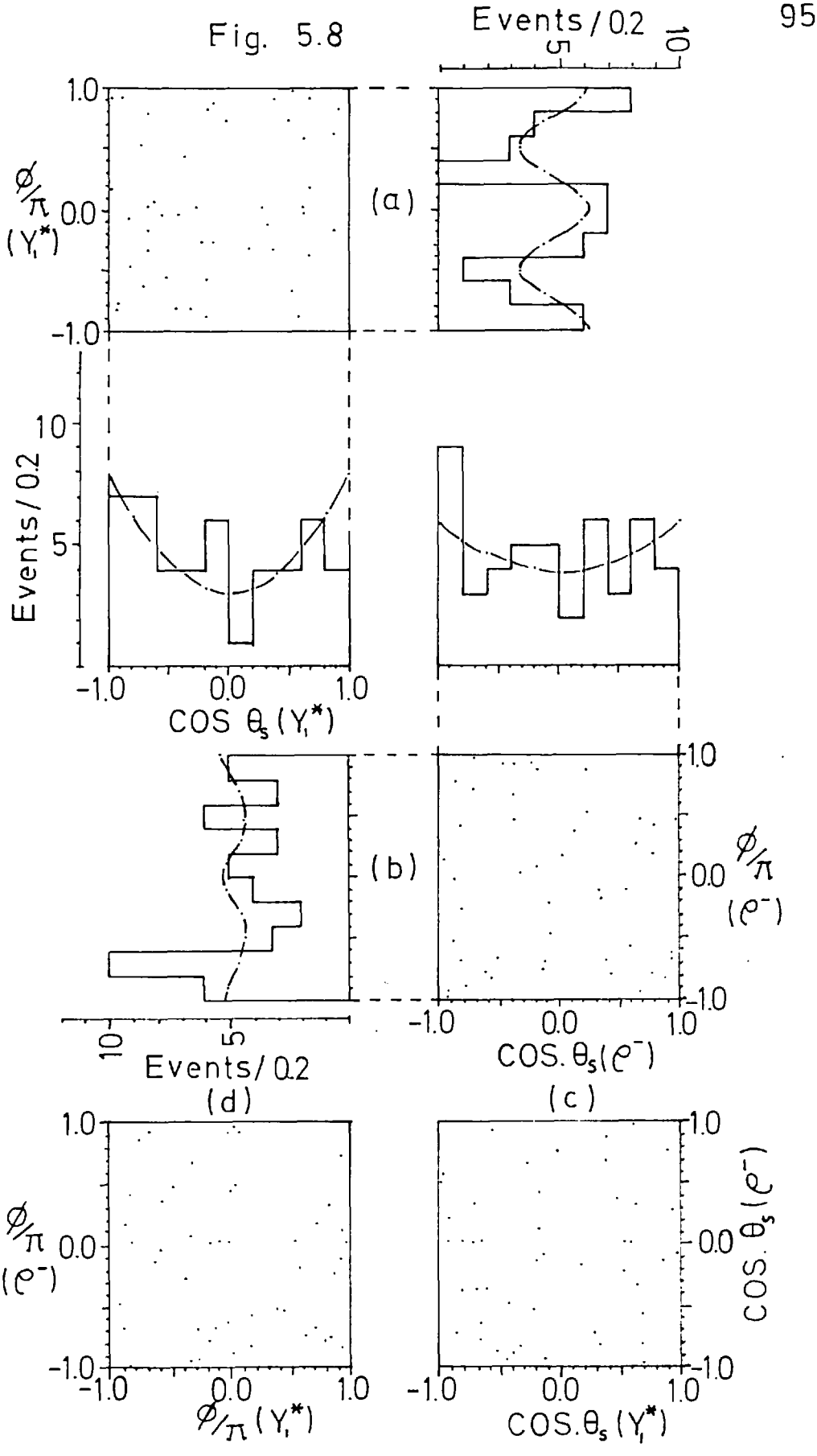
(a) The pure background events (non-resonant).

(b) The events containing a genuine ρ^- and a background $\Lambda^\circ\pi^+$ combination in the Y_1^{*+} region.

(c) The events containing a genuine Y_1^{*+} and a background $\pi^-\pi^\circ$ combination in the ρ^- region.

(d) The genuine double resonance events $Y_1^{*+}\rho^-$. The number of events in each category can be estimated from the triangle plot shown in Fig. 5.1(a). Using various sizes of the areas around the overlap region the number of $Y_1^{*+}\rho^-$ associated production events varied from 35 to 42 and an average estimate was 40 ± 10 (16 ± 4 μbn.). The production angular distribution is shown in Fig. 5.7(b). To emphasise the presence of this channel and to reduce the background to $\leq 10\%$ a momentum transfer cut was made of $-t_{p,Y_1^{*+}} \leq 0.8$ Gev.^{2} The resulting triangle plot is shown in Fig. 5.7(a). The sample used for the detailed analysis was 47 events. This channel was very interesting in that it gave an opportunity to study any correlations between the decays of the two resonances. With this in mind the following analysis was carried out. First the conventional scatter plots

Fig. 5.8


Events / 0.2
5
10
1.0
0.0
-1.0
ϕ/π (Y_1^*)
(a)
Events / 0.2
10
5
-1.0
0.0
1.0
COS θ_s (Y_1^*)
(b)
1.0
0.0
-1.0
ϕ/π (ρ^-)
-1.0
0.0
1.0
COS. θ_s (ρ^-)
10
5
Events / 0.2
(d)
(c)
1.0
0.0
-1.0
ϕ/π (ρ^-)
-1.0
0.0
1.0
ϕ/π (Y_1^*)
1.0
0.0
-1.0
COS. θ_s (ρ^-)
-1.0
0.0
1.0
COS. θ_s (Y_1^*)

of cos. θ_s and φ for the Y_1^{*+} and ρ^- were obtained. These are shown in Fig. 5.8(a) and (b). Secondly the scatter plots of cos. θ_s of the ρ^- against cos. θ_s of the Y_1^{*+}, and φ of the ρ^- against φ of the Y_1^{*+} were obtained and are shown in Fig. 5.8(c) and (d). No strong correlations are seen, however definite conclusions are impossible in view of the low statistics. There is an indication of a correlation in the scatter plot of φ_{ρ^-} against $\varphi_{Y_1^{*+}}$. This shows a depopulation along the line $\varphi_{\rho^-} = +\varphi_{Y_1^{*+}}$, but this is barely statistically significant. The results of the maximum likelihood and moments fits to the Y_1^{*+} and ρ^- decay distributions for $-t_{p,Y_1^{*+}} < 0.8$ Gev.^{2} in terms of the spin density matrix elements (ρ - parameters) are shown in Table 5.4.

TABLE 5.4.

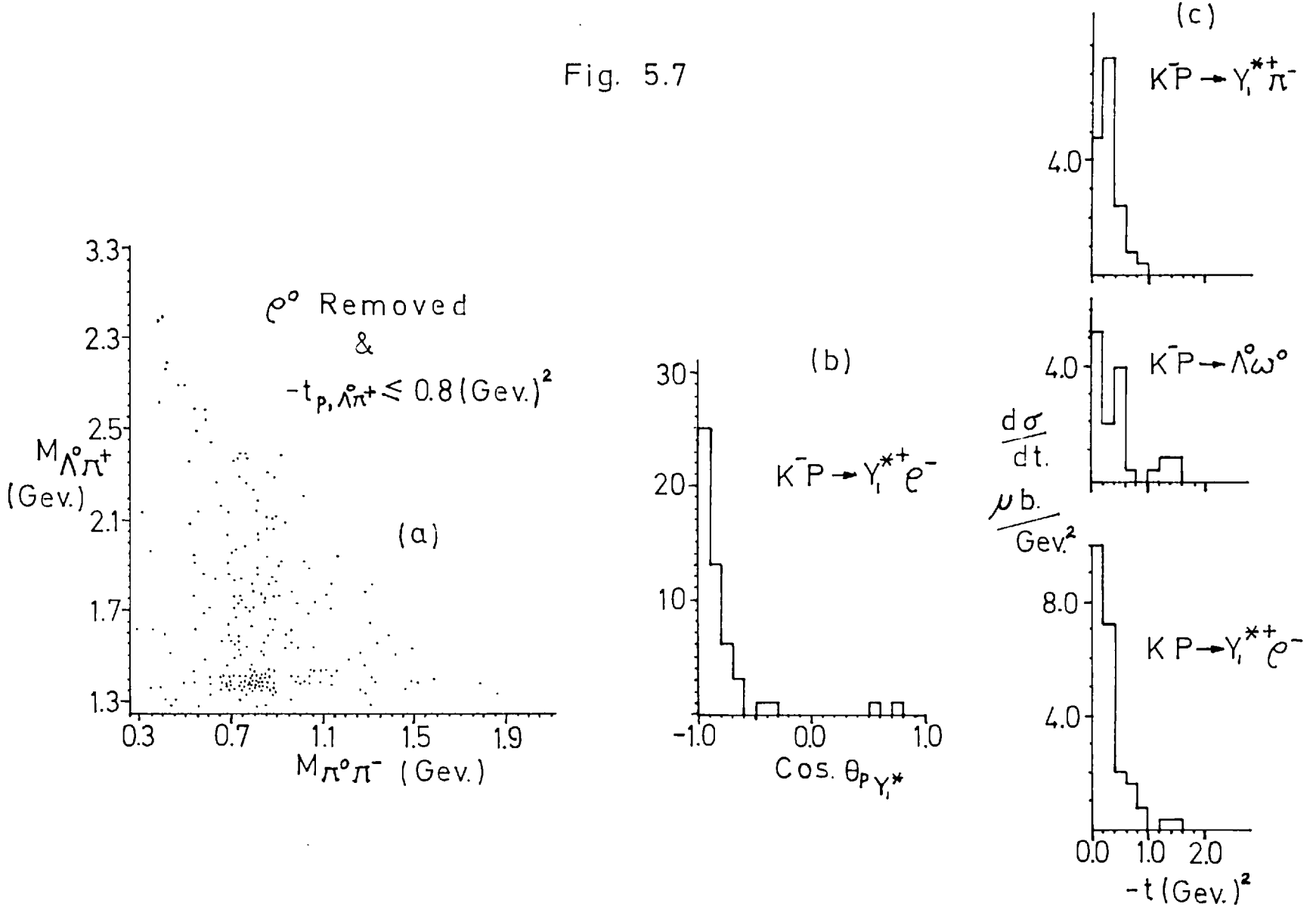
Y_1^{*+}

ρ- parameters.	$\rho_{3,3}$	Re $\rho_{3,-1}$	Re $\rho_{3,1}$
Max. Lik.	0.16 ± 0.08	-0.13 ± 0.07	-0.02 ± 0.08
Moments.	0.16 ± 0.08	-0.13 ± 0.08	-0.03 ± 0.10

ρ - parameters.	ρ_{oo}	$\rho_{1,-1}$	Re $\rho_{1,0}$
Max. Lik.	0.44 ± 0.10	-0.04 ± 0.08	0.13 ± 0.06
Moments.	0.46 ± 0.10	-0.03 ± 0.09	0.13 ± 0.06

These values, if absorption is neglected, indicate more

Fig. 5.7


(a)
ρ° Removed
&
$-t_{p,\Lambda^0\pi^+} \leq 0.8\,(\text{Gev.})^2$
$M_{\Lambda^0\pi^+}$ (Gev.)
$M_{\pi^0\pi^-}$ (Gev.)
3.3
2.3
2.5
2.1
1.7
1.3
0.3
0.7
1.1
1.5
1.9
(b)
$K^-P \to Y_1^{*+}\rho^-$
30
20
10
-1.0
0.0
1.0
Cos. $\theta_{pY_1^*}$
(c)
$K^-P \to Y_1^{*+}\pi^-$
$K^-P \to \Lambda^0\omega^0$
$K\,P \to Y_1^{*+}\rho^-$
4.0
4.0
8.0
4.0
$\frac{d\sigma}{dt}$
$\frac{\mu b.}{Gev.^2}$
0.0
1.0
2.0
$-t\,(Gev.)^2$

pseudoscalar (K) exchange than in the other two-body processes. This fact was also indicated by the fact that the momentum-transfer distribution was more peaked at small values than in the other two-body processes (see Fig. 5.7(c)).

TABLE 5.5

	Channel	Cross section μbn.
$K^- p \longrightarrow$	$\Lambda^\circ \eta^\circ$	2 ± 1
	$\Lambda^\circ \omega^\circ$	16 ± 4
	$\Lambda^\circ X^\circ (\rho^\circ\gamma)$	5 ± 2
	$Y_1^{*+} \rho^-$	16 ± 4
	$Y_1^{*\circ} \rho^\circ$	4 ± 4
	$Y_1^{*-} \rho^+$	$\leqslant 4$
	$Y_1^{*+} \pi^- \pi^\circ$	20 ± 10
	$Y_1^{*\circ} \pi^+ \pi^-$	10 ± 5
	$Y_1^{*-} \pi^+ \pi^\circ$	$\leqslant 5$
	$\Lambda^\circ \pi^+ \rho^-$	60 ± 10
	$\Lambda^\circ \pi^\circ \rho^\circ$	40 ± 10
	$\Lambda^\circ \pi^- \rho^+$	10 ± 5
	$\Lambda^\circ \pi^+ \pi^- \pi^\circ$	126 ± 30

5.3 Three-body channels.

The method of isolating the three-body channels was first to remove all other resonance channels and then, using a scatter plot of momentum transfer to the particle combination containing the resonance to be isolated against the effective mass of this particle combination, seleot a range of effective mass and momentum transfer which reduced the background of the resonance to a reasonably small level i.e. $\leq 25\%$. The cross section for these channels are given in Table 5.5.

The analysis performed on the three-body channels found in the $\Lambda^\circ\pi^+\pi^-\pi^\circ$ final state is essentially that outlined in Chapter 4 for the $\Lambda^\circ\pi^+\pi^-$ channel.

$$K^-p \longrightarrow \Lambda^\circ\pi^\circ\rho^\circ$$

The first step in the isolation of this channel was to remove events which had effective masses in the ρ^-, η°, ω°, and $X^\circ(\rho^\circ\gamma)$ resonance regions. The overlap of the ρ° with the η° and ω° was small but the η° and ω° events were removed so that a better estimate of the background could be made ; these events produce a strong reflection on the low-mass side of the ρ - mesons. It was not necessary to remove the $Y_1^{*+}(1385)$ events explicitly because the strong overlap with the ρ^- events meant that the removal of the ρ^- events also removed most of the $Y_1^{*+}(1385)$ events.

The second step was to study the scatter plot of the

momentum transfer between the incident K^- and the $\pi^+\pi^-$ mass combination against the $\pi^+\pi^-$ effective mass (Modified Chew-Low plot). This is shown in Fig. 5.9(a). There is an obvious cluster of events in the ρ° region at small momentum transfer. The ρ° region was defined by the mass range :

$$0.625 \leqslant M_{\pi^+\pi^-} \leqslant 0.875 \text{ Gev.}$$

This range was decided upon from a study of the $\pi^+\pi^-$ effective mass distribution and the modified Chew-Low plot. The background was defined by two mass ranges, of half the width of the ρ° mass range, either side of the ρ° .

i.e. Background (i) $\quad 0.450 \leqslant M_{\pi^+\pi^-} \leqslant 0.575$ Gev.

Background (ii) $\quad 0.925 \leqslant M_{\pi^+\pi^-} \leqslant 1.050$ Gev.

These background ranges were separated from the ρ° band by 50 Mev., in an attempt to reduce the effects of the Briet-Wigner tails of the ρ° peak. This background estimate is about 15% too small due to the curvature of the phase space distribution. Because of the small statistical level this effect was ignored. The background-subtracted momentum transfer distribution for events in the ρ° region is shown in Fig. 5.9(b), and shows that a large part of the ρ° production is at low momentum transfer ($\leqslant$ 1.2 Gev.^{2}). There is a smaller part which corresponds to large momentum transfers, but the signal to noise ratio is too small to allow a reasonable separation to be made. The mass projection of the modified Chew-Low plot is shown in Fig. 5.9(c),

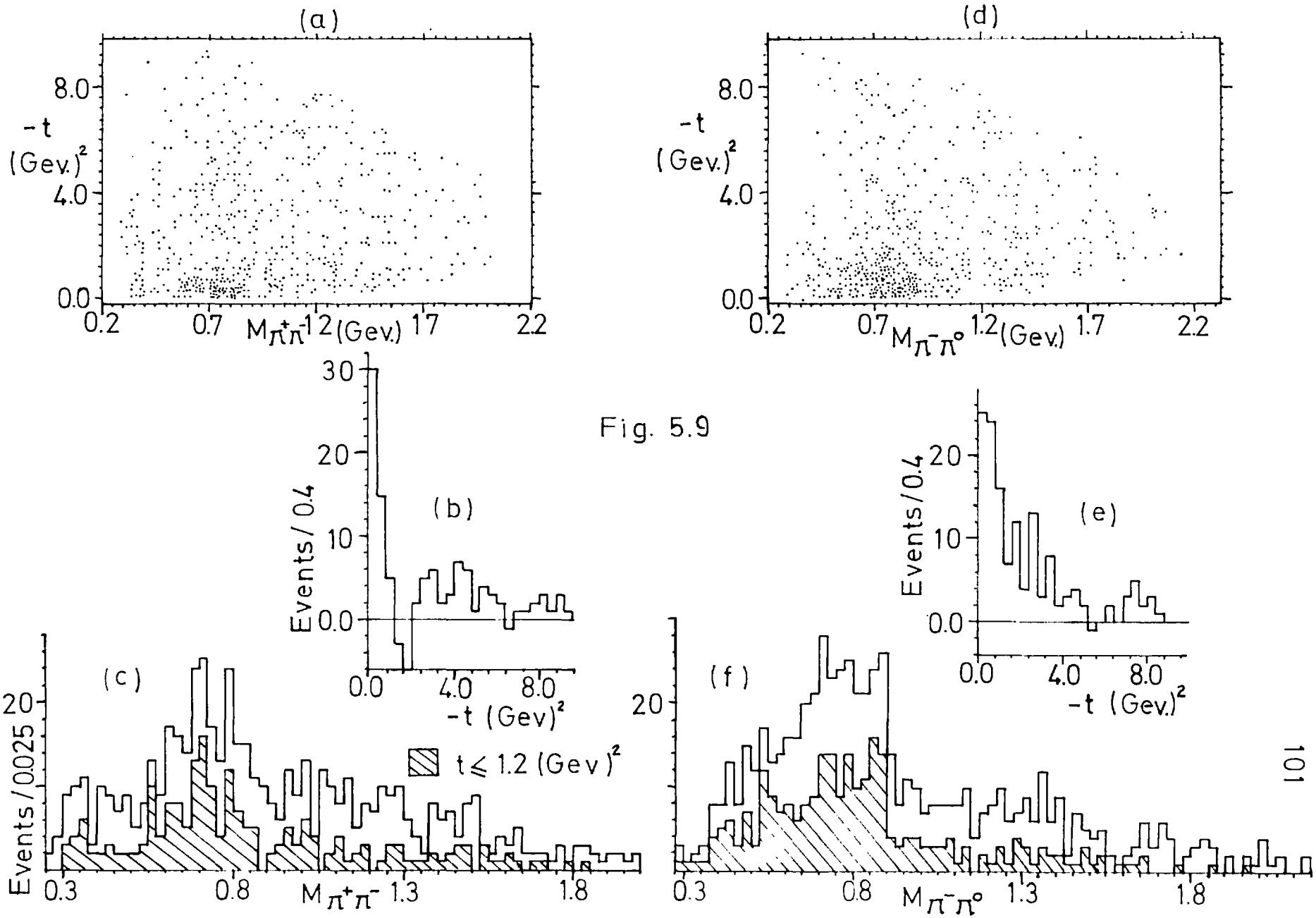

(a)
(d)
(b)
(e)
(c)
(f)
-t (Gev.)²
8.0
4.0
0.0
0.2
0.7
1.2
1.7
2.2
(Gev.)
Mπ⁺π⁻
Mπ⁻π°
Events/0.4
30
20
10
0.0
4.0
8.0
-t (Gev)²
Events/0.025
0.3
0.8
1.3
1.8
t≤1.2 (Gev)²

Fig. 5.9

with the low momentum transfer events shown shaded.

The $\Lambda^\circ\pi^\circ\rho^\circ$ channel was then selected after the removal of the resonances mentioned above by the criteria :

$0.625 \leqslant M_{\pi^+\pi^-} \leqslant 0.875$ Gev. and $-t_{K^-,\pi^+\pi^-} \leqslant 1.2$ Gev.^{2}

These criteria isolate the $\Lambda^\circ\pi^\circ\rho^\circ$ channel with the ρ° peripheral and gave a sample of 78 events with an estimated background of 20%. The loss of true $\Lambda^\circ\pi^\circ\rho^\circ$ events was about 30%, but most of these ρ°'s were less peripheral.

To study the kinematic characteristics of this channel the following histograms and scatter plots were produced :

(a) The production angular distributions for each particle in the K^-p centre of mass.

(b) The scattering angle of the π° with respect to the incident K^- in the $\rho^\circ\pi^\circ$ centre of mass and with respect to the incident proton in the $\Lambda^\circ\pi^\circ$ centre of mass.

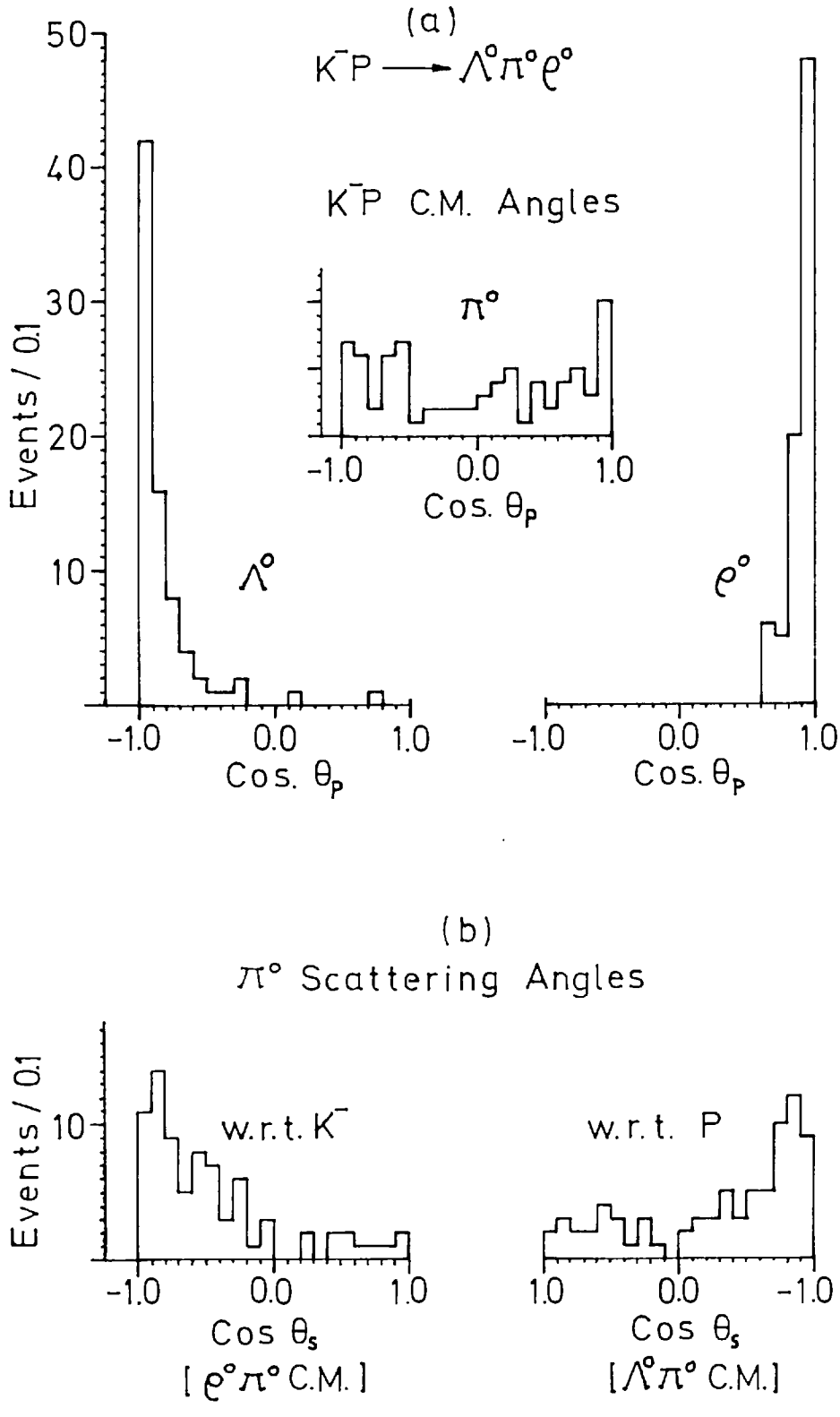
(c) The "Peyrou Plots" for each particle. The longitudinal momentum is defined positive in the direction of the incident K^-.

(d) The Dalitz plot and two-body effective mass distributions.

These are shown in Figs. 5.10(a), (b), 5.12(a), 5.13(a) and (c) respectively.

From the production angular distributions it is seen that the $\Lambda^\circ$is as peaked backwards as the $\rho^\circ$is forwards, while the π° is essentially isotropic. Both the scattering angular distributions (Fig. 5.10(b)) are very asymmetric, showing peaks at cos. $\theta_s \sim -1.0$.

Fig. 5.10


(a)
$K^-P \longrightarrow \Lambda^0\pi^0\rho^0$
K^-P C.M. Angles
π^0
Λ^0
ρ^0
Events / 0.1
50
40
30
20
10
-1.0
0.0
1.0
Cos. θ_P
(b)
π^0 Scattering Angles
w.r.t. K^-
w.r.t. P
Cos θ_s
[$\rho^0\pi^0$ C.M.]
[$\Lambda^0\pi^0$ C.M.]

These distributions indicate that the Λ° and π°, and $\rho^\circ$and π° in their respective centres of mass are produced in a manner similar to a real two-body process. From the Peyrou plot it is clearly seen that the Λ° and $\rho^\circ$are produced in opposite directions at high momenta (about 1.2 Gev.) and small angles, and the π° is produced with relatively small momentum ($\leq$ 0.5 Gev.) and isotropically. The Dalitz plot shows the tendency for the $\Lambda^\circ\pi^\circ$ and $\rho^\circ\pi^\circ$ effective masses to be small, and the $\Lambda^\circ\rho^\circ$ effective mass to be large. This is the effect of the extreme peripherality of the Λ° and ρ°, which constrains the events to lie in the left hand corner of the Dalitz plot (Fig. 5.13(a)). These features are seen in the $\Lambda^\circ\pi^\circ$, $\rho^\circ\pi^\circ$ and $\Lambda^\circ\rho^\circ$ effective mass histograms (Fig. 5.13(c)). There is a small amount ($10 \pm 5\%$) of contamination from the $Y_1^{*\circ}(1385)$ seen in the $\Lambda^\circ\pi^\circ$ effective mass distribution. The smooth curves drawn on these histograms are phase space distributions normalized to the total number of events. These are shown to emphasise the distortions of the effective mass distributions due to the three-body kinematics.

$$K^-p \longrightarrow \Lambda^\circ\pi^+\rho^-$$

The isolation of this channel follows, in general, the method used for the $\Lambda^\circ\pi^\circ\rho^\circ$ channel. In this case the resonances ω°, η° and $Y_1^{*+}(1385)$ were removed. The ρ°events were not removed because the $\pi^+\pi^-$ effective mass distribution for events in the ρ^- mass region showed no enhancement in the ρ° region. From a

study of the $\pi^-\pi^\circ$ effective mass distribution and the modified Chew-Low plot the ρ^- mass range was defined as :

$0.650 \leqslant M_{\pi^-\pi^\circ} \leqslant 0.900$ Gev. and the background by :

Background (i) $0.475 \leqslant M_{\pi^\circ\pi^-} \leqslant 0.600$ Gev.

Background (ii) $0.950 \leqslant M_{\pi^\circ\pi^-} \leqslant 1.075$ Gev.

with a separation of 50 Mev. from the ρ^- mass range. The modified Chew-Low plot for the $\pi^\circ\pi^-$ mass combination, the background-subtracted momentum transfer distribution for events in the ρ^- mass range and the mass projections of the modified Chew-Low plot with the small momentum transfer events shown shaded are shown in Figs. 5.9(d),(e) and (f) respectively.

The modified Chew-Low plot shows a well defined cluster of events in the ρ^-region at small momentum transfers, though less well defined than in the case of the ρ° . This difference is partly due to the loss of some very peripheral ρ^- events belonging to the $\Lambda^\circ\pi^+\rho^-$ channel due to the removal of the Y_1^{*+} events. The criteria used to isolate the $\Lambda^\circ\pi^+\rho^-$ channel was :

$0.650 \leqslant M_{\pi^-\pi^\circ} \leqslant 0.900$ Gev. and $-t_{K^-,\pi^\circ\pi^-} \leqslant 1.2$ Gev.^{2}

These criteria gave a sample of 120 events with a background of about 25% and a loss of true $\Lambda^\circ\pi^+\rho^-$ events of about 50%. The excluded ρ^- events in most cases have much larger momentum transfers.

The same plots were used for this channel as for the $\Lambda^\circ\pi^\circ\rho^\circ$ channel. The production angular distributions for each particle

in the K^-p centre of mass are shown in Fig. 5.11(a), the scattering angles of the π^+, defined in the same way as for the π° in the $\Lambda^\circ\pi^\circ\rho^\circ$ channel, are shown in Fig.5.11(b), the Peyrou plots are shown in Fig. 5.12(b), he Dalitz plots are shown in Fig.5.13(b) and the $\Lambda^\circ\pi^+$, $\rho^-\pi^+$ and $\Lambda^\circ\rho^-$ effective mass distributions are shown in Fig. 5.13(d). Again the Λ° is seen to be as peaked backwards as the ρ^- is forwards and the $\pi^+$is mainly isotropic. There is an excess of events at $\cos.(\theta_p)_{\pi^+} \sim -1.0$ in the distribution. This effect concerns about 20 events (17%). The scattering angular distributions for the π^+ are again very asymmetric showing peaks at $\cos.\theta_s \sim -1.0$. In the distribution of the π^+ scattering angle in the $\Lambda^\circ\pi^+$ centre of mass there is also a peak at $\cos.\theta_s \sim 1.0$. The events in this peak correspond to those in the peak in the π^+ production angular distribution. The Peyrou plots are similar to those of the $\Lambda^\circ\pi^\circ\rho^\circ$channel except that on the plot for the Λ° there are more events extending to the region of small longitudinal momenta and on the plot for the π^+ there are more events with large negative longitudinal momenta. The Dalitz plot shows the same accumulation of events in the left hand corner. This is due to the peripherality of the $\Lambda^\circ$and ρ^-. There were, in contrast to the $\Lambda^\circ\pi^\circ\rho^\circ$ Dalitz plot, more events with large $\rho^-\pi^+$effective masses. This feature is also seen in the $\rho^-\pi^+$ effective mass histogram. These events correspond to those in the peak in the π^+ production angular distribution, to those in

Fig. 5.11

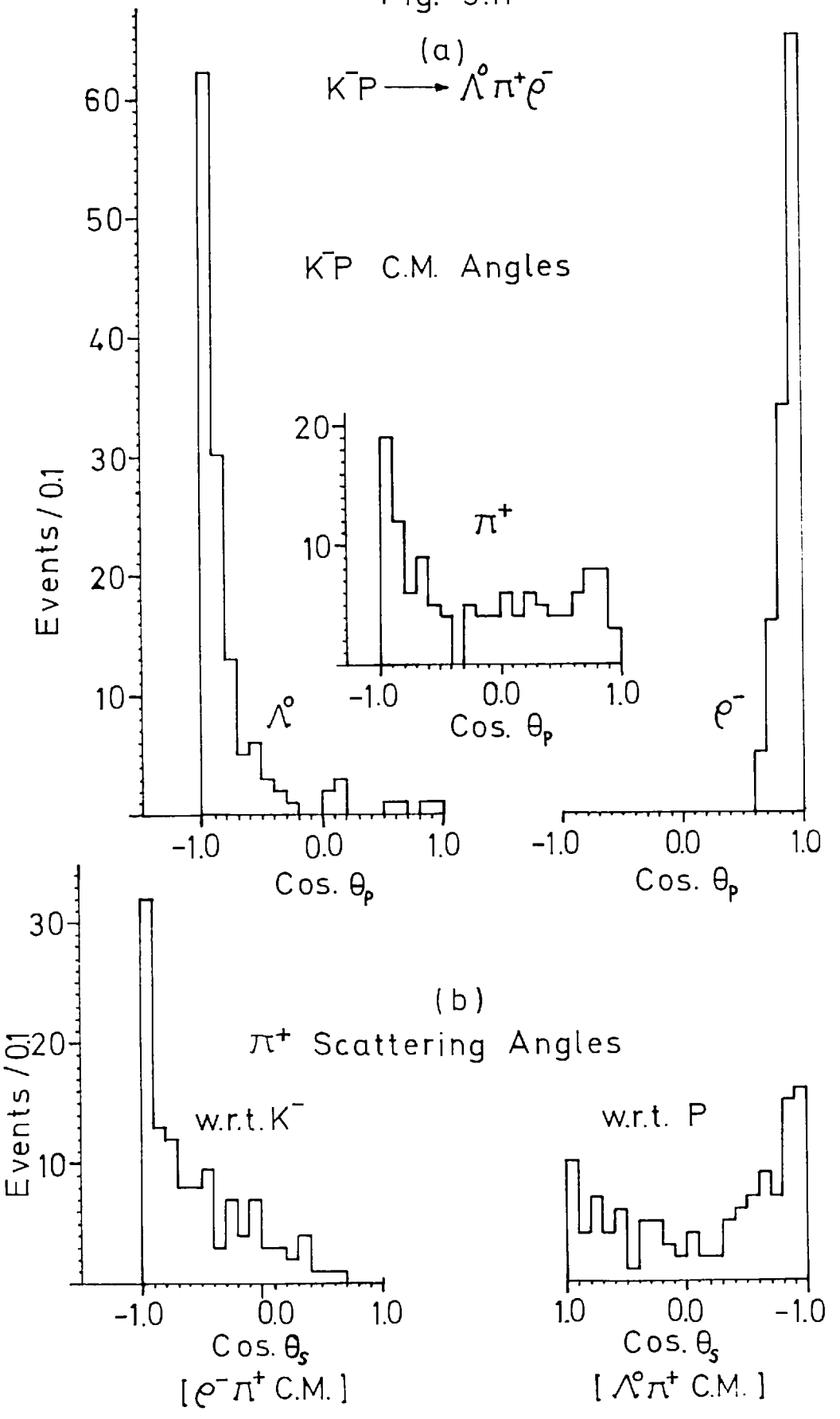
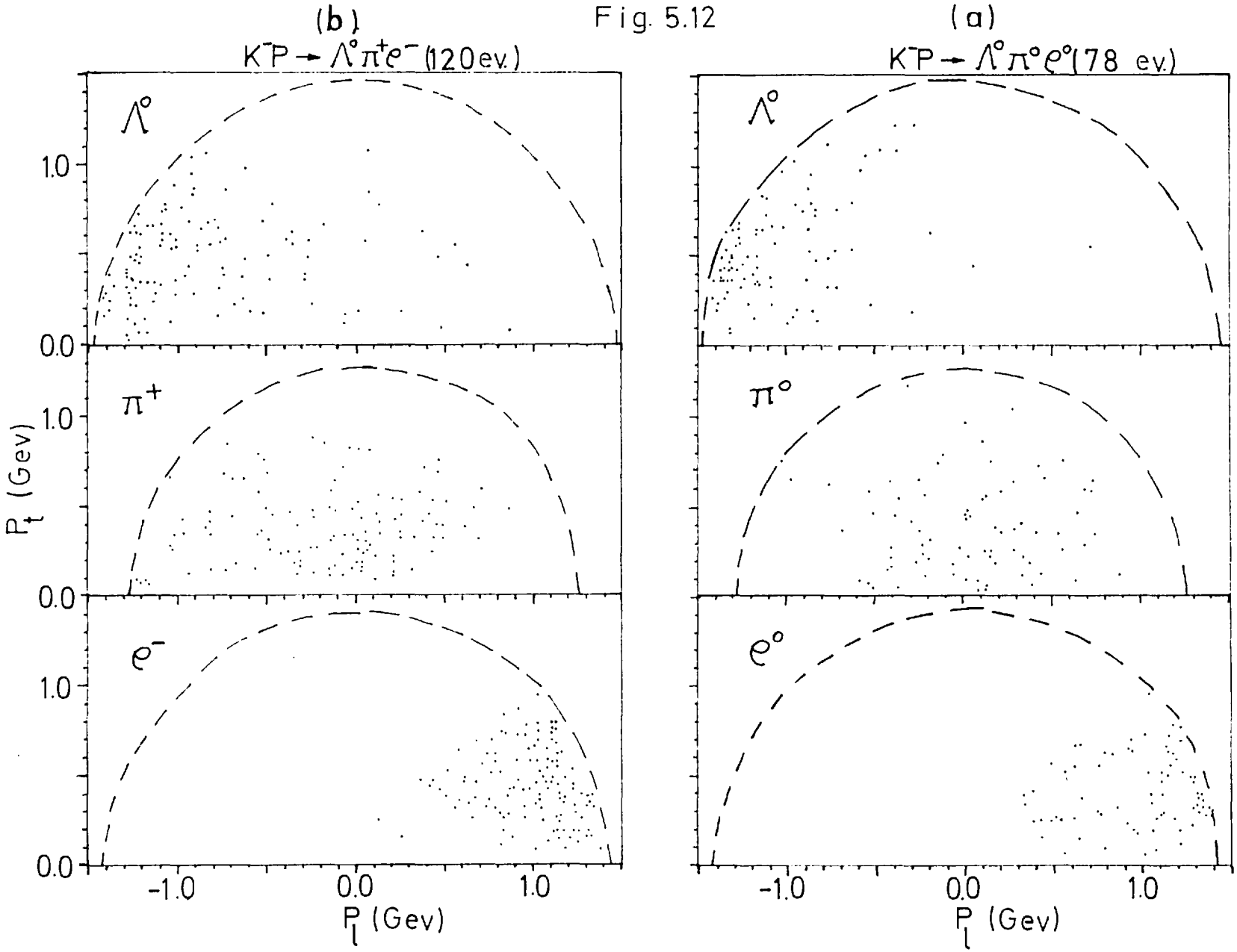

(a)
$K^-P \longrightarrow \Lambda^\circ \pi^+ \rho^-$
K^-P C.M. Angles
Events / 0.1
Λ°
π^+
ρ^-
Cos. θ_p
(b)
π^+ Scattering Angles
w.r.t. K^-
w.r.t. P
Cos. θ_s
[$\rho^- \pi^+$ C.M.]
[$\Lambda^\circ \pi^+$ C.M.]

Fig. 5.12


(b)
K⁻P → Λ°π⁺e⁻ (120 ev.)
Λ°
π⁺
e⁻
1.0
0.0
P_t (Gev)
-1.0
0.0
1.0
P_l (Gev)
(a)
K⁻P → Λ°π°e° (78 ev.)
Λ°
π°
e°
1.0
0.0
-1.0
0.0
1.0
P_l (Gev)

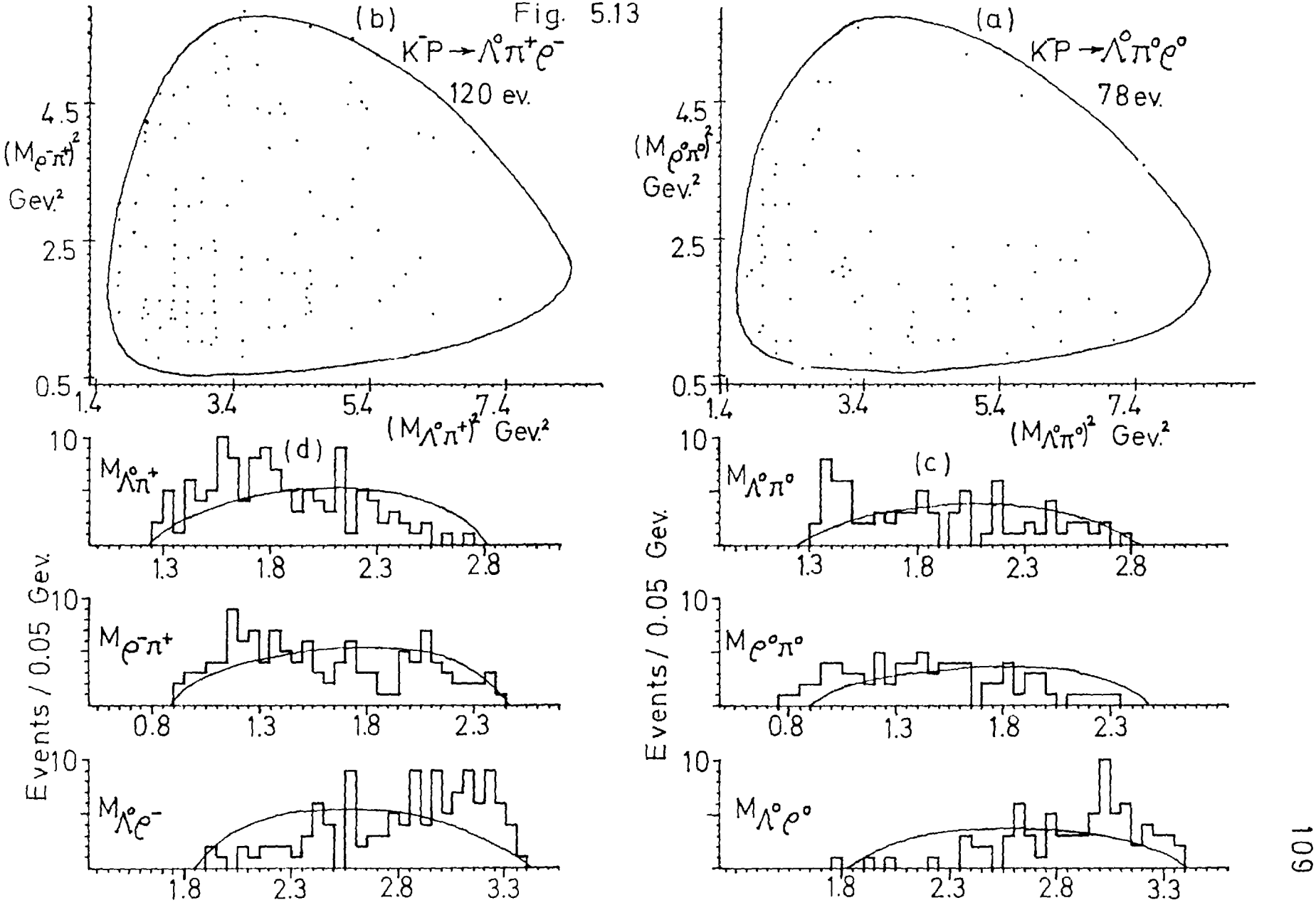

(b)
$K^-P \to \Lambda^0\pi^+\rho^-$
120 ev.
$(M_{\rho^-\pi^+})^2$ Gev.^{2}
4.5
2.5
0.5
1.4
3.4
5.4
7.4
$(M_{\Lambda^0\pi^+})^2$ Gev.^{2}
(a)
$K^-P \to \Lambda^0\pi^0\rho^0$
78 ev.
$(M_{\rho^0\pi^0})^2$ Gev.^{2}
$(M_{\Lambda^0\pi^0})^2$ Gev.^{2}
(d)
(c)
$M_{\Lambda^0\pi^+}$
$M_{\rho^-\pi^+}$
$M_{\Lambda^0\rho^-}$
$M_{\Lambda^0\pi^0}$
$M_{\rho^0\pi^0}$
$M_{\Lambda^0\rho^0}$
Events / 0.05 Gev.
10
1.3
1.8
2.3
2.8
0.8
3.3

Fig. 5.13

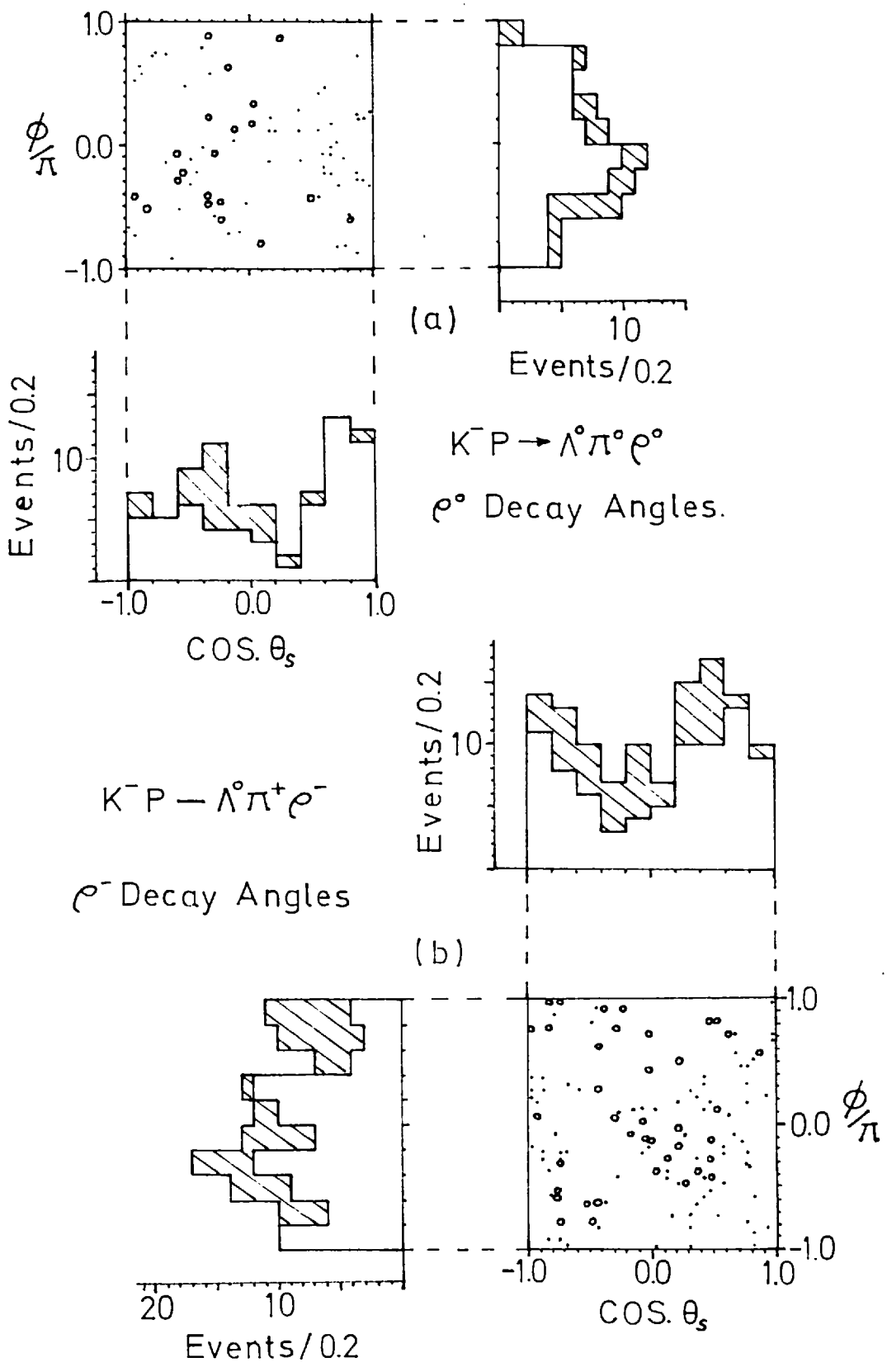
the peak in the π^+ scattering angular distribution in the $\Lambda^\circ\pi^+$ centre of mass and to those with low Λ° longitudinal momentum and high π^+ longitudinal momentum.

It is important to note that there tends to be a depopulation of events with large $\Lambda^\circ\pi^\circ$ and $\Lambda^\circ\pi^+$ masses due to the peripheral selection criteria used on the ρ° and ρ^- . These criteria, however, only emphasise the natural feature of peripheral ρ -meson production.

It is seen from the above discussion of the kinematic features of the $\Lambda^\circ\pi^\circ\rho^\circ$ and $\Lambda^\circ\pi^+\rho^-$ channels that they are essentially the same as those shown by the $\Lambda^\circ\pi^+\pi^-$ channel and are consistent with a double peripheral production mechanism. A discussion of some features of this model and its application to the main three-body channels will be given in Chapter 6.

Assuming that the ρ° and ρ^- are produced by a simple particle exchange mechanism between the π° and ρ°, and the π^+ and ρ^- the conventional analysis of the ρ -meson decay distributions was carried out. The scatter plots of the scattering angle ($\cos.\theta_s$) against the azimuthal angle (φ) and their projections for the ρ° and ρ^- are shown in Figs. 5.14(a) and (b) respectively. The open circles shown on the scatter plots and the shaded events in the projected histograms correspond to events with the ρ° and ρ^- production angle cosine $\leqslant 0.85$, which is approximately equal to the momentum transfer being $\geqslant 0.7$ Gev.^{2} To

Fig. 5.14


1.0
0.0
-1.0
ϕ/π
Events/0.2
10
(a)
$K^-P \rightarrow \Lambda^\circ\pi^\circ\rho^\circ$
ρ° Decay Angles.
-1.0
0.0
1.0
COS. θ_s
$K^-P \rightarrow \Lambda^\circ\pi^+\rho^-$
ρ^- Decay Angles
(b)
20

obtain information about the quantum numbers of the system exchanged between the π° and ρ° , and the π^+ and ρ^- the ρ - parameters were calculated for the ρ° and ρ^- by fitting their decay distributions to the expression for the decay of a 1^- particle into two 0^- particles using a moments method. The results of this fitting are shown in Table 5.6. The values of the ρ -parameters are averaged over the momentum transfer range :

$$0.0 \leq -t_{K^-,\rho^\circ \text{ or } \rho^-} \leq 1.2 \text{ Gev.}^2$$

TABLE 5.6

Channel	ρ_{oo}	$\rho_{1,-1}$	Re $\rho_{1,0}$
$\Lambda^\circ\pi^\circ\rho^\circ$	0.45 ± 0.08	-0.06 ± 0.05	-0.01 ± 0.04
$\Lambda^\circ\pi^+\rho^-$	0.45 ± 0.07	-0.05 ± 0.05	-0.03 ± 0.04

If absorption effects are neglected these values indicate that the exchange mechanism in both channels is about 50% pseudoscalar (K) and 50% vector (K^*). It is seen from the unshaded projected histograms that there is an increase in the amount of pseudoscalar exchange ($\theta_s \longrightarrow \cos.^2\theta_s$) for the more peripheral ρ° and ρ^- events. There is the familiar ρ° decay asymmetry present in the ρ° scattering angular distribution.

$$K^-p \longrightarrow Y_1^{*+}\pi^-\pi^\circ$$

This channel was originally thought to be very strong, but on applying the missing mass cut offs described in Chapter 3 the intensity was greatly reduced. This implies that the events were

mostly due to the $Y_1^{*+}\pi^-\pi^\circ\pi^\circ$ channel. This was further substantiated by the fact that there was strong Y_1^{*+} production in the multineutral events. The background- subtracted histogram of the momentum transfer from the proton to the Y_1^{*+} with the ρ^- events removed showed that no reasonable separation of this channel was possible. Approximately 60% of all Y_1^{*+} production is associated with the ρ^-. Some of the remaining Y_1^{*+} events are a reflection of a small enhancement (about 13 events) seen in the $\Lambda^\circ\pi^+\pi^\circ$ effective mass distribution at about 1660. The reflection is due to the limited $\Lambda^\circ\pi^+$ phase space. This enhancement is tentatively assigned to the $Y_1^{*+}(1660)$.

5.4 The four-body channel

$$K^-p \longrightarrow \Lambda^\circ\pi^+\pi^-\pi^\circ$$

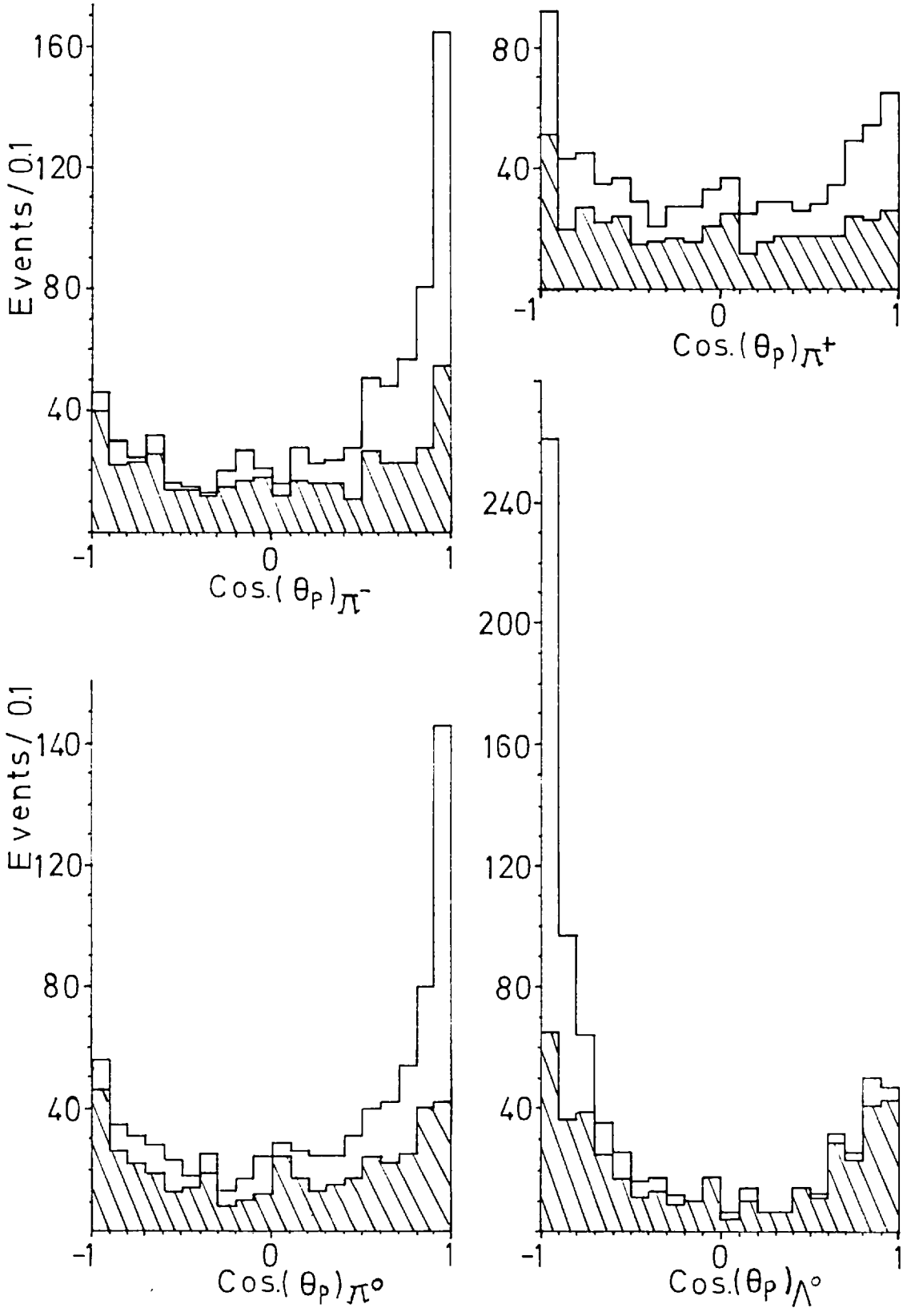
This non-resonant four-body state was estimated, from the Briet-Wigner fits discussed at the beginning of this chapter, to consist of 350 ± 50 events. This corresponds to a cross section of about 130 μbn (see Table 5.5). Hence this channel has the largest cross section almost by an order of magnitude and purely for this reason warrants some study. In previous experiments these multi-body non-resonant channels were not studied presumably becauss of the inherent difficulties involved in the analysis when more than two bodies are produced. For this channel only approximate qualitative conclusions will be made in view of the statistical limitations.

The non-resonant events were selected by removing all the resonance channels defined previously. These are the $Y_1^{*+}(1385)\,\pi^-\pi^\circ$ $\Lambda^\circ\omega^\circ$, $\Lambda^\circ\eta^\circ$, $\Lambda^\circ X^\circ(\rho^\circ\gamma)$, $\Lambda^\circ\pi^\circ\rho^\circ$, $\Lambda^\circ\pi^+\rho^-$, and $Y_1^{*+}(1385)\,\rho^-$. This criteria gives a sample of 430 events with a contamination of about 25% and a loss of true non-resonant events of about 12%. These lost events will be highly biased due to the criteria used to define the resonant channels. However because the bias is small and tends to be cancelled by the remaining peripheral resonances it has been ignored.

A study of the effective mass distributions shows that in most cases a phase-space distribution fits reasonably well. Some representative examples are shown as shaded histograms, with phase space curves superimposed, in Figs. 5.2, 3 and 4. There are small differences in the $\Lambda^\circ\pi^-$, $\Lambda^\circ\pi^+\pi^-$ and $\Lambda^\circ\pi^-\pi^\circ$ distributions, with more events in the large-mass regions, and in the $\pi^+\pi^\circ$ distribution with more events in the low-mass region. The method of analysis for this channel was to search for correlations between the production angles of the particles in the K^-p centre of mass. The approximate consistency of the effective mass distributions with phase space suggests that a statistical model of the production process is valid. This model is however inconsistent with the production angular distributions of each particle. These distributions are shown as shaded histograms in Fig. 5.15. The unshaded parts correspond to the resonances

Fig. 5.15

$K^-P \rightarrow \Lambda^\circ \pi^- \pi^+ \pi^\circ$ Production Angles



which were removed. The π° and π^{-} distributions still show peripheral features, but the Λ° distribution is very different to the other distributions in that it is strongly peaked at $\cos.(\theta_p)_{\Lambda^{\circ}} \sim 1.0$ and -1.0. Since the Λ° distribution shows distinct peripheral features it was used as a basis for the subsequent analysis. In an attempt to isolate the peripheral events the production angular distribution of the Λ° was divided into three regions. These were :

$$\text{(i)} \quad \cos.(\theta_p)_{\Lambda^{\circ}} \leqslant -0.5$$

$$\text{(ii)} \quad \cos.(\theta_p)_{\Lambda^{\circ}} \geqslant 0.5$$

$$\text{(iii)} \quad -0.5 < \cos.(\theta_p)_{\Lambda^{\circ}} < 0.5$$

Events in region (i) were defined as backward Λ° events and events in region (ii) as forward Λ° events. The events in region (iii) were considered to be produced by a statistical process and were not used in the following analysis. These criteria gave a ratio of peripheral to isotropic events in region (i) of about 3:1 and in region (ii) of about 2.5:1. The production angular distributions of the pions associated with the backward Λ° events are shown in Fig. 5.16(a). Strong peaks are seen in the π^{-} and π° distributions at $\cos.(\theta_p)_{\pi^-}$ or $\pi^{\circ} \sim 1.0$ (i.e. forwards). An enhancement is seen in the π^{+} distribution but this is not as peaked or as strong as the π^{-} or π° peaks. Because the π^{-} forward peak is strongest a further selection was made on the basis of this distribution. This selection was to divide the

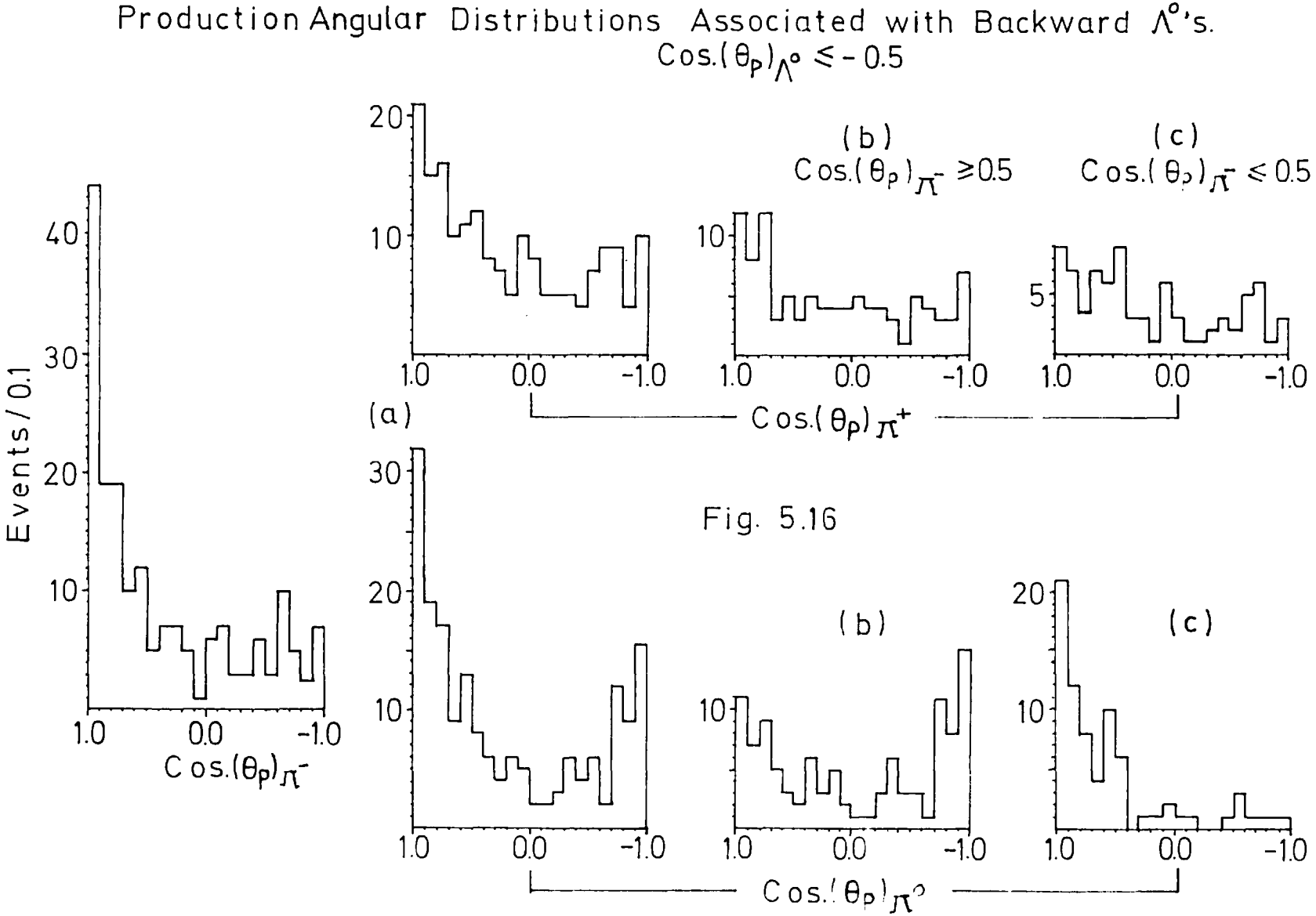

Production Angular Distributions Associated with Backward Λ°'s.
Cos.(θp)Λ° ≤ -0.5
(a)
(b)
Cos.(θp)π⁻ ≥0.5
(c)
Cos.(θp)π⁻ ≤0.5
Events / 0.1
Cos.(θp)π⁻
Cos.(θp)π⁺
Cos.(θp)π°
1.0
0.0
-1.0

Fig. 5.16

distribution into two parts :

$$(i(a)) \qquad \cos.(\theta_p)_{\pi^-} > 0.5$$

$$(i(b)) \qquad \cos.(\theta_p)_{\pi^-} < 0.5$$

The π° and π^+ distributions corresponding to these regions are shown in Figs. 5.16(b) and (c) respectively. These distributions show that the π° and π^- forward peaks are essentially independent.

The production angular distributions of the pions associated with the forward Λ° events are shown in Fig.5.17(a). Again there is a strong peaking of the π^- but in this case in the backward direction ($\cos.(\theta_p)_{\pi^-} \sim -1.0$). Strong backward peaks are also shown in the π° and π^+ distributions. As before the π^- distribution was used as the basis for a further selection criteria. These were :

$$(ii(a)) \qquad \cos.(\theta_p)_{\pi^-} < -0.5$$

$$(ii(b)) \qquad \cos.(\theta_p)_{\pi^-} > -0.5.$$

The π° and π^+distributions corresponding to these two regions are shown in Figs. 5.17(b) and (c). The events shown shaded on the π° and π^+distributions correspond to each other. All these distributions show that the π^-,π° and π^+ backward peaks are all independent.

The results of this analysis are that the Λ° 's produced peripherally backwards are associated with either π°'s or π^-'s produced peripherally in the forward direction and that the Λ°'s produced peripherally forwards are associated with either π^-'s or π^+'s or π°'s produced peripherally backwards. An

Production Angular Distributions Associated with Forward Λ^0's

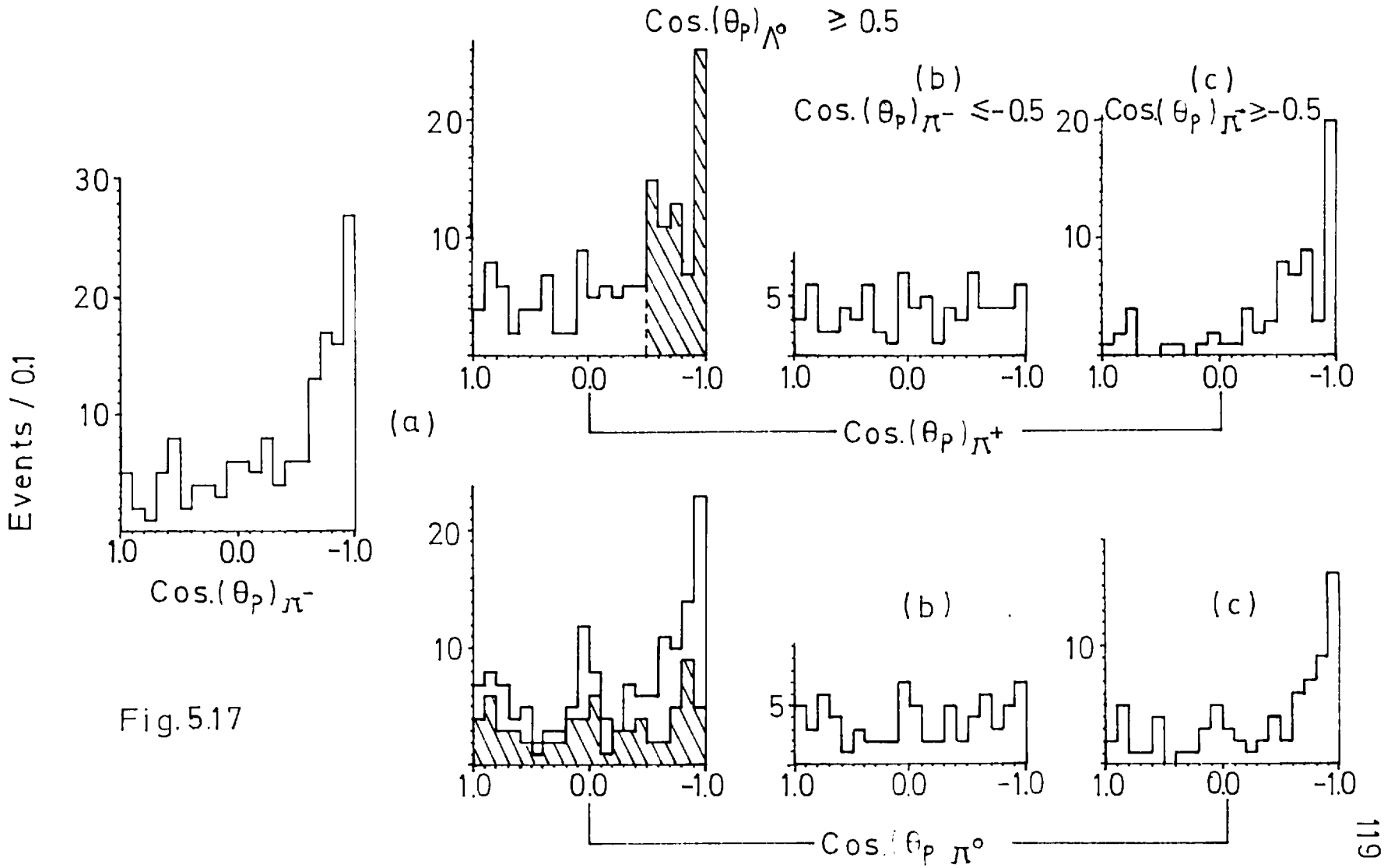
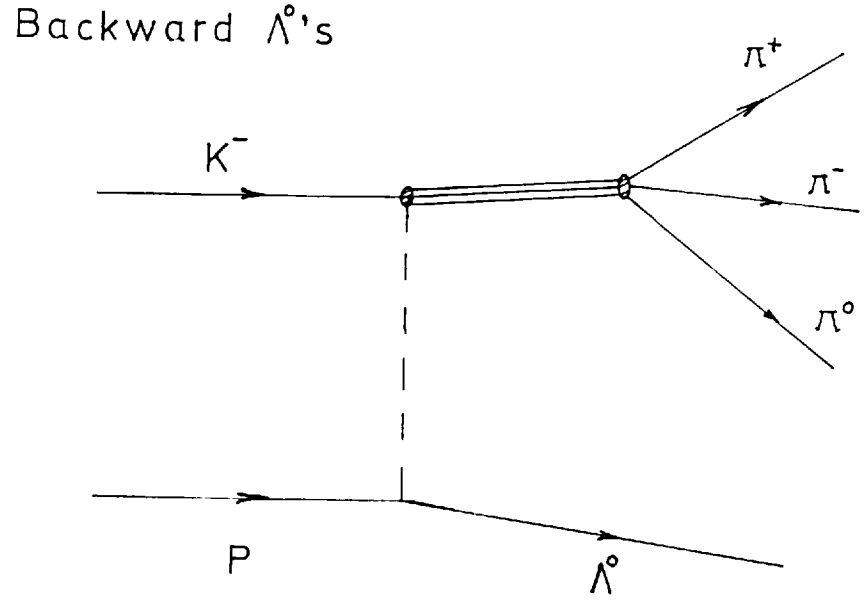


Fig. 5.17

interpretation of these results could be in the form of a triple peripheral production mechanism. This interpretation will be discussed in Chapter 6.

An alternative interpretation of the strong forwad and backward peaking of the Λ° production angular distribution is that for the forward Λ°s the Λ° is produced at the kaon vertex and the pions are all emitted from the baryon vertex and for the Λ°'s produced backwards the Λ° is produced at the baryon vertex and the pions at the kaon vertex. Feynman diagrams for these two situations are shown in Fig. 5.18(a). In these processes the pions can be regarded as forming a variable mass object which behaves internally in a statistical manner. This means that the object will decay isotropically into three pions. To test this the scattering angle of each pion with respect to the direction of the incident K^{-} in thh three pion centre of mass was calculated for the forward and backward Λ° 's separately. These distributions are shown in Fig. 5.19. It is seen that there is a strong isotropic component in each distribution which are therefore consistent with the above model.



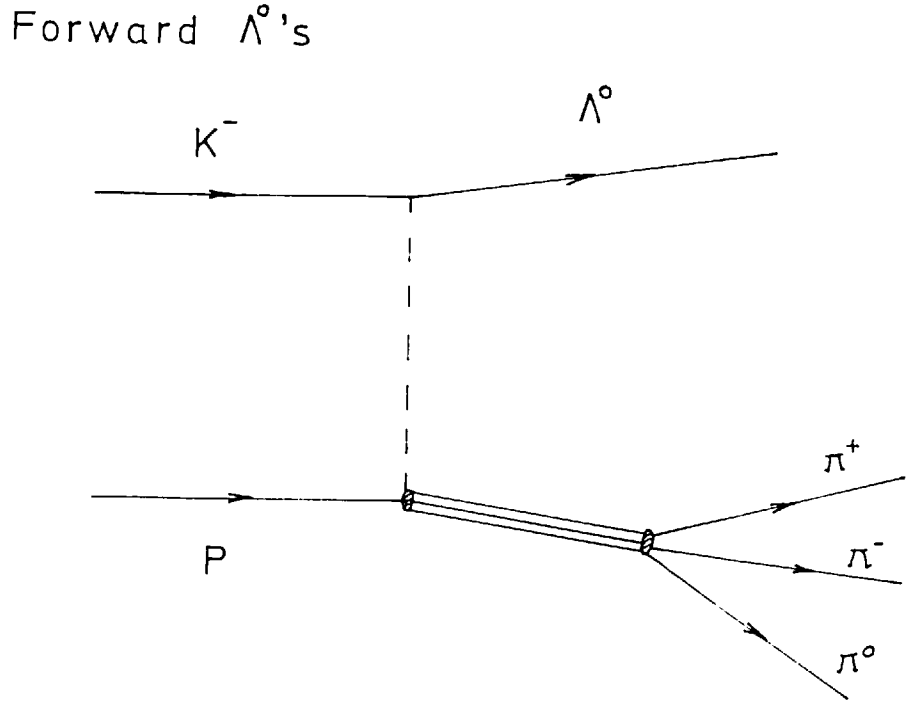


Fig. 5.18.

Scattering Angles for π^-, π^+ and π^o in the $\pi^-\pi^+\pi^o$ c.m.

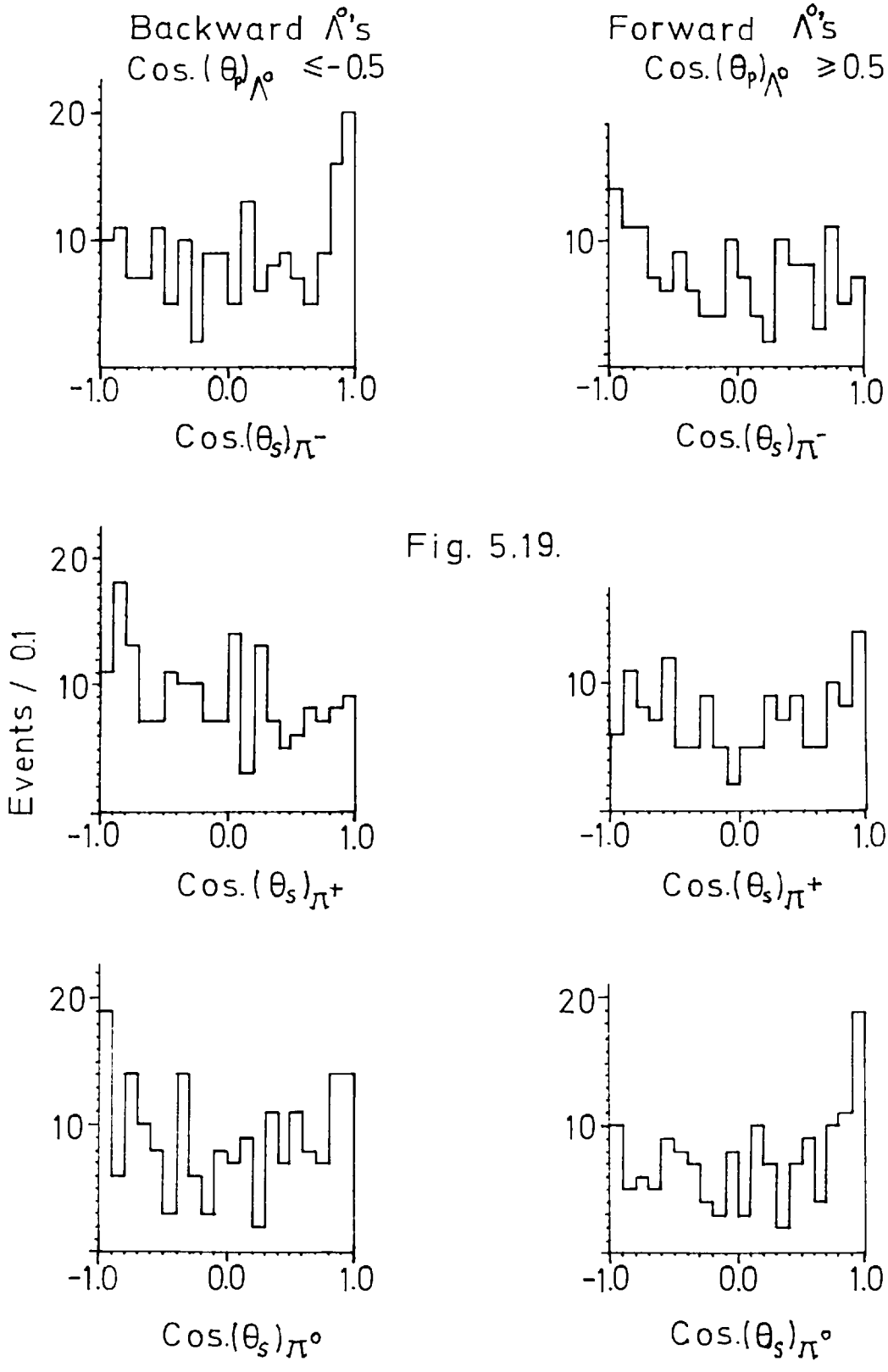


Fig. 5.19.

CHAPTER 6

In this chapter comparisons with simple theory and other experiments are made.

6.1 Two-body channels.

The main two-body channels produced in the $\Lambda^\circ\pi^+\pi^-$ and $\Lambda^\circ\pi^+\pi^-\pi^\circ$ final states are $Y_1^{*+}(1385)\ \pi^-$, $\Lambda^\circ\omega^\circ$ and $Y_1^{*+}(1385)\ \rho^-$. The cross section of all of these channels continues the trend of decreasing with increasing energy as exhibited at lower energies. The plot of the logarithm of the cross section against the logarithm of the incident momentum for each of the above channels are shown in Fig. 6.1. Straight lines were fitted to these points which gave the relations :(6.1)

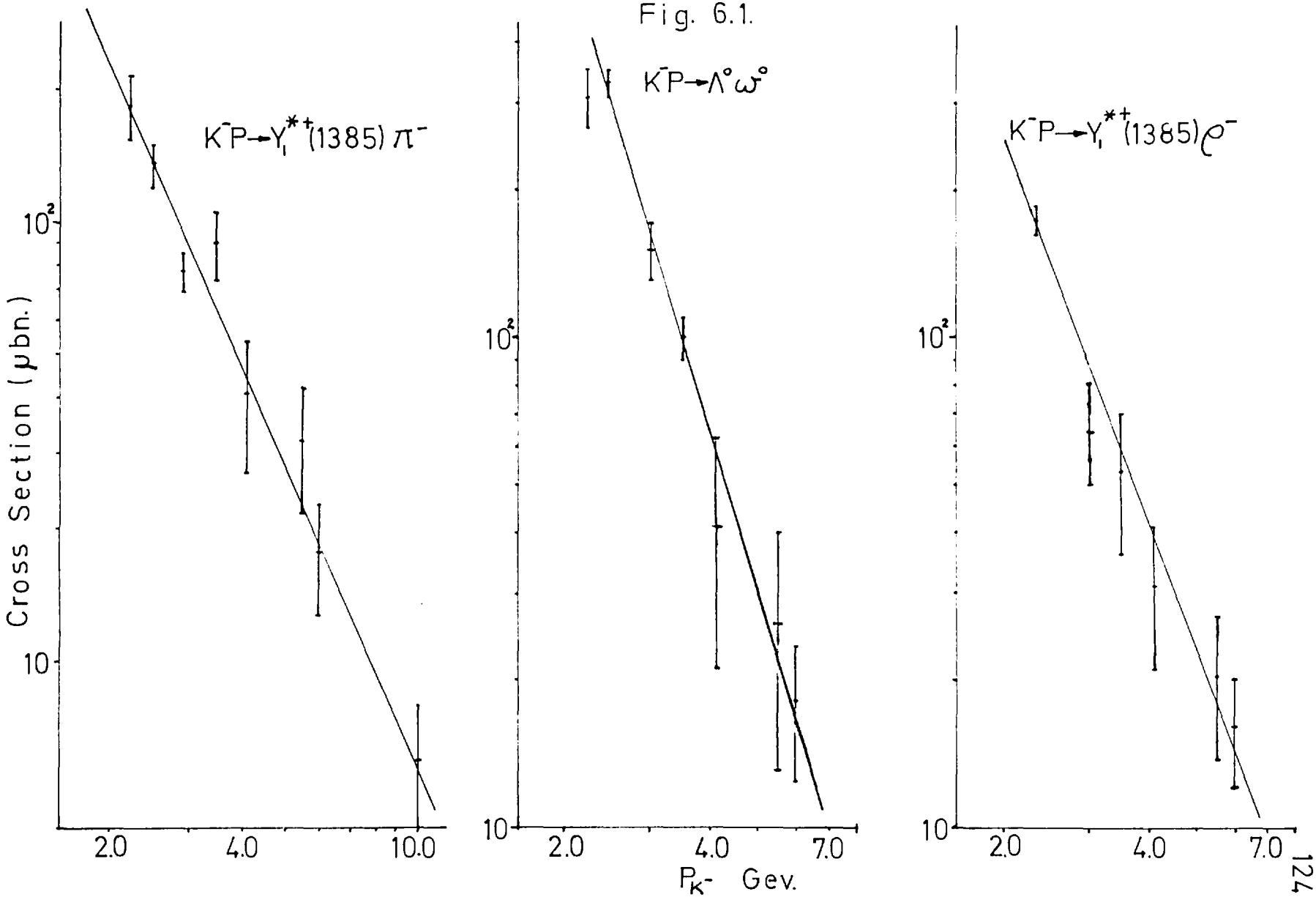
$$\sigma_{Y_1^{*+}\pi^-} \sim S^{-5.2\ +0.7\ -0.6}$$

$$\sigma_{\Lambda^\circ\omega^\circ} \sim S^{-9.6\ +1.0\ -3.0}$$

$$\sigma_{Y_1^{*+}\rho^-} \sim S^{-5.1\ +2.0\ -1.0}$$

The angular and momentum transfer dependence of the $\Lambda^\circ\omega^\circ$ and $Y_1^{*+}\pi^-$ amplitude for our energy and lower energies(6.2) are shown in Fig. 6.2. For the $Y_1^{*+}\pi^-$ there is little change in the angular dependence except for a small sharpening of the peak at $\cos.(\theta_p)_{Y_1^{*+}} \sim -1.0$. The $\Lambda^\circ\omega^\circ$ channel however is very different. At the lowest energy the distribution is almost isotropic and then it gradually changes into distinct forward and backward peaks as centre of mass enegy increases. There is very little data with

Fig. 6.1.


$K^-P \to Y_1^{*+}(1385)\pi^-$
$K^-P \to \Lambda^\circ\omega^\circ$
$K^-P \to Y_1^{*+}(1385)\rho^-$
Cross Section (μbn.)
10^2
10
2.0
4.0
10.0
7.0
P_{K^-} Gev.

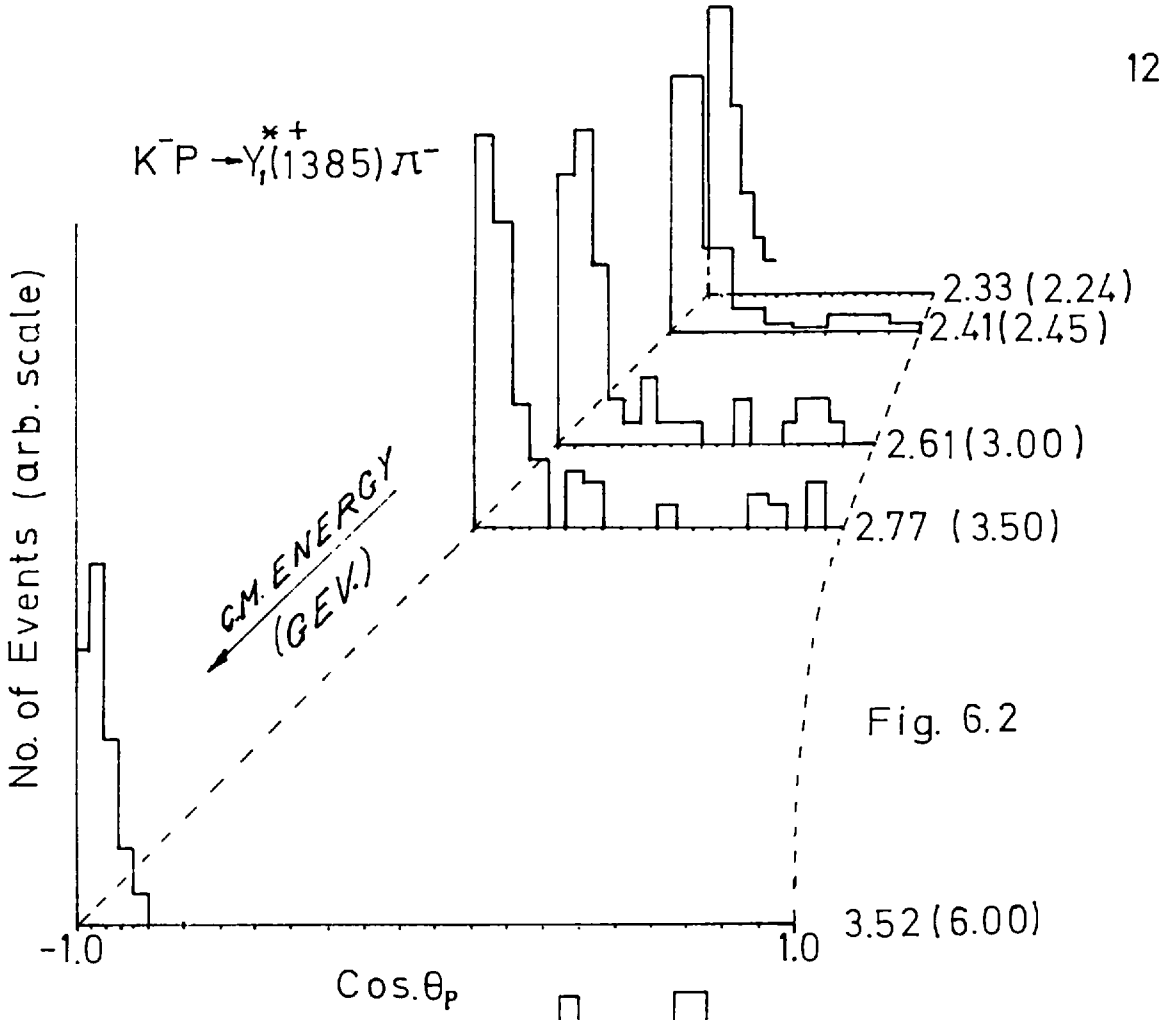
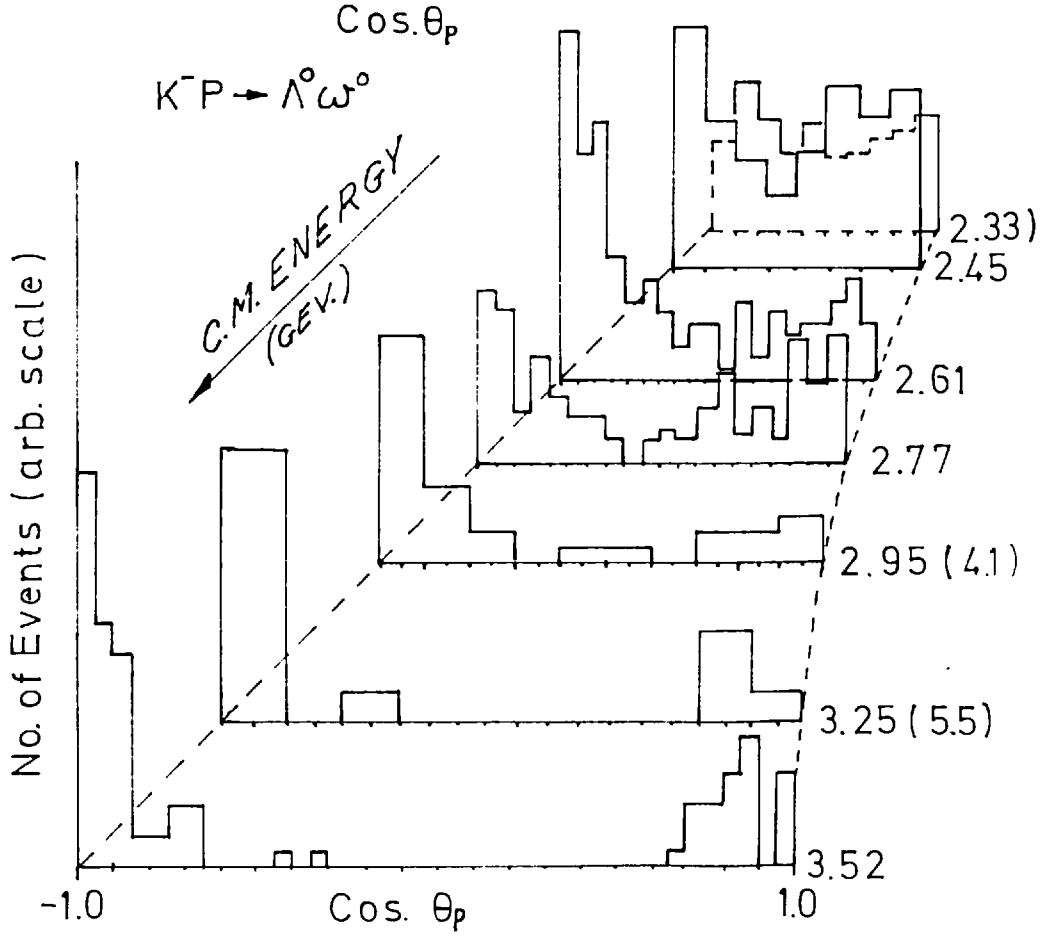

$K^-P \rightarrow Y_1^{*+}(1385)\pi^-$
No. of Events (arb. scale)
C.M. ENERGY (GEV.)
2.33 (2.24)
2.41 (2.45)
2.61 (3.00)
2.77 (3.50)
3.52 (6.00)
-1.0
1.0
Cos. θ_p

Fig. 6.2

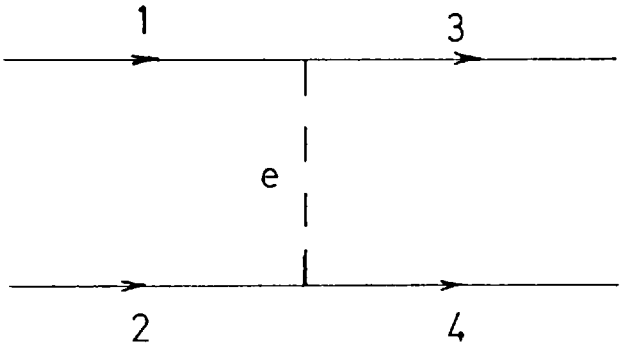

$K^-P \rightarrow \Lambda^0\omega^0$
No. of Events (arb. scale)
C.M. ENERGY (GEV.)
2.33)
2.45
2.61
2.77
2.95 (4.1)
3.25 (5.5)
3.52
-1.0
1.0
Cos. θ_p

which to compare for the $Y_1^{*+}(1385)\,\rho^-$ channel but it appears to be similar to that for the $Y_1^{*+}\pi^-$ channel. Thus for the $Y_1^{*+}\,\pi^-$ and $Y_1^{*+}\rho^-$ there is only a strong dependence on S (centre of mass energy) and a fixed dependence on the momentum transfer (t) which is the same for each value of S for S >2 Gev.

In the case of the $\Lambda^\circ\omega^\circ$ channel there is a simultaneous dependence on t and S which is complicated by the presence of a forward and backward peripheral amplitude which completely dominates at the higher energies.

The $Y_1^{*+}\,\pi^-$ and $\Lambda^\circ\omega^\circ$ are produced with almost all the events in the small momentum transfer region $-t < 1.0$ Gev.^{2} (ignoring the backward ω° events in the $\Lambda^\circ\omega^\circ$ channel). Thus a peripheral production mechanism is obvious. The simple one-meson exchange diagrams (O.M.E.) for the $Y_1^{*+}\pi^-$ and $\Lambda^\circ\omega^\circ$ channels are shown in Fig. 6.3. The the dependence of the differential cross section on t has been seen to be predicted incorrectly by O.M.E. model, being too large at large t. The Absorption model which is a modified O.M.E. model damps out the large t part of the amplitude by absorbing it into other processes. Thus it is essentially a mixture of an optical model and a O.M.E. model. The size of the absorbing region is determined from the data on the elastic scattering of the initial state particles at the energy considered. This model predicts a correlation of the decay distribution with momentum transfer and between cos. θ_s and

Two-Body Process $1 + 2 \rightarrow 3 + 4$



Three-Body Process $1 + 2 \rightarrow 3 + 4 + 5$

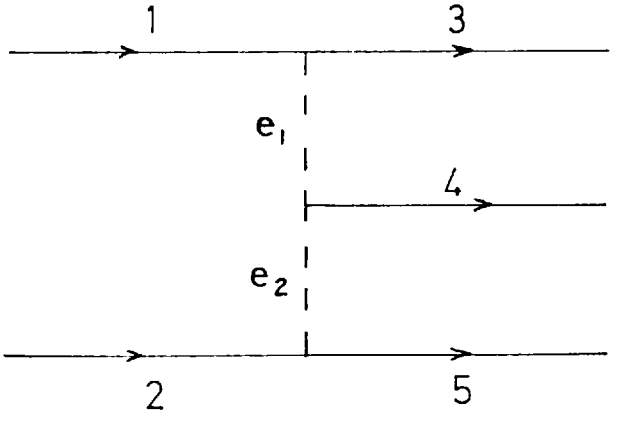


Fig. 6.3.

ϕ . These correlations can be understood as a mixing of the O.M.E. amplitude with that of the absorbing region which produces the same final state. The amount of mixing will depend on the momentum transfer. For channels dominated by pion exchange the "size" of the absorbing region is small relative to the pion range and absorption effects provide a small correction to the t dependence of the differential cross section. At low energies the absorption model works well for the pion-exchange channels and correctly predicts the correlations of the decay distributions.(6.3) But for high energies and for channels dominated by the exchange of a vector meson, which is more massive than a pion, the absorptive corrections are large and,as one would expect, disagreement is found. The variation of the differential cross section with t for these channels as predicted by the absorption model, which is better than that predicted by the O.M.E. , is still too large at large t and the S dependence, being essentially the same as that given by the O.M.E. model, is completely wrong i.e. $\frac{d\sigma}{dt} \sim S^{2j-2}$ where j = the spin of the exchanged particle. It thus predicts diverging cross sections with increasing energy, which eventually violates the unitarity of cross section . A recent critiscism, made by Selleri(6.4), has been that absorption should not be included in a model for peripheral processes because by considering a O.M.E. diagram one is considering the amplitude at small t only. He considers that a O.M.E. diagram should contain

all the features of a strongly collimated peripheral amplitude. For pion exchange this is essentially true for small t. According to Selleri the modifications to the simple O.M.E. model should be of the form factor type. Physically this modification attempts an empirical parametrization, based on experimental data, of the unknown effects of the "of the mass shell" nature of the exchanged particle and its coupling to the other particles. The form factor is a function of t and is calculated from the distribution of the experimental differential cross section. The test of this approach is the universality of the form factor for a particular process over the experimentally available energy range. However it is not inconceivable that the form factors have some S dependence also. A strong criticism of the form factor approach is the fact that to obtain agreement with the experimental dependence of the differential cross section on t the form factor must contain almost all the t dependence of the amplitude and overshadows the intrinsic t dependence of the O.M.E. model.

The last model to be briefly discussed is the Regge Pole Model[6.5]. This model is derived from transforming the partial wave expansion of the scattering amplitude, which is a sum of discrete angular momentum states, into an integral expression in terms of a continuous angular momentum variable. This variable is a generalised complex angular momentum. The expression so obtained contains "poles" (singularities) in the complex angular

momentum plane. Expressing this form of the amplitude in terms of the variables S and t and considering the crossed channel where S is the four-momentum transfer and t is the centre of mass energy the poles at integer values of the real part of the complex angular momentum variable $\alpha(t)$ can be identified with the physical particles. The value of the variable $\alpha(t)$ at the integer values corresponds to the total spin quantum number of the particle. The expression can be simplified by taking the limit $S \longrightarrow \infty$. The resulting expression can the be continued into the uncrossed channel where t is the four momentum transfer and S is the centre of mass energy and the limit $S \longrightarrow \infty$ is the high energy asymptotic limit. In the physical region of this channel there is a continuous monotonic variation of the real part of $\alpha(t)$. The graphical representation of these features is given by the Chew-Frautschi plot[6.6]. This theory replaces the concept of a particle by the concept of a"Reggeized" particle, which is represented by a smooth curve (trajectory) on the Chew-Frautschi plot, and can be regarded as a "family" of particles. The formula for scattering in the asymptotic limit is given by this theory is :

$$d\sigma/dt = |f_S(S,t)|^2 \cong \beta(t) S^{2\alpha(t)-2}$$

Thus the Regge pole model does not predict diverging cross sections with energy because the function $\alpha(t) \leqslant 1$ and does include a form factor ($\beta(t)$) as a natural consequence of the theory.

The decay density matrix elements (ρ -parameters) for the resonances produced in the $Y_1^{*+}\pi^-$ and $\Lambda^\circ\omega^\circ$ channels at various energies will now be compared. The values are shown in Table 6.1. There is insufficient data on the $Y_1^{*+}\rho^-$ channel to allow such a comparison to be made.

TABLE 6.1

$K^-p \longrightarrow Y_1^{*+}\pi^-$

Beam Momentum (Gev.)	c.m. Energy (Gev.)	ρ_{33}	Re $\rho_{3,1}$	Re $\rho_{3,-1}$
2.24	2.33	0.31 ± 0.05	0.03 ± 0.04	0.27 ± 0.04
3.46	2.77	0.34 ± 0.06	0.00 ± 0.09	0.17 ± 0.09
4.10	2.95	0.35 ± 0.07	0.16 ± 0.10	0.16 ± 0.07
6.02	3.52	0.23 ± 0.08	0.10 ± 0.07	0.12 ± 0.08

$K^-p \longrightarrow \Lambda^\circ\omega^\circ$

		ρ_{oo}	$\rho_{1,-1}$	Re $\rho_{1,0}$
3.00	2.61	0.33 ± 0.06	-0.23 ± 0.05	-0.06 ± 0.04
3.46	2.77	0.28 ± 0.14	0.15 ± 0.10	-0.08 ± 0.07
4.1	2.95	$0.10^{+0.01}_{-0.02}$	0.18 ± 0.16	
5.5	3.25	0.20 ± 0.05	0.18 ± 0.16	
6.02	3.52	0.08 ± 0.10	0.03 ± 0.13	-0.01 ± 0.08

For the $Y_1^{*+}\pi^-$ channel there is a decrease , at 6 Gev., of the value of ρ_{33} from the Stodolsky-Sakurai value. This may be due to the increase of $K^*(1400)$ exchange or absorption or both.

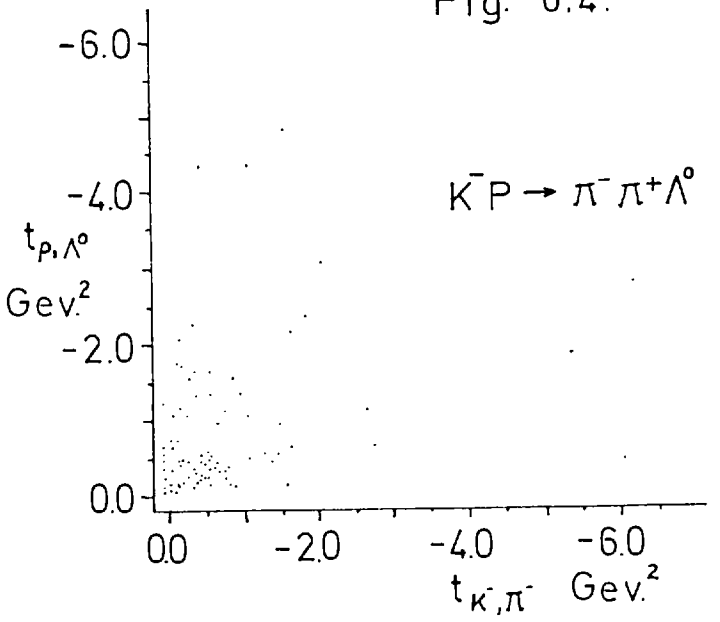
The $\Lambda^\circ\omega^\circ$ channel shows a steady decrease of the value of ρ_{oo} which, if absorption is ignored, can be interpreted as the decrease of the pseudoscalar (K) exchange mechanism and the corresponding increase of the vector exchange mechanism (K^*) to a value of $90 \pm 10\%$ at 6 Gev.

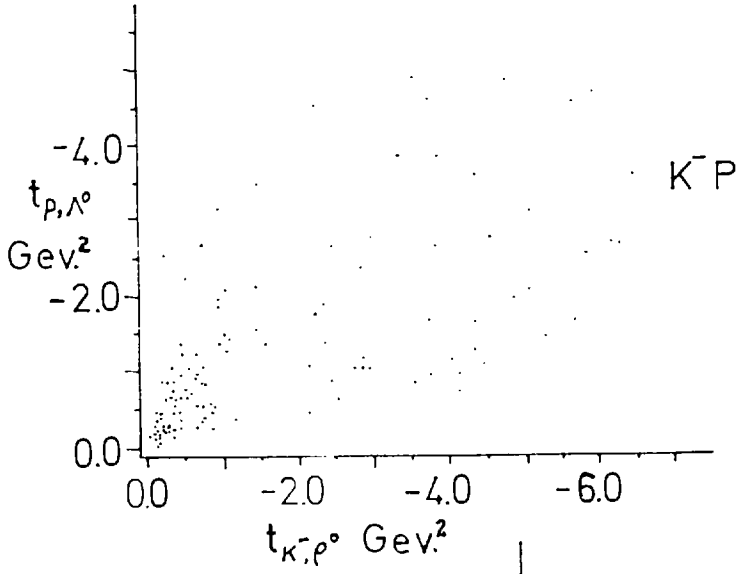
6.2 The three-body channels.

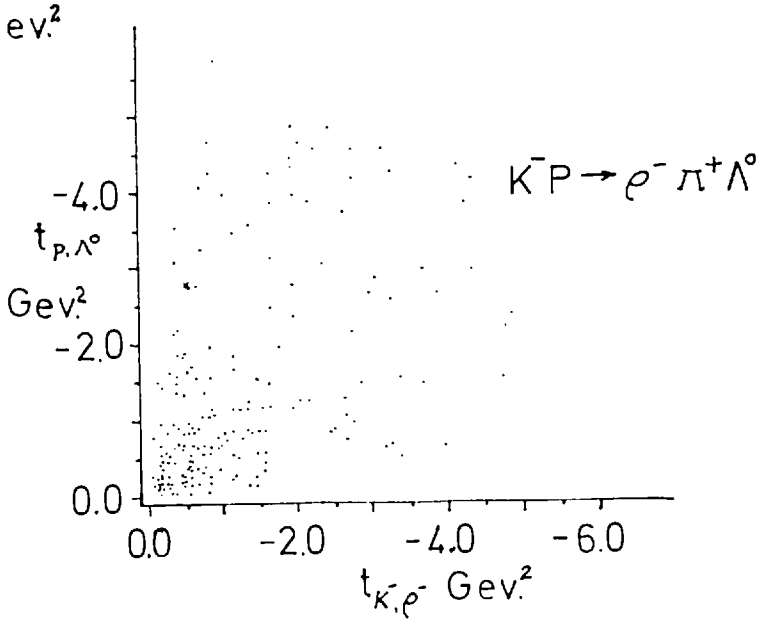
The channels considered in this thesis are $\Lambda^\circ\pi^+\pi^-$, $\Lambda^\circ\pi^\circ\rho^\circ$ and $\Lambda^\circ\pi^+\rho^-$. The essential experimental features of these channels are that the particles of each pair show peripherality in their respective centres of mass, the larger mass particles (except the π^- in the $\Lambda^\circ\pi^+\pi^-$ channel) tend to be simultaneously produced in a peripheral manner and the smallest mass particle (a pion) is produced isotropically in the K^-p centre of mass. See figures 5.10(a), 11(b) and 6.4.

The only model which has been used theoretically to describe the production of three particles is the Double Peripheral Model.[4.10] This has recently been revived in the form of a Double Regge Model where the one particle exchange mechanism is replaced by the exchange of a Regge trajectory.[4.11] See also reference 4.12. The basic idea of explaining the multiparticle production processes by the mechanism of sharing the available centre of mass energy into peripheral two-body subsystems was due to Amati, Stanghellini and Fubini.[6.7] The main predictions of the Double Peripheral Model is in terms of the scattering

Fig. 6.4.


-6.0
-4.0
t_{p,Λ^0}
Gev.^{2}
-2.0
0.0
$K^-P \to \pi^-\pi^+\Lambda^0$
0.0
-2.0
-4.0
-6.0
t_{K^-,π^-} Gev.^{2}


-4.0
t_{p,Λ^0}
Gev.^{2}
-2.0
0.0
$K^-P \to \rho^0\pi^0\Lambda^0$
0.0
-2.0
-4.0
-6.0
t_{K^-,ρ^0} Gev.^{2}


-4.0
t_{p,Λ^0}
Gev.^{2}
-2.0
0.0
$K^-P \to \rho^-\pi^+\Lambda^0$
0.0
-2.0
-4.0
-6.0
t_{K^-,ρ^-} Gev.^{2}

angle of the particles in the centre of mass of the two-body subsystems with respect to the incident particles. It predicts that these should show a peripheral peaking similar to that observed in real two-body processes. In the Double Regge Model the main prediction is that the distribution of the four momentum transfer to the particles at the outer vertices shows a "diffraction like" peaking at small values. All these features are exhibited by the three-body channels considered in this thesis. In addition it appears that in the case when two of the masses are large and the other of relatively small mass the double peripheral mechanism which has the largest cross section is that in which the large mass particles are produced at the outer vertices and the smallest mass particle at the middle vertex. Recent predictions have been made by G.Zweig[6.8] on the distribution of points on the plots shown in Fig. 6.4. One of these is that the density of points is constant along the lines $t_1 + t_2 = 1$. The data are too poor test this but appears to be consistent with it. Other useful references on the Double Peripheral Model are given in references 6.9 and 6.10. The general double peripheral diagram for three-body processes is shown in Fig. 6.3.

A method of identifying which double peripheral graph is appropriate for the production of each event was suggested by Chan et. al[4.11]. This method is to order the particles of each event according to their longitudinal momenta with respect to the

direction of the incident K^-. Then each order can be identified with the appropriate double peripheral graph. This method is only approximate and is very sensitive to two-body contamination. It strictly only applies to events produced by a double peripheral mechanism. The results of this classification are shown in Figs. 6.5 and 6.6. For the $\Lambda^\circ\pi^\circ\rho^\circ$ and $\Lambda^\circ\pi^+\rho^-$ channels the number of configurations is limited due to the peripheral ρ-meson selection criteria, but the inhibited configurations were expected to contribute very little to the cross section. Also the configuration (3) is reduced by the criteria mentioned above and was not used in the following analysis. From Fig. 6.5 it is seen that the main amplitude of the $\Lambda^\circ\pi^+\pi^-$ is that which has $3 = \pi^-$, $4 = \pi^+$ and $5 = \Lambda^\circ$ (configuration 1). This is approximately 50% of all $\Lambda^\circ\pi^+\pi^-$ events. In this configuration e_1 can only be a vector meson due to parity and angular momentum conservation at the kaon vertex and e_2 can be pseudoscalar or vector. Both of course have to be hypercharged. The configurations with $3 = \pi^+$ (2 and 6) are forbidden on the basis of a simple particle exchange due to the necessity of exchanging a doubly charged hypercharged meson, which at present is not known. The large number of events in configuration (2) may be due to some remaining ρ° and possibly f° events. The cross sections of configurations (4) and (5) can be compared on the basis of an isotopic spin analysis. For these configurations $e_1 = \overline{N}^{*-}$ and in (4) $e_2 = n$ or $N^{*\circ}$ and in

Fig. 6.5

$K^- P \rightarrow \Lambda^\circ \pi^+ \pi^-$

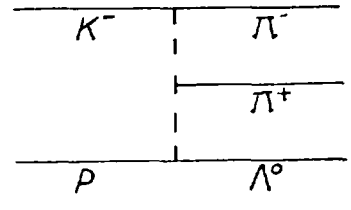
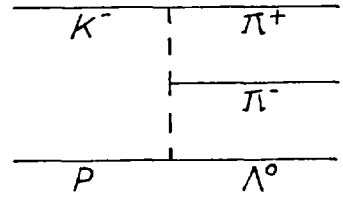
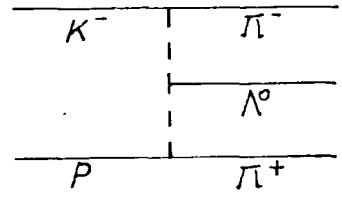
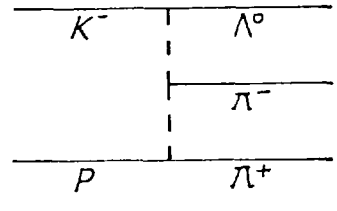
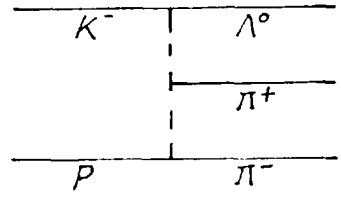
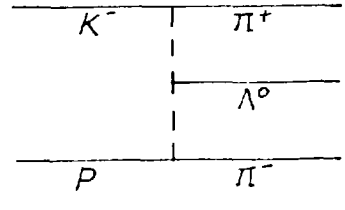
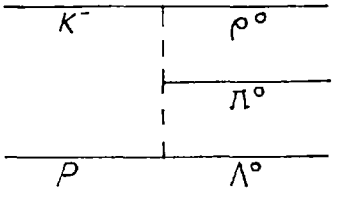
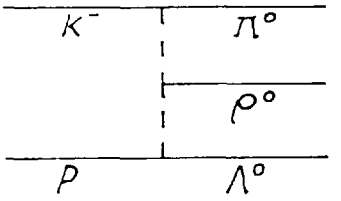
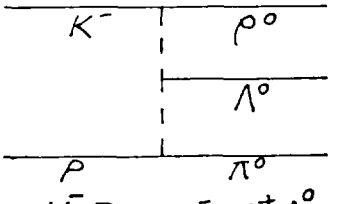
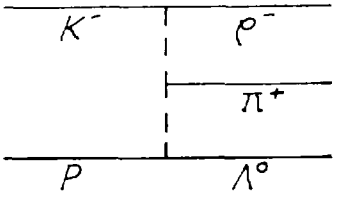
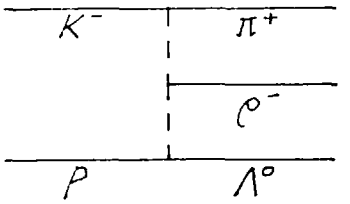
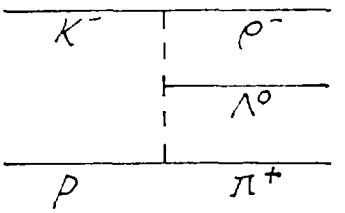
P_l Order	Diagram	No. of events
(1) $P_{l_{\pi^-}} > P_{l_{\pi^+}} \gtrless P_{l_{\Lambda^\circ}}$		47 (43%)
(2) $P_{l_{\pi^+}} > P_{l_{\pi^-}} > P_{l_{\Lambda^\circ}}$		19 (17%)
(3) $P_{l_{\pi^-}} > P_{l_{\Lambda^\circ}} > P_{l_{\pi^+}}$		17 (16%)
(4) $P_{l_{\Lambda^\circ}} > P_{l_{\pi^-}} > P_{l_{\pi^+}}$		12 (11%)
(5) $P_{l_{\Lambda^\circ}} > P_{l_{\pi^+}} > P_{l_{\pi^-}}$		12 (11%)
(6) $P_{l_{\pi^+}} > P_{l_{\Lambda^\circ}} > P_{l_{\pi^-}}$		4 (4%)

Fig. 6.6

$K^- P \rightarrow \rho^0 \pi^0 \Lambda^0$

P_l Order	Diagram	No. of events.
(1) $P_{l\rho^0} > P_{l\pi^0} > P_{l\Lambda^0}$		63 (81%)
(2) $P_{l\pi^0} > P_{l\rho^0} > P_{l\Lambda^0}$		9 (11%)
(3) $P_{l\rho^0} > P_{l\Lambda^0} > P_{l\pi^0}$		6 (8%)

$K^- P \rightarrow \rho^- \pi^+ \Lambda^0$

(1) $P_{l\rho^-} > P_{l\pi^+} > P_{l\Lambda^0}$		90 (75%)
(2) $P_{l\pi^+} > P_{l\rho^-} > P_{l\Lambda^0}$		4 (3%)
(3) $P_{l\rho^-} > P_{l\Lambda^0} > P_{l\pi^+}$		26 (22%)

(5) $e_2 = N^{*++}$ only. For N^* exchange only we have :

$$\sigma_5 / \sigma_4 = 9/4.$$

Experimentally $\sigma_4 = \sigma_5$. Thus if a double peripheral model is assumed then there must be some neutron (n) exchange.

In a similar manner the cross sections of configurations (1) and (3) in the $\Lambda^\circ\pi^\circ\rho^\circ$ and $\Lambda^\circ\pi^+\rho^-$ channels can be compared. For configuration (1) e_1 = pseudoscalar (K) or vector (K^*) and $e_2 = K^*$ if e_1 = K and K or K^* if $e_1 = K^*$. The comparison can still be made with out knowing the amounts of K and K^* exchange because they are both isospinors. Thus for configuration (1) we have : $\sigma_{\Lambda^\circ\pi^\circ\rho^\circ} / \sigma_{\Lambda^\circ\pi^+\rho^-} = 1 / 4$

For configuration (3) e_1 = K or K^* and e_2 = nucleon only.

Hence : $\sigma_{\Lambda^\circ\pi^\circ\rho^\circ} / \sigma_{\Lambda^\circ\pi^+\rho^-} = 1 / 4$

For (1) the experimental value is about 1/1.5. This number however is seriously affected by the selection criteria and is unreliable. For (3) the experimental value is about 1/4. This configuration can be expected to be more reliable because the Λ° and π^+ are unlikely to have an effective mass in the Y_1^{*+} mass range. The fact that there are more events in configuration (3) in the $\Lambda^\circ\pi^+\rho^-$ channel than the $\Lambda^\circ\pi^\circ\rho^\circ$ channel causes the differences discussed in section 5.3 for the $\Lambda^\circ\pi^+\rho^-$ channel.

6.3 The four-body channel.

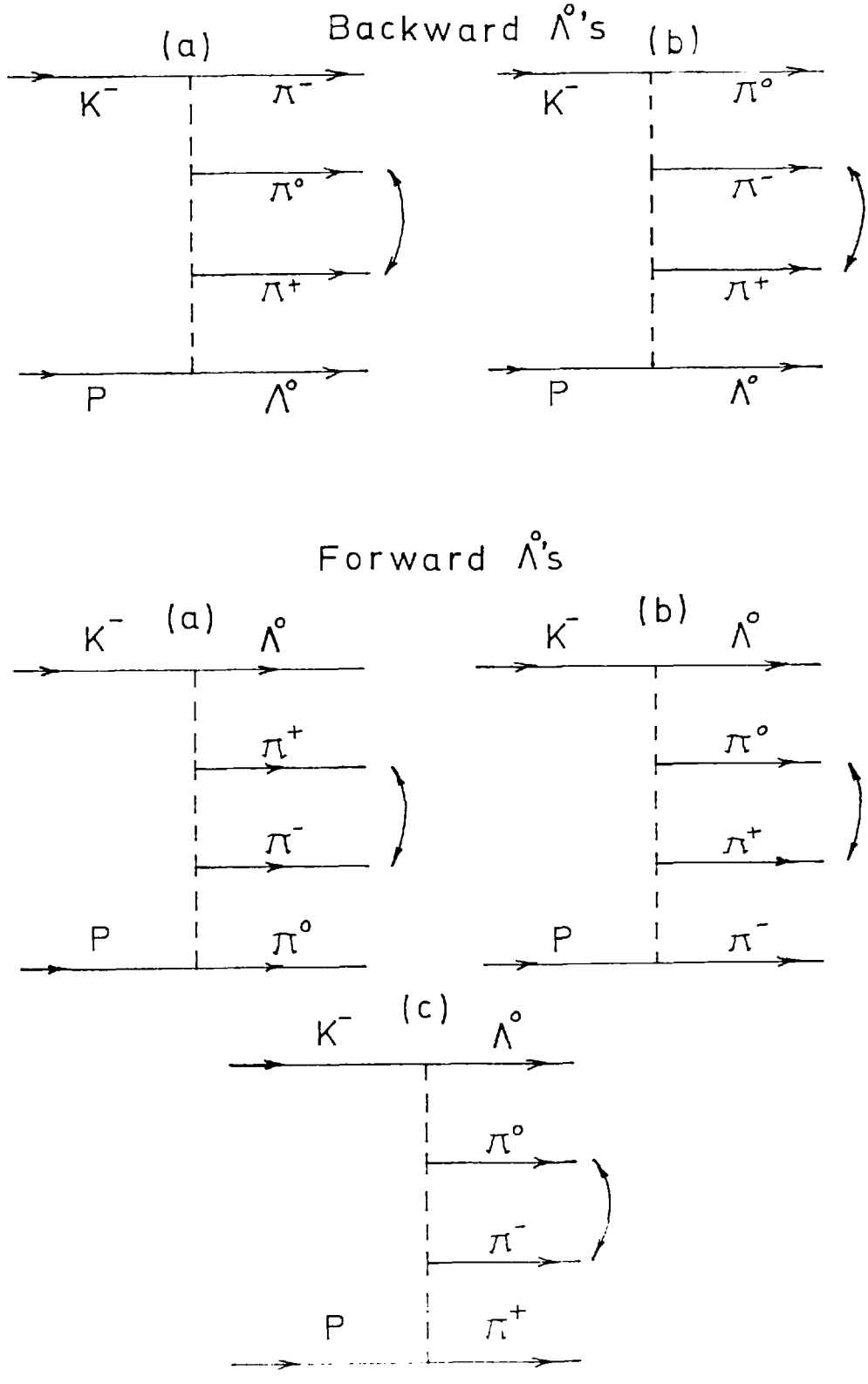
The channel considered is $\Lambda^\circ\pi^+\pi^-\pi^\circ$. With the addition of another particle the complexity of the problem of determining

the production mechanism increases enormously and at this energy the situation is made less well defined in terms of the overall peripherality. However from the angular analysis given in Chapter 5 we can consider two main triple peripheral diagrams for the backward Λ°'s. These are shown in Fig. 6.7. For these diagrams we have K or K^{*} exchanged between the particles and an isotopic spin analysis gives : $\sigma_a / \sigma_b = 2$. Experimentally this ratio is 2 to 1.5.

For the forward Λ°'s there are three possible diagrams. These are shown in Fig. 6.7. The ratio of $\sigma_a : \sigma_b : \sigma_c$ is 10: 9:0.8 assuming N^{*} exchange only. The experimental values are 10: 6: 5. The presence of nucleon exchange will obviously change the predicted values and also the fact that no phase has been considered betwoen the two diagrams obtained by permuting the centre particles.

Fig. 6.7.

Four-Body Process $K^- P \rightarrow \Lambda^\circ \pi^+ \pi^- \pi^\circ$



CONCLUSION

The zero hypercharge baryons which were studied in this thesis are produced very peripherally ($-t_{p,\Lambda^\circ}$ or Y_1^{*+} < 1.0) in the two-body processes. They are also produced with a small background which makes the isolation of these channels relatively easy. The production mechanism is dominated by the exchange of a hypercharged vector meson system (K^*). In the $Y_1^{*+}\pi^-$ channel there appears to be a departure from the strong M1 coupling at the $p\,K^{*o}\,Y_1^{*+}$ vertex seen at other energies. There is a definite peripheral peak in the forward direction of the Λ° production angular distribution in the $\Lambda^\circ\omega^\circ$ channel which implies a baryon exchange production mechanism. A significant polarization of the Λ°'s was found which is opposite in sign for the forward and backward Λ°'s. The cross section of the $Y_1^{*+}\pi^-$, and $Y_1^{*+}\rho^-$ channels decreases approximately as $(\text{c.m. energy})^{-5}$ and that of the $\Lambda^\circ\omega^\circ$ channel as $(\text{c.m. energy})^{-10}$. This difference is due to the faster decrease of the baryon exchange part of the $\Lambda^\circ\omega^\circ$ cross section(6.1). In general, in K^-p interactions at this energy, the cross section of the channels zero hypercharge meson + zero hypercharge baryon are almost an order of magnitude smaller than the channels negative hypercharge meson + positive hypercharge baryon(7.1). This indicates, since the initial state is negative hypercharge meson + positive hypercharge baryon, the strong damping of the

hypercharge exchange mechanism. The two-body processes can provide very useful information about the K^-p interaction at high energy provided the statistical level of the experiment is high enough to compensate the rapid decrease in the two-body cross section.

The main contribution of this thesis to the study of the production mechanisms of zero hypercharge baryons lies in the analysis of the three-body channels. It has shown that the kinematic features of these channels are consistent with a Double Peripheral or Double Regge Model of the production mechanism.

There is evidence for a baryon exchange mechanism in the $\Lambda^\circ\pi^+\pi^-$ channel from the presence of a well defined forward peak in the production angular distribution of the Λ°. There is also evidence for a similar mechanism in the $\Lambda^\circ\pi^+\rho^-$ channel. From a brief study of the $\Lambda^\circ\rho\pi$ channel at 3.5 Gev. and 10 Gev. it appears that its maximum cross section is at about 6.0 Gev. This, plus the fact that this channel is difficult to isolate, makes the study of this channel at various energies very difficult. The best three-body channels to study are those in which the particles are stable against strong decays or are narrow well defined resonances and in which the two-body channels are weakly produced or the associated resonances are at the edge of phase space(i.e. $N^*(1238)$ and $Y_1^{*+}(1385)$. Examples of such channels are:

(i) $K^- p \longrightarrow \Lambda^\circ \pi^\circ \varphi^\circ$

(ii) $K^- p \longrightarrow K^{*-} \pi^+ n$

(iii) $K^+ p \longrightarrow K^+ \pi^+ n$

(iv) $K^- p \longrightarrow N^{*++} K^- \pi^-$

(v) $pp \longrightarrow pp \pi^\circ$

There is evidence of the features of a Double Peripheral production mechanism in the channels $K^{*-} \pi^+ n$, $K^{*-} \pi^\circ p$, $K^{*\circ} \pi^\circ p$ and $N^{*++} K^- \pi^-$ in this experiment (7.1) and in the process

$$p \bar{p} \longrightarrow \overline{N^{*++}} N^{*++} \pi^\circ \quad (7.2)$$

There is a large increase in the ratio of three-body to two-body cross sections with increasing energy which emphasises the need to study the three-body channels.

The study of the four-body channel has exemplified the inherent analytic complexity of these channels and is sufficiently interesting to justify a study at higher energies where the increased peripherality will assist in the determination of the production mechanism.

REFERENCES

0.1	M. Gell-Mann	Proc. of the Int. Conf. on H.E.N.P. CERN 805 - 1962.
0.2	M. Gell-Mann	P.R. 125,1067, 1962.
0.3	Y. Neeman	Nuc. Phys. 26, 222, 1961.
0.4	Colley et. al.	P.L. 19, 2, 152, 1965.
1.1	Keil and Neal	Proc. of Int. Conf. Dubna 1963.
1.2	W.W. Neal	Prog. in Nuc. Tech. and Instr. 2-1965.
1.3	W.W. Neal	Prog. in Nuc. Tech. and Instr. 2 . To be published.
1.4	W.W. Neal	Private communication.
1.5	Riddiford et. al.	Int. Conf. on H.E. Accel. and Instr. CERN 1959.
1.6	Welford	Applied Optics 2, 10, 1963.
1.7	Mag. Field of B.N.H.B.C.	CERN / TC / NBC 2-1963.
1.8	Welford	Applied Optics 2, 10, 1963.
1.9	F. Fuchs	M.Sc. Thesis Imperial College 1966.
2.1	Burren and Sparrow	NIRL / R / 14, 1963.
2.2	A. G. Wilson	NIRL/ M / 38, 1963.
2.3	M. Scarr	B.N.L. Upton N.Y. U.S.A.
2.4	J. Allison	Ph. D Thesis Oxford 1966.
2.5	F.T. Solmitz	Ecole Polytechnique 1960.
3.1	Rosenfeld et. al.	U.C.R.L. 8030, Pt 1 , Jan. 1967.
3.2	Galbraith et. al.	P.R. 138, B 913, 1965.

4.1	G.F. Chew	Benjamin Inc. Publishers.
4.2	N.N. Schmitz	Proc. CERN Easter School Vol.1 1965.
4.3	J.D. Jackson	N.C. Serie X, 34, 1644, 1964.
4.4	R. Davis et. al.	A.N.L. Illinois.
4.5	Rosenfeld et. al.	U.C.R.L. 8030, Pt.1, Jan. 1967.
4.6	Gottfried and Jackson	CERN Preprint 8010 / TH / 397 1964.
4.7	Stodolsky and Sakauri	P.R.L. 11, 2, 90, 1963.
4.8	Gottfried and Jackson	CERN Preprint 8956 / TH / 428 1964
4.9	R. Davis et. al.	A.N.L. Illinois.
	S. Baker	Ph.D. Thesis Imperial College 1966.
4.10	Joseph and Pilkuhn	N.C. Serie X, 33, 1407, 1964.
4.11	Chan Hong Mo et. al.	CERN Preprint 66/ 845 / 5 TH 679 1966.
4.12	Frazer and Roberts	ICTP / 66 / 2 1966.
5.1	Lindsey et.al.	P.R.L. 15, 5, 1965.
5.2	Lindsey et. al.	P.L. 20, 1, 1966.
5.3	G. Goldhaber	Private communication
5.4	G. Goldhaber	Review at Berkeley 1967.
5.5	London et. al.	B.N.L. Report BNL 9542(C-58) 1966.
6.1	D.R. Morrison	P.L. 22, 4, 528, 1966.
6.2	Refs. 4.4, 5.5, Ross et. al. Dubna Report 1964, J. Badier et. al. Dubna Report 1964, B.G.L(I.C.).O.RL. Collaboration Oxford Univ. Preprint 1966.	
6.3	Jackson et. al.	P.R. 139, 2B, 428, 1965.
6.4	Selleri	N.C. 42, A,4, 835, 1966.

6.5 T. Regge N.C. 14, 951, 1959, and 18, 947, 1960.

6.6 Chew and Frautschi P.R.L. 7, 394, 1961 and 8,41, 1962.

6.7 Amati et. al. N.C. 26, 896, 1962.

6.8 Private communication from G. Jones Cal. Tech. Pasadena 1967.

6.9 T.W.B. Kibble P.R. 131,5, 2282, 1963.

6.10 M.S.K. Razmi N.C. Serie X, 31, 3, 615,1965.

7.1 P.K. Chaudhuri Ph.D. Thesis Imperial College 1967.

7.2 Alles-Borelli et. al. CERN / TC / Physics 66-6 1966.

ACKNOWLEDGEMENTS

I should like to express my gratitude to Professor C.C. Butler for enabling me to work in his High Energy Physics Group at Imperial College.

Aknowledgement is made of the assistance and useful guidance given by Drs. S.J.Goldsack and S.L.Baker and the many stimulating and encouraging discussions with my colleagues L.K.Sisterson, Dr.P.K.Chaudhuri, Dr.A.W.Eskreys and Dr.M.Saeed.

The work of Mrs.S.Hulbert and Miss A. Tomlin and the many scanners, measurers and technical staff in the initial stages of this experiment is gratefully aknowledged.

The Imperial College Computer Unit staff are warmly thanked for their assistance and cooperation.

I am grateful to the Science Research Council for their maintainence grant.

Finally I am greatly indebted to my wife for assistance in the typing and presentation of this work and constant encouragement.